Air cooling of an EMSM field winding

SAMUEL ESTENLUND

DIV. OF INDUSTRIAL ELECTRICAL ENGINEERING AND AUTOMATION | LUND UNIVERSITY

Air cooling of an EMSM field winding

Air cooling of an EMSM field winding

by Samuel Estenlund

Licentiate Thesis
Division of Industrial Electrical Engineering and Automation,
Department of Biomedical Engineering, Lund University

2018

If anyone supposes that he knows anything,
he has not yet known as he ought to know;
but if anyone loves God, he is known by Him.

1 Corinthians 8:2-3

Acknowledgements

Almost four year ago, a few months after I received my Master of Science diploma, I was on my way back to school to listen to a friend's Master's Thesis presentation. At the time I was still looking for a job after my degree, and a few interviews and more applications that had led me nowhere, I started to plan how I would look for old professors I had studied under and lead the conversations to job offers at the University, or anywhere. But I soon realized that my strategies would just come out cheezy and then stopped and said:

"God, I'm not the one writing this story, but you are. If it is your plan than anything good for my career will come out of this visit, I leave it completely up to you. I won't let any bad strategies of mine come in the way of yours."

So I went to the university, listened to my friend's presentation, had a few short conversations with old class mates, and as people started leaving, I started to walk home too. But halfway out of the building I remembered that I had forgotten my jacket back in the room of the presentation. So I went back and had barely entered the room when an old professor of mine asked me what I had been doing since my degree.

"Mostly enjoying my free time, and writing job applications" I answered.

"I have some teaching and research possibilities that I want to discuss with you". Boom. Just like that. You can call it whatever you want, I'll respect that, but for me there is a purpose to why I have gotten this chance to write a PhD thesis and that has been a great comfort for me as I'm traveling this road.

It's a tough road to travel at times, when you're struggling with all the challenges that makes you feel dumber and dumber until you realize how much you've grown during the struggle - the process we call learning - and through all that, there are a lot of people who have played different roles on the journey this far.

First, I want to mention my family, my wife and our two or three or so kids.

We've grown in this together and are continuing to do so, figuratively and literally. Our third child is expected to be born in a week, at the time of writing this, but before this is printed, this might be past tense. Thank you for all the ways you have helped me, to work extra when I have needed to, and to not work when I have needed to.

I also want to thank Mats Alaküla, my supervisor, for offering me this opportunity and for all the discussions about research, progress, absence of progress, life, the universe and everything. I always walk out of our meetings filled with inspiration and eager to proceed.

My co-supervisor Avo Reinap is also deserving of my gratitude, for always being available and willing to listen to my unclear thoughts unorderly expressed in words. I have always walked out of our meetings filled with other questions, often better, than the ones I had when I came to them.

In software engineering there is a debugging method called rubber duck debugging. Whenever you're not completely sure why your code behaves the way it does, or what you even want it to do, it's good to have a rubber duck on your desk. You appoint the duck and explain to it, in detail, what your code is doing, line by line, and eventually that monologue might make you realize what was unclear to you. Conventionally, rubber ducks don't talk back, but mine have. I call them Philip and Michael, and innumerous monologues and dialogues have taken me through issues during the work.

I want to thank my co-office friends and colleagues, for telling me when the music in my head slips out too much, and for pointing out where I'm wrong whenever I get excited about things I thought I had understood. You're awesome! Sebbe de H, han e en go go kille. Anton, we'll catch up on Spain and Monaco when we're both back from our ten days. Gabo, I'd double check your seat before you sit down next time you come to your office if I were you.

There are so many more colleagues and co-workers that have meant a lot to me. Carina, Conny, Fran, GD, Gunnar, Henriette, Johan, Jörgen, Max, Olof, Ulf, Ulrika, and more, you all deserve much more ink or pixels than what your names make up here.

There are also people from other divisions at the University who deserve mentioning for sharing their expertise where I have lacked it. Marcus Lundgren, Zan Wu, Bengt Sundén and Christoffer Norberg, thank you for sharing your time and experience!

Finally, my parents, siblings, family-in-law, Dr Per with family, Dr Samme B,

hemgruppen, and more, you have inspired, supported and prayed for me in different ways, and I'm so glad for that.

Abstract

The performance of electrical machines are tangibly limited by thermal limitations. The difference in torque and power between what the machine can maintain continuously and for shorter bursts is often significant and regularly requires a machine to be over-sized to meet specification requirements. For some applications this is not a substantial problem, but for others the power and torque density of the machine is the most important parameter. Traction machines for electrical vehicles (EVs) is an example of an application where the latter may be true.

There are several electrical machine topologies that are suitable for EV traction. Permanent magnet synchronous machines (PMSMs) have dominated the EV market for a few years with no sign of backing down, but induction machines and electrically magnetized synchronous machines (EMSMs) are also represented in a few models. The EMSM is an example of a machine topology where the thermal restrictions are apparent and if the heat generation in an EMSM can be handled effectively, it has serious potential for high power density operation.

This thesis presents two similar concepts for parallel direct air cooling, using rectangular windings with either indented sides or hollow windings, and attempts to answer the question whether direct cooling can make EMSMs to match or outperform PMSMs for EV traction. The direct cooling concepts are studied analytically in an empirical-lumped parameter model, which is tested experimentally for validation. The outcome of the model suggests that current densities of at least 16 A/mm^2 are achievable continuously (through an area where copper, cooling ducts and insulation are included).

An electrically magnetized rotor is designed, utilizing the proposed direct cooling concepts, fitting in a stator originally designed for an interior PMSM rotor. Through simulations the performance of the EMSM and the PMSM are compared, resulting in comparable performances but with slightly lower efficiency for the EMSM due to the extra cooling.

It is concluded that the direct cooling concepts proposed are promising and worth further studies. A few examples of future work needed are more experiments for more dimensions and operations points are needed in the future, as well as the design of a whole system including a pump for the coolant air, and rotor current supply (with slip rings or a rotating transformer).

Nomenclature

Glossary

space harmonics	Harmonics in a current caused by the movement of machine arts, i.e. current harmonics induced by to flux variations when stator teeth pass a rotor tooth. 56
time harmonics	Harmonics in a current, independent of the machines movement, i.e. current ripple form converter. 82
wedge	Part or a tooth covering part of the slot opening near the air-gap. 56

Acronyms

BEV	battery electric vehicle 1
CFD	computational fluid dynamics 85, 88
DSSRM	double stator switched reluctance machine 13
EE	electrically excited, or electrically magnetized (not to be confused with EM: electrical machine) 1
EMSM	electrically magnetized synchronous machine 6, 14–17, 65, 72, 73, 78–80, 82, 83, 85, 86, 90, 91
EV	electric vehicle 1, 12, 13, 15, 16
HEV	hybrid electric vehicle 12, 15, 16
IM	induction machine 1, 13–16
IPMSM	interior permanent magnet synchronous machine 5, 6, 10, 13–15, 53, 65, 70, 79, 82, 83, 85, 86, 90
PHEV	plug-in hybrid electric vehicle 1
PM	permanent magnet 1, 9, 20, 83, 85
PMSM	permanent magnet synchronous machine 10, 14–16, 20, 21
SRM	switched reluctance machine machine 12–14, 20, 21
synRM	synchronous reluctance machine 10, 12

List of Symbols

A	Area [m^2] 30, 32
A_{dw}	Surface area of a section of a pipe [m^2] 35, 36
C	Geometry constant for the Reynolds number [-] 33
c_{p}	Specific heat [J/kgK] 32
C_{wp}	Inner circumference of wetted perimeter of a not necessarily circular pipe [m] 31, 32
D	Inner diameter of pipe [m] 30, 35, 40, 41
D_{h}	Inner hydraulic diameter of a not necessarily circular pipe [m] 31–33, 35
e	Induced voltage [V] 68, 69
f	The Darcy friction factor [-] 32–35, 40, 41, 43
h	Heat transfer coefficient [W/Km^2] 30, 35, 39, 40
h_{s}	Slot height [m] 57, 65–67, 78
I	Current [A] 44
I_{r}	Rotor slot current [A] 57, 60, 61, 63, 65, 68, 69, 71, 78, 80, 82, 93
i_{r}	Rotor current per turn [A] 71
I_{x}	x-component of stator winding current per phase and turn [A$_{\mathrm{rms}}$] 57, 63, 65, 68, 69, 71, 73, 76, 78–81, 93
i_{x}	Power invariant stator x-current [A] 9, 10, 71, 79
I_{y}	y-component of stator winding current per phase and turn [A$_{\mathrm{rms}}$] 57, 63, 65, 68, 69, 76, 78, 79, 93
i_{y}	Power invariant stator y-current [A] 9, 71, 79
J	Current density A/m^2 44, 45
k	Heat transfer replacement constant [W/K] 30
k_{b}	Bend coefficient [-] 40
k_{f}	Copper fill factor [-] 44
L	Length [m] 30, 35, 36, 39–41, 44–46, 70
L_{mx}	Mutual inductance in x-axis [H] 9, 65
L_{my}	Mutual inductance in y-axis [H] 9, 65
$\dot{m}$	Mass flow through cross section of pipe [kg/s] 35
Ma	Mach speed [m/s] 37
n	Arbritrary integer [-] 12
Nu	The Nusselt number [-] 30, 33–35
P	Pressure [Pa] 36
p_{L}	Losses [W] 68, 69
p_{m}	Mechanical power [W] 74
Pr	The Prandtl number [-] 32–34
p_{res}	Resistive copper losses [W] 37
dP	Pressure drop [Pa] 35, 40, 41
Q	Heat flow [W] 30, 31, 35
r	Radius [m] 39, 44
Re	The Reynolds number [-] 32–35
s	Side length of rectangular winding [m] 39, 44
T	Torque [Nm] 9, 68, 69
T_{amb}	Temperature of heat radiating body's surrounding [K] 30
T_{b}	Bulk temperature, average of the fluid temperatures through a cross section of a pipe [K] 30, 31, 35

T_{body} Temperature of heat radiating body [K] 30

T_{c} Wall temperature of copper [K] 35, 37

T_{f} Temperature distribution in the fluid in a pipe [K] 30, 31

T_{s} Temperature distribution in the solid surrounding a pipe [K] 31

T_{w} Temperature of the wall of the solid surrounding a pipe [K] 31, 35

ΔT Temperature difference [K] 30, 31

u_{m} Mean velocity of fluid through cross section of pipe [m/s] 32, 35, 40, 41

u_{sy} Stator y-voltage [V] 10

w_{s} Slot width [m] 57, 65–67, 78

x Distance along length L for parameters distributed along a pipe [m] 33

ϵ_{r} Absolute roughness [m] 35

ε Emissivity coefficient 30

λ Heat conductivity [W/Km] 30, 32

μ Dynamic viscosity [Ns/m^2] 32

ν Kinematic viscosity [m^2/s] 32, 36

ϕ Number of phases [-] 12

Ψ_{r} Rotor (winding) flux linkage [Vs] 9, 10, 14

ρ Density [kg/m^3] 40, 41

σ Stefan Boltzmann's constant [W/m^{2}K^4] 30

Contents

Chapter 1

Introduction

1.1 Background

1.1.1 Electrical machine topologies in the EV market

On a website tracking plug-in car sales all over the world [1], the 20 most sold battery electric vehicle (BEV) and plug-in hybrid electric vehicle (PHEV) models in the world during 2017 has been put together. The sales numbers are presented in table 1.1 together with the topology of the electrical machine for each model.

From the data, it is clear that permanent magnets (PMs) are used in almost all of the most popular models. Even among the manufacturers using other topologies, a move towards permanent magnet machines is seen. Tesla Model 3 have PM machines, in contrast to Tesla's previous models. Renault have been using electrically excited, or electrically magnetized (not to be confused with EM: electrical machine) (EE) machines for years, but some versions of the Renault Zoe from 2016 and on use PM machines.

From 2007 to 2012 a majority of all electric vehicles (EVs) used induction machines (IMs) [18]. Before that DC machines where the most common topology. But today, PM machines are simply dominating the EV market.

Table 1.1: Top 20 EV sales in the world in 2017 and machine topologies

	Manuf.	Model	Sales	Share	Topology
1	BAIC	EC-Series	78 079	6.4 %	PM [2]
2	Tesla	Model S	54 715	4.5 %	IM [3]
3	Toyota	Prius Prime / PHV	50 830	4.2 %	PM [3]
4	Nissan	Leaf I+II	47 195	3.9 %	PM [4]
5	Tesla	Model X	46 535	3.8 %	IM [3]
6	Zhi Dou	D2	42 342	3.5 %	PM [5]
7	Renault	Zoe	31 932	2.6 %	EE^a [6]
8	BMW	i3	31 410	2.6 %	PM [3]
9	BYD	Song PHEV	30 920	2.5 %	PM [7]
10	Chevrolet	Bolt^b	27 982	2.3 %	PM [8]
11	Chery	eQ	27 444	2.2 %	PM [9]
12	Chevrolet	Volt	26 291	2.1 %	PM [10]
13	JAC	iEV7S/E	25 745	2.1 %	PM [11]
14	Mitsubishi	Outlander PHEV	25 571	2.1 %	PM [12]
15	BYD	e5	23 632	1.9 %	PM [13]
16	Geely	Emgrand EV	23 324	1.9 %	PM [14]
17	BYD	Qin PHEV	20 791	1.7 %	PM [15]
18	BMW	330e	19 815	1.6 %	PM [16]
19	Roewe	eRX5 PHEV	19 510	1.6 %	PM [7]
20	Hyundai	Ioniq Electric	17 241	1.4 %	PM [17]
21+	Rest		552 799	45.2 %	-
-	Total		1 224 103	100 %	-

---

^{a}Sports model uses PM
^{b}Includes Opel Ampera-e

1.1.2   Permanent magnets

Neodymium and Dysprosium are rare earth metals and key elements in the type of permanent magnets used in today's PM electric machines. Rare earth metals are, despite the name, not particularly rare in the earth's crust. They appear in several minerals around the world, although not in pure form but mixed with several or all of the 17 metals classified as rare earth metals. The hardest part about rare earth metals is thus not finding them, but separating them from each other. That process is costly and produces lots of salt water and waste that can be both toxic [19] and radioactive [20].

In the mid 1980's 75 % of the rare earth metals produced in the world was produced outside China [21]. Since then all but a few mines outside China was eventually depleted or closed partly due to increased regulations for the waste in the western world leading to profitability problems [22]. Meanwhile, rare earth mines and production sites in China increased and in 2010 97 % of all rare earth metals were produced in China, a majority of which comes from the area around the city of Baotou, Inner Mongolia. Reports of enormous lakes of waste sludge [19] and contaminated ground water making farming impossible in a large area around Baotou [23], have been frequent in the last decade [24].

Markets like EVs and wind turbines, that use permanent magnets, are thus heavily dependent on a single limited part of the world. The problems with a dependency like that became evident when China limited rare earth metal exports in 2009 and 2010 [20], leading to a world wide shortage and a tenfold price increase of rare earth metals in 2011 [25]. Luckily, the price spike only lasted for a few months. The World Trade Organisation deemed China's export limits illegal, making such a price spike improbable in the future, and the price went back to normal levels after the spike [26].

The rare earth metal crisis in 2011 lead to an increase in rare earth metal production outside China, and today the rest of the world produces about 15 % of the worlds rare earth metals, compared to 3 % in 2010 [21].

However, there are more aspects with rare earth metal production to keep a watching eye on. In 2010, about half of Chinas rare earth metals came from illegal production, and China has since then put in efforts to close down the illegal sites. The price of rare earth metals have started to increase during 2017, much because of the closed down illegal sites in China [27]. More shortages are predicted in the future [28], and with the decreasing production in China, and its demands still growing, China could be a net importer of rare earth metals within a few years [26], which could hit the EV market if the technology does

not change the growing dependency on rare earth permanent magnets [29].

1.1.3   Application challenges

Most people today have experience from driving combustion engined cars, and know that the temperature of the engine very rarely is something that limits the cars performance or usage. The nature of a combustion engine allows a well dimensioned cooling systems with jackets close to both the source of the heat and to the parts sensitive to high temperatures. The coolant is cooling the cylinder, cylinder head and the oil which in turn keeps the pistons cool enough to not cease the cylinder. Compared to an electrical machine, a combustion engine has a lower efficiency and generates more excess heat, but most of it in gases which are taken out through the exhaust system and replaced by new cooler air between the combustions. A combustion engine can often run on maximum power for hours, days or even weeks before breaking down.

An electrical machine can normally not do that. The maximum power limited by the power supply can in most machines be used continuously only for seconds rather than minutes. In most electrical machines, the cooling is situated at the exterior of the machine, while the heat sources and the parts sensitive to high temperatures are both deep inside its interior. For the machine to not overheat in the long run, the heat has to travel to the exterior of the machine and be taken away from there at the same rate it is generated. For most machines this means that the continuous power is significantly lower than the maximum power output.

To be able to maintain a higher continuous power, efficiency can be improved to minimize the heat generation, but only to some degree. Another way to reach higher continuous power is improving the cooling, but with exterior cooling, that has a limited effect too. Often this results in the machine being over-sized, with a higher maximum power than required, to get the thermally balanced continuous power high enough.

In many cases, this is not a problem, like when the monetary cost for building a machine with higher efficiency and more effective cooling is a bigger drawback than the extra volume and weight a larger machine occupies. But some cases require a higher power density, and thus a solution that enables a higher continuous power without over-sizing the machine.

An extreme example of an EV application like this is a truck driving in the Alps. The weight of the vehicle is heavy. The slope can be steep up hills, lasting not

just for a minute or two, but considerably longer. The roads go through small villages with narrow turns and crossings, calling for an agile vehicles with few shafts. This means a powerful traction system has to be put one one single shaft, and it raises the question: Is there a way to, just like the combustion engine, put efficient and effective cooling closer both to the source of the heat and the parts sensitive to high temperatures, and with that enable higher continuous power?

1.2   Objectives

The objectives of this thesis is to analytically study a concept of direct cooled windings in an electrical machine. The concept consists of rectangular windings that are either hollow or have indents along the sides, allowing a coolant to be pushed through the axial length of the machine. This is studied theoretically in empirical models and compared to experimental results for verification.

To test the performance, an electrically excited rotor with direct cooled windings is designed. The rotor fits in the stator of an existing interior permanent magnet synchronous machine (IPMSM), and the performances of the machine with the two different rotors are compared using electromagnetic 2D simulations.

1.3   Contributions

The main contributions of this thesis are as follows.

- A wide comparison of alternative electric traction machines without permanent magnetization.

- A detailed modeling and optimization of an electrically excited traction machine with direct air-cooled rotor windings.

1.4   Outlines

This thesis is divided into six chapters. The first three chapters make out an inquiring part that gives the prerequisites and delimitations for the work in chapters 4 and 5 before the work is summed up and concluded in chapter 6.

The first chapter gives an initial nature of the problem - A PM-less machine capable of high load during long time periods. The motivation for researching PM-less topologies for EV traction is given as well as an example of an application where high load during long time periods is required.

The second chapter contains a literature study for PM-less topologies with potential for EV traction. The electrically magnetized synchronous machine (EMSM) is found to have interesting potential, if the thermal problems can be manages.

The third chapter presents the principle of direct cooling, a few examples of applications in literature along with the direct cooled concept that will be investigated in the rest of the thesis, in an attempt to solve the thermal problems of the EMSM.

The fourth chapter describes a heat transfer model that will study the potential of the direct cooling concept. The theory of the model and its possibilities and inadequacies are explained, before the presentation of an experimental validation and the results of the model lead to some tools and experiences that are integrated in the fifth chapter.

The fifth chapter designs an EMSM rotor for an existing IPMSM. The IPMSM is used for reference of the performance of the EMSM-rotor that will utilize the concept oresentet in chapter three and explored in chapter four. The performance comparison to the reference machine is used to draw some conclusions on the work, and not least present some ideas on how the concept could be developed in the future.

1.5   Publications

In parallel with the work of this thesis, the following has been published:

- Avo Reinap, Mats Alaküla, Sebastian Hall and Samuel Estenlund, "Performance estimation of hybrid excited machine with alternating pole configuration," *2014 International Conference on Electrical Machines (ICEM)*, Berlin (Germany), 2014.

- Samuel Estenlund, Mats Alaküla and Avo Reinap, "PM-less machine topologies for EV traction: A literature review," *2016 International Conference on Electrical Systems for Aircraft, Railway, Ship Propulsion and*

Road Vehicles & International Transportation Electrification Conference (ESARS-ITEC), Toulouse (France), 2016.

- Samuel Estenlund, "Model of air cooled windings for traction machine", *XXIIIrd International Conference on Electrical Machines (ICEM)*, Alexandroupoli (Greece), 2018.

Chapter 2

Literature study of different topologies

This chapter is broadly an extract from a literature study conducted by the author and published as a conference paper [30]. It covers some of the most common and conventional machine topologies, presenting their advantages, disadvantages, areas in need of development and their potential for the electrical vehicle market.

2.1 Background of the literature study

There are many ways to build an electric machine without permanent magnets. The generated torque with optional saliency can be described with equation 2.1 applying to many conventional electrical machine topologies.

$$T = \underbrace{\Psi_\mathrm{r} i_\mathrm{y}}_{\text{Excitation}} + \underbrace{(L_\mathrm{mx} - L_\mathrm{my}) i_\mathrm{x} i_\mathrm{y}}_{\text{Reluctance}} \tag{2.1}$$

Equation 2.1 shows that there are two components contributing to the torque. The first depends on the rotor excitation that gives the flux Ψ_r, which is partly what makes PM machines so advantageous. The second comes from the reluctance, which depends of the saliency of the rotor.

For the first component of the torque generation, the stator current in the quadrature axis is vital (in this thesis called i_y, see appendix A). The quadrature

axis stator voltage, u_{sy}, of a permanent magnet synchronous machine (PMSM), that is used to control this current, is described as follows.

$$u_{sy} = R_s i_y + L_{sy}\frac{di_y}{dt} + \omega_r(\Psi_r + L_{sx}i_x) \tag{2.2}$$

In Equation 2.2, the main reason for an electric machine's speed range is indicated. As the speed increases, the rotor flux, Ψ_r induces a voltage counter to the voltage output from the converter. Eventually this voltage, known as the back emf, becomes higher than the converter voltage, and the control of the stator current is not possible. Conventional field weakening is employed by feeding the stator with a negative direct axis current, i_x. Equations 2.1 and 2.2 applies to a number of conventional machine topologies, but the principle of the voltage supply limitation and the need of reducing the magnetic flux linking stator and rotor at higher speeds apply for all machines.

With this in mind, the most relevant PM-less topologies are explained briefly. An example of each topology, including the IPMSM, is shown in Figure 2.1.

2.2   Synchronous reluctance machine

The synchronous reluctance machine (synRM) has no rotor excitation to create any flux, Ψ_r, or torque on its own. Instead, all the torque comes from the saliency, the second torque component described in Equation 2.1. Usually, air gap channels are used in the rotor to create paths for the flux along the direct axis, maximizing the difference between the direct and quadrature axis inductances, resulting in a greater reluctance torque.

The simple and robust structure of the synchronous reluctance machine (synRM) is one of its main advantages. This is because the rotor consists of only one uniform part which also makes the synRM simple and cheap to manufacture. It requires only a simple vector controller and a standard 3-phase power converter [31]. The efficiency is good [32] and the field weakening range is wide [33].

However, the torque density and power density are significantly lower than that of an IPMSM [34]. The constant power speed range is not wide. A challenge in the design of the air gap channels is to combine the optimization of the reluctance with enough mechanical strength to endure the forces of a high rotational speeds, especially for larger machines [32].

To improve the performance, the rotor to stator air gap need to be reduced.
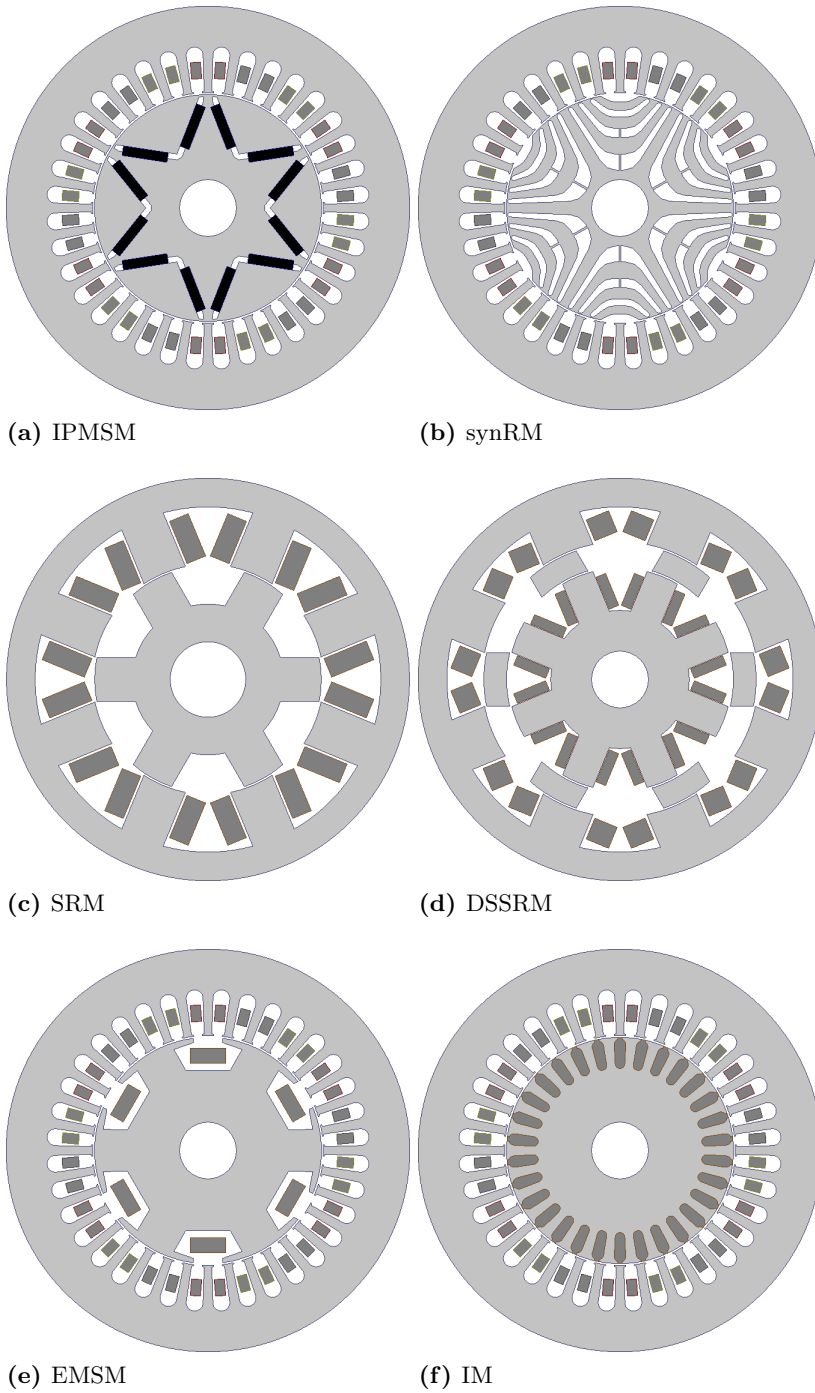
(a) IPMSM

(b) synRM

(c) SRM

(d) DSSRM

(e) EMSM

(f) IM

Figure 2.1: The machine topologies studied in this chapter.

Since the torque of a synRM is built on reluctance differences that are sensitive to magnetic saturation, synRM have generic issues with overloading capability. These things can be improved with material choices and materials, but that potentially takes away some of the advantage of a simple and cheap construction.

[32] from 1998 claims that the synRM is a strong competitor for potential drives for EVs, thanks to its cost, weight and efficiency. [33] in 2015 also holds synRM as one of the most promising PM-less topologies for hybrid electric vehicles (HEVs), much thanks to its low cost and relatively good performance in other aspects.

2.3   Switched reluctance machine machine

The switched reluctance machine machine (SRM), like the synRM, also gets its torque from saliency, but in this case double saliency, from both the rotor and the stator. The machine typically has from two to five phases (ϕ), $n\phi$ poles and $n(\phi+1)$ stator teeth. This means that if one pole is aligned with a stator tooth, a total of n poles are aligned that way, while the other poles are more or less miss-aligned. Unlike the synRM that has a synchronously rotating stator field, the switched reluctance machine machines (SRMs) field is created in pulses from the stator teeth being a certain angle ahead of a rotor pole, making the field pulses move opposite the rotational direction. This topology has been known for a long time, but as switch devices are becoming more cheap and efficient, it has gained in popularity lately [35].

Like the synRM, the SRM also has the advantage of a simple and uniform rotor, lacking the assembling of extra rotor parts like windings or permanent magnets [36]. Further, the SRM also lacks the narrow air gap channels that the synRM implements to increase the saliency. This makes the SRM extremely robust, allowing very high speeds from a mechanical perspective [33]. It can operate in high temperatures and harsh environments [37] and is simple and cheap to manufacture [38]. The fault tolerance is high [35] and maintenance cost is low [39]. The constant power range is wide [39], even extremely wide with some designs [40]. The simplicity of the machine makes it easy to recycle [38].

Due to rotor iron losses [36] and copper losses due to the magnetizing current that is drawn from the stator, the efficiency of a SRM seldom exceeds 90 % [33] [39] [38]. The torque and power densities are relatively low [33] [35] [38] [37], so more volume and weight has to be allocated for the machine in high torque or power vehicles. Several articles [33] [38] [41] [36] also mention the demand for

non standard power electronics as a drawback of the SRM. This is because of the discretized motion of the machine, which also results in a substantial amount of torque ripple, noise and vibrations [33] [39] [38] [41] [36].

The efficiency, however, can be increased to 92 % [34] but with a current density of 33 A/mm^2, or 96 % [38] with a good design and choice of core materials. The efficiency is generally higher at high speeds. The torque density is comparable to IM [39] and can be improved (to 45-61 NM/l) in liquid cooled machines. [42] says that the torque and power density (per volume) can match the IPMSM in the 2009 Toyota Prius, but with weight and current density increased by 15-25 % compared to the Prius. By using high silicon steel and smaller air gaps (0.1 mm) the SRM is said to outperform IPMSMs in efficiency, torque density, size and operation area [41].

In EV application [40] states in 2002 that the SRM is superior to IMs and brushless DC machines. According to [36], in 2007, SRMs have a significant potential for use in vehicle propulsion systems. But in 2015 the SRM was not considered for the FreedomCar 2020 targets made by the US Department of Energy, due to the low torque density of most designs [33].

2.3.1   Double stator switched reluctance machine

The double stator switched reluctance machine (DSSRM), works like the SRM, but with two stators, one outside the rotor and one inside the rotor. The rotor consists of a reluctance piece construction running in the gap between the two stators, the rotor pieces being pulled around by the pulses from both sides.

Because of its many advantages, much research is being made on different SRM designs, in order to overcome the problems. Facing one of the problems of the SRM, the amount of forces acting radially on the rotor, the double stator switched reluctance machine (DSSRM) was invented [43]. The double stator design can considerably increase the energy conversion efficiency, meaning more forces will act tangentially instead of radially on the rotor [44] [45]. This results in less vibrations and noise [39]. The deformation is 7 times smaller [46] and the torque ripple up to 19 times smaller [47] than in conventional SRMs. Another advantage is that the flux path becomes shorter [35] which results in lower inductance and reactive power requirements from the inverter [34]. The torque density is higher [39] as well as the power density [43] [37].

On the downside, the structure is more complex than the conventional SRM [34]. This affects the cost which is estimated to be 20-30 % higher, the end

windings which are longer and structural integrity as the rotor is built by many small pieces. Although having lower torque ripple than the SRM, the torque pulsation is still considered as a disadvantage, but it is still has potential to be reduced with more optimization of the design [37].

2.4   Electrically magnetized synchronous machine

The electrically magnetized synchronous machine (EMSM), or electrically excited synchronous machine gets its rotor flux, Ψ_r, from a DC current running in rotor windings exciting the rotor. The rotor windings are either fed conductively via slip rings or electromagnetically with a rotating transformer.

The most obvious advantage of the EMSM is the ability to control the rotor excitation, Ψ_r. Compared to a PMSM, this allows boosting the starting torque [48] and extending the speed range without utilizing field weakening operation with stator current components [18]. It also enables lowering the iron and excitation losses at partial load. Together, these abilities enables a large operation area with an extended field weakening area [49], wider than the IM [50]. Compared to the PMSM, the EMSM has low idle losses, no danger of demagnetization and no risk of high voltage when compensating for back emf. As a synchronous machine, the control is simple and robust [18] with good ability to control reactive power and back emf [51]. The structure is simple and reliable [48]. Since the EMSM has no PM, it has a potential of saving costs [51] [50]. This potential is broadened by the machines high power factor over the whole speed range, which allows a reduced inverter current size and potentially lower drive system cost.

One of the biggest disadvantages of the EMSM is a direct consequence of the biggest advantage. The excitation windings in the rotor that gives the machines its controllability also cause losses that lower the efficiency [48] [34] [18] and generate heat. The rotor copper losses is roughly as big as the stator copper losses [51], giving it a lower efficiency at all speeds compared to PMSM, if no rotor excitation current control is applied [50]. The heat generated in an inner rotor has has to travel a farther distance to the exterior, which makes the machine harder to cool. The thermal constraints are likely to force a compromise in torque density [52]. The EMSM has $\sqrt{1/2}$ the torque density of a PMSM if the total copper losses are equal [53]. Peak torque is lower than IPMSM [50]. The windings also require an extra DC converter and a rotary transformer [34] or slip-rings [52] that in turn require extra space and possibly also extra maintenance [51].

However [48] states that slip-rings do not require maintenance, since the same type are used in synchronous generators, where more experience is possessed. [18] says that slip-rings "are virtually maintenance free". If a rotary transformer and a diode rectifier is used, a high frequency reduces the size of the transformer [34]. The rotor excitation can also be fed in series with the stator, which takes away the need of an extra DC converter, but reduces the controllability [54].

When it comes to efficiency, the higher copper losses can be limited to when the machines runs in full load operation [49]. Using the optimal rotor excitation current control, mixed with stator field weakening, above 89 % effiency can be achieved in virtually all operation points above kneepoint, with a top efficiency of > 94 % for the machine [55]. While the top efficiency is not as high as in a PMSM, the high efficiency operation area could be bigger and better situated for some uses, and compared to other topologies, like the IM, the efficiency is overall higher in the EMSM [48].

In 2014, Renault was the only manufacturer with an EMSM in the EV/HEV market [34]. Since in 2015 Renault Zoe was the number 2 most sold EV in Europe [1] and number 7 in the world so EMSM is still represented in a fair amount of the total EV market. [55] means that EMSMs are of great interest for EV, most thanks to the lack of PM and the adjustable flux. [18] concluded in 2011 that the EMSM performs better than IM, which was market predominant at the time, and that the future price trend of permanent magnets will decide whether there is a market breakthrough for EMSM.

2.5   Induction machine

The induction machine (IM) has rotor windings, like the EMSM, but they are not externally fed. Instead the exciting current is induced by the stator field. The excitation can rotate within the rotor, moving from one rotor winding to another, creating a slip between the stator field frequency and the rotational frequency. The rotor windings are typically made of a squirrel cage forged or assembled of copper or aluminum, within the rotor core.

The IM has a simple and robust structure [34]. The rotor needs no supply [33], as the EMSM does, which helps to make it reliable, proof of hostile environments and relatively maintenance free [18] [56]. Materials and manufacturing are cheap [39] [57]. The machine is mature and standardized [36], since it is widely used in several markets, not only in EV applications [58]. It can reach peak torque and high speed performance similar to IPMSM [33] with the same current density

and lower cost [34]. The high speed operation area is wide [56] [57], and the efficiency is better in the high speed region [39].

The design adjustments required to enable high speeds forces trade-offs [57]. Among those, the peak torque may not meet the requirements with current and temperature limits [33], and the efficiency is decreased [18]. Overall the efficiency is low compared to PMSM [58], because of the copper losses in the magnetizing current in the cage in the rotor [34]. The rotor copper losses are, like in the EMSM, as big as the stator copper losses [51], where they are also difficult to cool [39]. Other than efficiency, the power density [57] and torque density [39] are lower and weight is higher compared to a PMSM with the same current density [34]. The controllability is not as good as in synchronous machines [57], especially at high speeds there is room for improvements of the current control [56] where the machine can otherwise stall at full current [58]. The power factor and inverter usage is low, due to the high current and voltage ratings requirements [34].

Some of the balancing when designing for better efficiency can be explained by trying to make the copper and iron losses as equal as possible. The copper losses are highest at base speed, so the iron losses should be higher than the copper losses at low and high speeds. The key to achieving high speeds is minimizing leakage reactance. [36]

In EV and HEV applications, the IM is already widely used and accepted as one of the most promising candidates [56]. Among the several manufacturers using IMs today the manufacturer of the top selling EV model in 2015[1], Tesla, is found.

2.6   Summary of topology literature study

There are several good candidates for PM-less machines for electrical vehicles, and no clear winner among them. All topologies presented here have some nice advantages to highlight, but also disadvantages that make the special requirements for each application crucial for where the choice falls. Some of the topologies are mature and widely used, some are barely more than concepts in its cradle. They are all promising in their own ways, but they are also all in need of more research and development.

If the thermal problems of the EMSM are addressed, the potential for the topology is great. Direct cooling is a potential solution to thermal problems in electrical machines. In the next chapter the principle of direct cooling and a

concept thereof is explained, which sets the prerequisites for the rest of the thesis where the possibilities of improving the EMSM's performance by addressing the thermal problems are studied.

Chapter 3

Direct cooling

In this chapter, the principle of direct cooling, some existing implementations of direct cooling in literature and the concept that is further studied in the remaining part of the thesis is explained and presented.

3.1 Principle of direct cooling

Conventional cooling of electrical machines is located at the exterior of the machine. The simplest form is just letting natural or forced convection of air at the outer surface of the stator (assuming an outer stator, inner rotor machine). It is also quite typical to force air, water or another coolant fluid through channels running axially through the outer part of the stator. The magnetic circuit needs to be short as well as having as much core material as possible to maximize the flux and minimize the core losses for optimal performance. Sacrificing any volume deep inside the machine for a cooling system is often not worth it.

As mentioned in the introduction (Chapter 1.1.3), combustion engines are easier to cool effectively, resulting in overheating not being a problem in normal combustion engines cars, much because the cooling can be located close to both where the heat is generated and the thermally sensitive parts.

In an electrical machine, the parts generating the heat is partly the core itself, but more so the windings in which current create the magnetic field. The parts sensitive to high temperatures are in part the possible permanent magnets, which will suffer permanent loss of strength if operating at high temperatures typically ranging from 80 °C to more than 200 °C depending on the intrinsic

Steel tube

Coolant

Litz wires, $d_\mathrm{w} = 0.5$ mm, $k_\mathrm{f} = 0.77$

8 mm
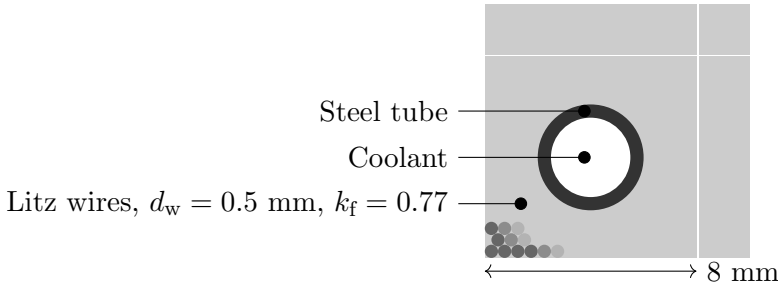
Figure 3.1: Illustration of direct cooling with Litz wires wrapped around a steel tube for cooling.

coercivity [59] [60]. Another part sensitive to temperatures are the copper windings, for which the lifetime of the insulation varnish will be shortened and in worst case come to an abrupt end at high temperatures, typically around 180-200 °C depending on the insulation type [61] [62].

This means the copper windings are both heat generating and heat sensitive. In addition, in an electrically excited machine, the excitation windings are situated near the center of the machine, while the cooling is conventionally dissipated to the exterior of the machine. If the heat could instead be dissipated directly from the rotor windings, the performance could be substantially less impeded.

3.2   Direct cooling in literature

Many concepts of direct cooling have been suggested and studied. One example is placing tubes for a liquid coolant among the windings. [63] did so in a SRM designed for vehicle propulsion and managed to improve the torque density and increase the current density in the stator slots to 9 A/mm^2 continuously. The outcome is a result of balancing the torque density and the efficiency of the machine. In a double stator, single rotor, axial flux PM machine [64] steel tubes for water cooling are placed among the thin copper Litz wires in the stator slots (Figure 3.1) to increase the torque density and prolong the winding insulation lifetime by lowering the temperature, at 8.8 A/mm^2. In a later study [65] 14 A/mm^2 was reached with a maximum winding temperature of 155 °C, compared to 4 A/mm^2 in the original machine with conventional cooling.

Another alternative to conventional exterior cooling is using radial cooling ducts for air or other coolants through the core (Figure 3.2). This was studied [66] with air in a PMSM wind turbine generator and found that in addition to designing the dimensions of the ducts for efficient cooling, a complex correlation with the
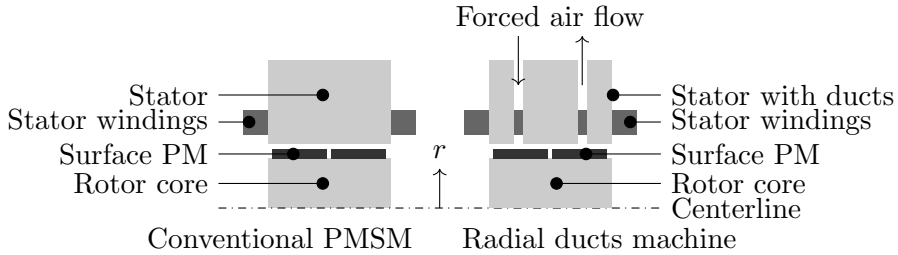
Figure 3.2: Cross section of simplified principle of direct cooling with radial ducts, inspired by [66].
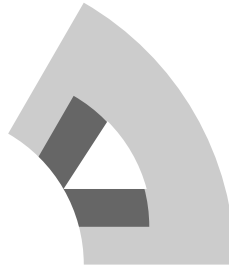
Figure 3.3: Illustration of section of SRM stator with a triangular cooling "prism" between the windings.

core saturation had to be taken into account. In another PMSM wind turbine generator [67] demineralized water was used in rectangular copper windings extracted over steel tubes to keep the winding temperatures below 90 °C and the permanent magnets below 60 °C with a current density of 7 A/mm^2.

In another study [68] an axial triangular space between the windings of a SRM (Figure 3.3) is cooled to a 50 % lower temperature and even though 25 % of the slot volume is used for the coolant channel, the current density is increased with 30 % and hence the overall torque and power density is increased.

3.3 Laminated windings

Another direct cooling concept is developed at the author's department at Lund University, the so called laminated windings [69][70][71]. The idea is that thin layers of copper or aluminum make up the windings and that air is blown in the space between the layers, illustrated in Figure 3.4.

The laminated windings can be manufactured and implemented in several ways, often implying rolling or folding them to fit the slots and winding configuration.
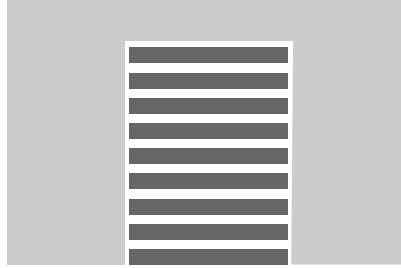
Figure 3.4: Illustration of cross section of laminated windings in a rectangular slot
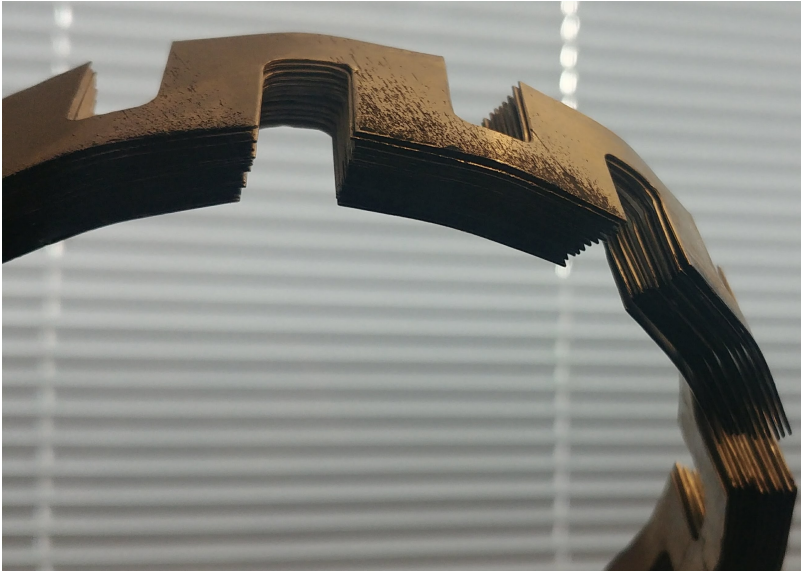
Figure 3.5: Example of rolled laminated winding for a machine with a short active length.

A couple of examples are shown in Figures 3.5-3.6.

The experience from the work on laminated windings is that they show a great theoretical potential, enabling current densities up to 30 A/mm^2. Experiments show that the basics of the concept works, but the theoretical potential has been difficult to convert to reality. In practice the distance between the layers have proven to be far from equal. Ideally, the layers and spaces between the layers should be very thin. But the thinner the conductor, the harder it is to keep them perfectly flat, or following a certain arc, and the thinner the space between the layers, the more relative difference from small imperfections. If the space between two layers are thinner than the others, significantly less air may pass in that space, leading to a dangerous hotspot that can damage the insulation of the windings. Also leakage proved to be a problem. Difficulties to

Figure 3.6: Example of folded laminated windings for a machine with long active length.

seal the inlet perfectly and to not let any air slip into the slot opening or air gap of the machine increased with narrower spaces between the windings.

During the work with the laminated windings this has led to increasing dimensions with thicker conductors and larger spaces between them, even though it is less optimal in the theoretical case, because the thicker laminated windings are sturdier so that in turn the cooling capabilities are more predictable.
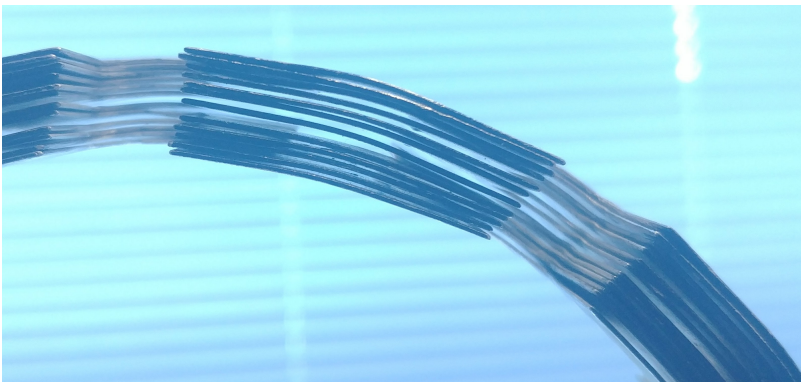
Figure 3.7: Example of rolled laminated winding with uneven spaces for air flow.

Figure 3.8: Example of folded laminated winding with relatively even spaces for air flow.
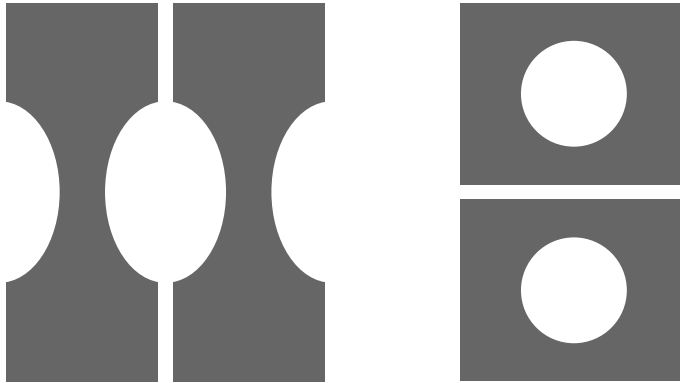
Figure 3.9: Left: Cross section of two rectangular winding with concave indents along the sides. Right: Cross section of two rectangular hollow windings with inner circular coolant channels.

3.4   Renewed ideas on parallel air-flow direct cooled windings

To build on the potential of laminated windings and address the problems, a couple of other concepts have become interesting to study further. Since the distance between laminated windings is difficult to ensure in practice, the shape of the windings themselves needs to assure the cooling channels are kept intact. Two basic ideas are illustrated in Figure 3.9.

Both ideas result in circular or elliptic coolant channels running along the windings, that will stay intact once the windings are squeezed into the slots. That means they both can be thermally modeled the same way, as solid copper blocks

Figure 3.10: Photo of a 6x6 mm rectangular hollow winding with 2 mm radius inner air channel.

with a number circular or elliptic channels running through - if the interface between the individual conductors and the insulation thickness is neglected and if the two outermost half ellipses are assumed to be equivalent to one whole ellipse; and that the area around every channel can be modeled as one smaller block of copper with one single circular or elliptic channel through it - if no heat exchange at the boundary is assumed, so that all the heat generated in the windings will dissipate into the coolant. The thermal models will thus be similar to the photo seen in Figure 3.10.

A number of different coolants can be considered as coolants, but this thesis studies the case with air only. This is mostly a practical choice, since air is easily available for experimental validation. The fact that liquid coolants like water or oil are better for cooling applications will generally mean that if the proposed concepts works with air, they may perform even better with water or oil for further studies.

One of the drawbacks in the properties of air when used for cooling is that the heat capacity per volume is very low, in comparison to oil and water that have higher specific heat and orders of magnitude higher density. This means air will increase quickly in temperature. Since it is important to not let the insulation overheat, the air will quickly reach the temperatures where the lifetime of the
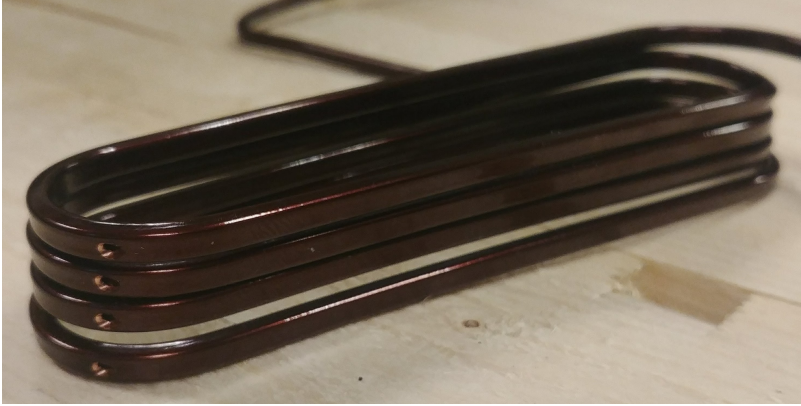
Figure 3.11: Photo of coiled rectangular hollow winding with drilled holes creating parallel cooling channels.

insulation will suffer [62]. In several of the examples of direct cooling mentioned above (section 3.2), a tube with liquid coolant could run several turns throughout the machine and still be able to keep the windings cool by the outlet. For air, the cooling channels need to be shorter.

For that reason, the cooling channels will run in parallel through the active (axial) length of the machine, in the work of this thesis. For the indented windings, the channels will open up at the end turns of the machine, creating inlets and outlets for the air. For the hollow windings however, holes have to be drilled in the end windings. An example of this is shown in Figures 3.11 and 3.12.

Only the active (axial) length of the machine is modeled. In a practical application of the proposed windings in a machine, the winding end turns will have an effect on natural convection, heat generation, inlet of the air flow, among other things. Those effects are neglected in this model. A compressor or fan will increase the air temperature with the pressure rise, so the placement of it, as well as its efficiency, will matter to the system. The air can either be circulated and cooled between outlet and inlet, or be brought from the surrounding through a filter. But in this thesis, neither of these questions will be covered.

This concludes the prerequisites and delimitations of the direct cooled winding concept for which the air cooling model is presented in the next chapter.

Figure 3.12: Close-up photo of end windings of coiled hollow rectangular winding with drilled holes for parallel air inlets/outlets.

Chapter 4

Model and analysis of air-cooled windings

This chapter presents the model developed for the proposed direct cooled windings, starting with the necessary heat transfer theory to describe the possibilities and inadequacies embedded in the empirical correlations that are used in the model. The empirical model is combined with a lumped parameter model and the accuracy of the combined model is briefly compared to experimental results.

The final part of the chapter presents and discusses the results from the model and the conclusions from the air cooling model that are integrated in the subsequent machine design of the next chapter.

The majority of the content of this chapter is published as a conference paper [72].

4.1 Modeling of heat transfer

For an electrical engineer, Ohm's law is one of the foundations of the universe and analogies for Ohm's law are identified in basically every field of physics. Heat transfer is no exception. A very fundamental relation for heat transfer through a given area can be written as equation 4.1 where Q/A is the heat flux in W/m^2 between two points (or the current in the Ohm's law analogy), ΔT is the difference in temperature in K between the same points (or the voltage in the analogy), while k will take different forms depending on the path of the heat, given in W/m^{2}K (and the equivalent of the inverse of the resistance).

$$\frac{Q}{A} = k \cdot \Delta T \tag{4.1}$$

If the heat travels through is thermal *conduction*, k can be expressed as equation 4.2 where λ is the heat conductivity given in W/mK and L is the length of the heat flux path (comparable to the resistance's relation to the resistivity).

$$k = \frac{\lambda}{L} \tag{4.2}$$

If the path of the heat is *radiation*, the expression takes the form of equation 4.3 where ε is the emissivity coefficient and Stefan-Boltzmann's constant $\sigma = 5.6703 \cdot 10^{-8}$ W/m^{2}K^4. T_{body} and T_{amb} are the temperatures of the radiating body and the surrounding ambient temperatures (between which temperatures ΔT is also defined).

$$k = \varepsilon\sigma(T_{\text{body}}^2 + T_{\text{amb}}^2)(T_{\text{body}} + T_{\text{amb}}) \tag{4.3}$$

Finally, if the heat takes the path of *convection*, $k = h$ where h is the heat transfer coefficient in W/m^{2}K. In this case, the fundamental relation (eq 4.1) is known as Newton's law of cooling. If the convection happens through forced convection in a pipe, the heat transfer coefficient is as in equation 4.4 where D is the diameter of the pipe, λ is the heat conductivity of the fluid and Nu is the Nusselt number, which is a dimensionless number that represents how easy the heat will spread from the wall to the fluid. The heat spread into the fluid (in heat transfer and fluid dynamics air and other gases counts as a fluid, as opposed to solids) depends on both the fluids convective and conductive heat transfer, since the heat is both conducted throughout the fluid as well as spread as the fluid mixes in eddies and vortices. The way the fluid behaves is unpredictable, and empirical models have proved to compose better estimations of the behavior than physics models.

$$h = \frac{\text{Nu}\lambda}{D} \tag{4.4}$$

The fluid temperature distribution along the radius of the pipe, T_{f}, will vary along the length of the pipe, as the flow develops. The exact distribution is hard to determine, but that is not necessary since the bulk temperature of the fluid, T_{b}, the average of the temperature distribution along the radius, is what
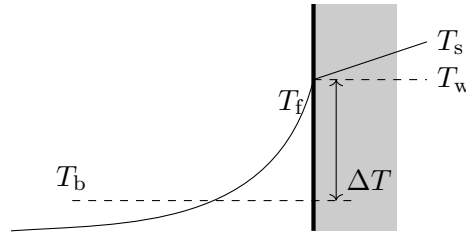
Figure 4.1: The temperature profile along the radius of a pipe and the definition of the solid temperature T_s, wall temperature of the solid T_w, fluid temperature T_f, bulk temperature of the fluid T_b and ΔT in the solid/fluid interface of a pipe.
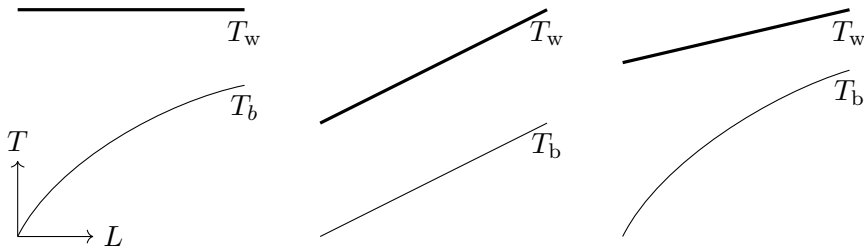

Figure 4.2: Temperature distributions along the length of the pipe. Left: Example of T_w constant. Center: Example of Q (or ΔT) constant. Right: Example of realistic case.

defines ΔT together with the temperature of the solid at the interface, as seen in Figure 4.1.

To solve a heat transfer problem, a choice between two options has to be made. That is if either the wall temperature of the solid (T_w), or the heat flux from the wall to the fluid (Q), is going to be assumed to be constant. Neither is true in reality (as shown in Figure 4.2), but one of them has to be assumed to be a better estimation.

In the work of this thesis, the assumption of the wall temperature being constant is made. To determine the heat transfer coefficient, the Nusselt number has to be obtained. The empirical models for the Nusselt number are different depending on the situation. Things like the dimensions of the pipe, the properties of the fluid and the rate of turbulence will affect which model that gives the best estimation.

The important parameters of the pipe's dimensions are the length, the hydraulic diameter and the ratio between them. The hydraulic diameter D_h, equation 4.5, is the same as the inner diameter of the pipe if its cross section is circular. If the pipe has another shape, D_h is an equivalent diameter that will result in the same hydraulic behavior as a circular pipe with the same diameter. C_{wp} is the

circumference (wetted perimeter) of the cross section through which the fluid flows.

$$D_{\mathrm{h}} = \frac{4A}{C_{\mathrm{wp}}} \tag{4.5}$$

Some of the properties of the fluid are represented in the Prandtl number, which is given by the relation between the thermal diffusion rate and the fluids dynamic viscosity, μ, obtained by equation 4.6.

$$\mathrm{Pr} = \frac{\mu c_{\mathrm{p}}}{\lambda} \tag{4.6}$$

The rate of turbulence is determined through the Reynolds number, equation 4.7. The Reynolds number is in itself dimensionless and depends on the fluid's mean speed through the cross section area (u_{m}, given in m/s), the diameter of the pipe (D_{h}) and the fluid's kinematic viscosity (ν).

$$\mathrm{Re} = \frac{u_{\mathrm{m}} D_{\mathrm{h}}}{\nu} \tag{4.7}$$

The Reynolds number is crucial when determining the Darcy friction factor, f. The friction factor is a proportional factor to the pressure drop of the fluid along the length of the pipe due to the resistance of the fluid's friction against the pipe walls. The friction factor is also an important part of the Nusselt number, which is evident in the following sections.

4.1.1   Empirical model

An empirical-numerical model is built to approximate the heat transfered from the copper windings to the air channels for a given air speed.

Laminar flow

For Reynolds numbers lower than 2300, the flow can assumed to be laminar, meaning that the fluid is moving only axially, and that radial or tangential directions of the flow can be neglected [73]. The fluid near the center of the pipe flows faster, while the local flow rate of the fluid closest to the walls of the pipe
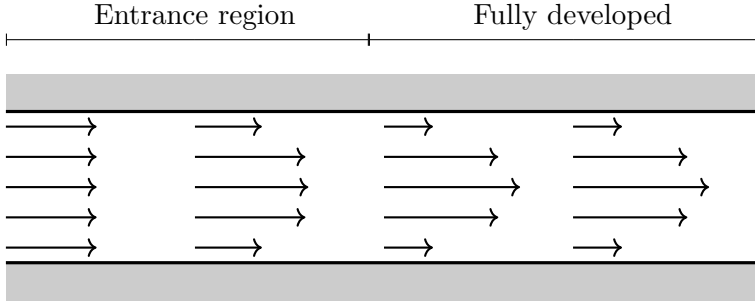
Figure 4.3: Velocity profile for the entrance region and fully developed laminar flow.

approaches zero. Laminar flow is typical for lower flow rates and pipes with small diameters.

The geometry of the pipe will decide the dimensionless constant C. Circular pipes results in a value of 64, while ellipses will results in a higher value. With C, the Darcy friction factor, f, is then obtained through equation 4.8.

$$f = \frac{C}{\mathrm{Re}} \tag{4.8}$$

In laminar flow, the Nusselt number will adopt a constant value of 3.656 for long pipes. But at the entrance into the pipe, the flow will need a distance to develop fully. During this length, the entrance length, the Nusselt number will be higher. For pipes with a length less than roughly 100 times the diameter, the entrance length can not be neglected. In these cases, the local Nusselt number along the pipe can be obtained with Hausen's formula, equation 4.9 [74].

$$\mathrm{Nu} = 3.656 + \frac{0.0668 \mathrm{RePr} \frac{D_\mathrm{h}}{x}}{1 + 0.04(\mathrm{RePr} \frac{D_\mathrm{h}}{x})^{2/3}} \tag{4.9}$$

The entrance length is defined be the length it take from the entrance until the velocity profile has stabilized. At the entrance the flow has the same speed in the center of the pipe as near the walls. The flow close to the walls is slowed down more and more along the entrance length. The entrance region and fully developed laminar flow is illustrated in Figure 4.3, where the two rightmost profiles are identical, meaning the flow is fully developed from there on.

Transitional flow

When the Reynolds number is in the region between 2300 and 4000, the flow
in a pipe is transitional, meaning it is neither fully laminar, nor fully turbulent.
The flow in the center of the pipe is be turbulent, while the flow close to the
surface is laminar.

The friction factor for transitional flow is difficult to determine and very little
theory is established for the region [73], much because transitional flow is hard
to predict, since the mix of laminar and turbulent flow in the pipe can change
back and forth over time [75] and be triggered by minor disturbances in the
pipe or its surrounding [76]. In this thesis, to not overestimate the friction
factor in transitional flow, the friction factor is interpolated linearly from the
friction factor of laminar flow at Re = 2300, using eq 4.8, to the friction factor
of turbulent flow at Re = 4000, using eq 4.12. This results in equation 4.10.

$$f = \text{Re} \cdot 8.00883 \cdot 10^{-6} + 0.0094057 \tag{4.10}$$

The choice to interpolate the friction factor in the transitional region was based
on the collection of experimental data for turbulent flow through pipes in [77].
The Nusselt number for the transitional region was calculated with Gnielinski's
correlation (eq 4.11).

Turbulent flow

From Reynolds numbers of 4000 and above, the flow can be considered turbulent
and thus more predictable than the randomly mixed transitional flow. For
the Nusselt number in turbulent flow, Gnielinski has established a well-known
correlation, equation 4.11.

$$\text{Nu} = \frac{f}{8} \frac{\text{Pr}(\text{Re} - 1000)}{1 + 12.7\sqrt{f/8}(\text{Pr}^{2/3} - 1)} \tag{4.11}$$

Even though Gnielinski's correlation neglects the entrance region it has proven
to provide the most accurate estimation of the Nusselt number for smooth pipes
over a wide region of Reynolds numbers [76]. The entrance region would locally
result in a higher Nusselt number, which in turn would increase the heat transfer
coefficient and thus the cooling abilities. Using Gnielinski's correlation this
way results in a conservative model, that does not overestimate the cooling

capabilities of the system. Gnielinksi's correlation for turbulent flow should be used with Petukhov's correlation for the friction factor, equation 4.12.

$$f = \frac{1}{(0.79 \ln{(\mathrm{Re})} - 1.64)^2} \tag{4.12}$$

Freshly drawn copper has an absolute roughness of $\epsilon_\mathrm{r} = 0.0015$ mm [78] which in the range of $2 \leq D \leq 10$ mm will result in a relative roughness of $0.00015 < \epsilon_\mathrm{r}/D < 0.00075$. In the mentioned range of diameters and the expected range of air speeds ($20 < u_\mathrm{m} < 110$ m/s), the Reynolds number is not expected to exceed 20 000. Within that range, the difference between perfectly smooth pipes and drawn copper is negligible, as seen in a Moody Chart [79], which means that the Petukhov correlation will make a good estimation of the friction factor.

Implementation in model

The model is implemented by dividing the pipe into shorter sections, as illustrated in Figure 4.4, calculating the Reynolds, friction and Nusselt numbers as described above, as well as the heat transfer coefficient for each section separately (eq 4.13). For each section also the pressure drop (eq 4.19), heat absorbed by the air (eq 4.15) and the temperature rise of the air is calculated (eq 4.16). Depending on the pressure and the bulk temperature of the air, the density (eq 4.17), speed (eq 4.18), heat conductivity and viscosity is updated. The heat conductivity and viscosity is interpolated from table data. From here on, the surface temperature of the solid will be called T_c (for copper) instead of T_w.

$$h = \frac{\mathrm{Nu}\lambda_\mathrm{air}}{D_\mathrm{h}} \tag{4.13}$$

$$dP = \rho_\mathrm{air}\frac{u_\mathrm{m}^2}{2}f\frac{dL}{D_\mathrm{h}} \tag{4.14}$$

$$Q = A_\mathrm{dw}h(T_\mathrm{c} - T_\mathrm{b}) \tag{4.15}$$

$$\dot{m} = u_\mathrm{m}A_\mathrm{pipe}\rho_\mathrm{air}$$

$$dT_\mathrm{b} = \frac{Q}{\dot{m}c_\mathrm{p,air}} \tag{4.16}$$
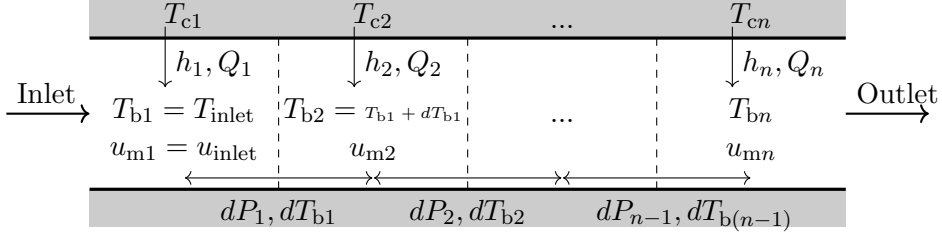
Figure 4.4: Sketch of the sectioned pipe and how some of the quantities develop.
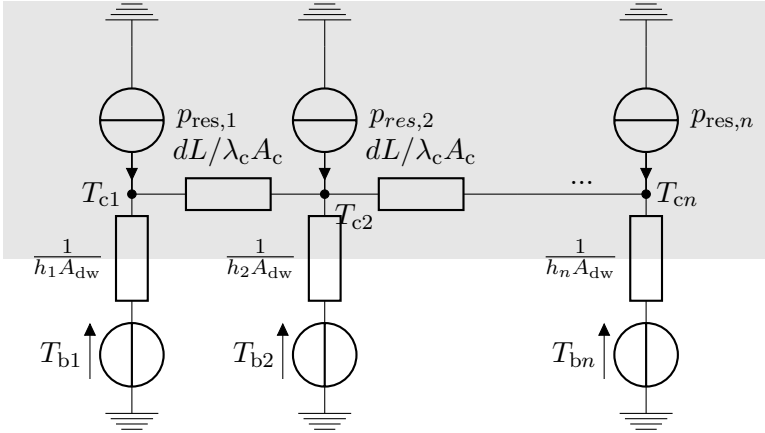
Figure 4.5: Lumped parameter model

$$\rho_{\text{air}} = \frac{P}{287.05 \; \nu} \tag{4.17}$$

$$u_{\text{local}} = u_{\text{inlet}} \frac{P_{\text{inlet}}}{P_{\text{local}}} \frac{T_{\text{b,local}}}{T_{\text{b,inlet}}} \tag{4.18}$$

4.1.2   Lumped parameter model

In addition to the empirical model, a lumped parameter model is used. The thermal network used is shown in Figure 4.5. The network can be represented by a matrix, from which the copper temperatures ($T_{c1}...T_{cn}$) in each node can be derived. In the lumped parameter model, the temperature dependent resistance for each section is calculated, which results in a non-uniform heat generation along the conductor ($p_{\text{res},1} \neq p_{\text{res},2}$ when $T_{c1} \neq T_{c2}$).

4.1.3 Combined empirical-lumped parameter model

The problem is solved by iterating between the empirical heat transfer model and the lumped parameter model. The inputs for the model is the current (which gives p_{res}), the inlet air speed u_{m1}, the inlet air temperature T_{b1}, the initial constant copper temperature, and the necessary dimensions. For the first empirical iteration, the copper temperature is constant along the length of the pipe and the air pressure is set as a linear pressure gradient based on the inlet air speed. The result of the empirical iteration is the air bulk temperatures ($T_{b1..n}$) and heat transfer coefficients for each section ($h_{1..n}$). This is fed into the lumped parameter model, which results in an update of the copper temperature distribution.

For the second iteration of the empirical model, T_c is no longer constant along the entire pipe, but each section is solved with a constant T_c of its own, equal to the corresponding copper temperature from the lumped parameter network. This is also the first time an approximation of the pressure in each section is known, which will play a part in updating the air properties.

This way, the system iterates back and forth between the empirical model and the lumped parameter model until it converges. Convergence of the copper temperature distribution is achieved after 17 iterations, if run with a number of sections resulting in a length of around 10 mm for each section. A sketch of the flow chart and the evolution of the temperature distributions is presented in Figure 4.6.

Purpose and conditions for the model

The purpose of the model is to find the necessary inlet air speed to keep the hottest part of the copper below a certain temperature. The point in keeping the hottest part of the copper cool enough is simply to not deteriorate the insulation of the windings. The point in finding the necessary inlet air speed is to derive the power needed to achieve the cooling. That power is later added as a loss in the machine, when calculating the efficiency of the machine.

The search for the lowest necessary inlet air speed is done by a golden section search algorithm. The search is performed between 0 and 110 m/s. The upper limit is set to approximately 110 m/s, because at higher speeds ($Ma^2 > 0.1$) the correlations between density, speed and pressure becomes more difficult to model in an accurate way, making convergence more difficult to achieve. One effect at this limit is that the air speed will not increase (at all, or very little)
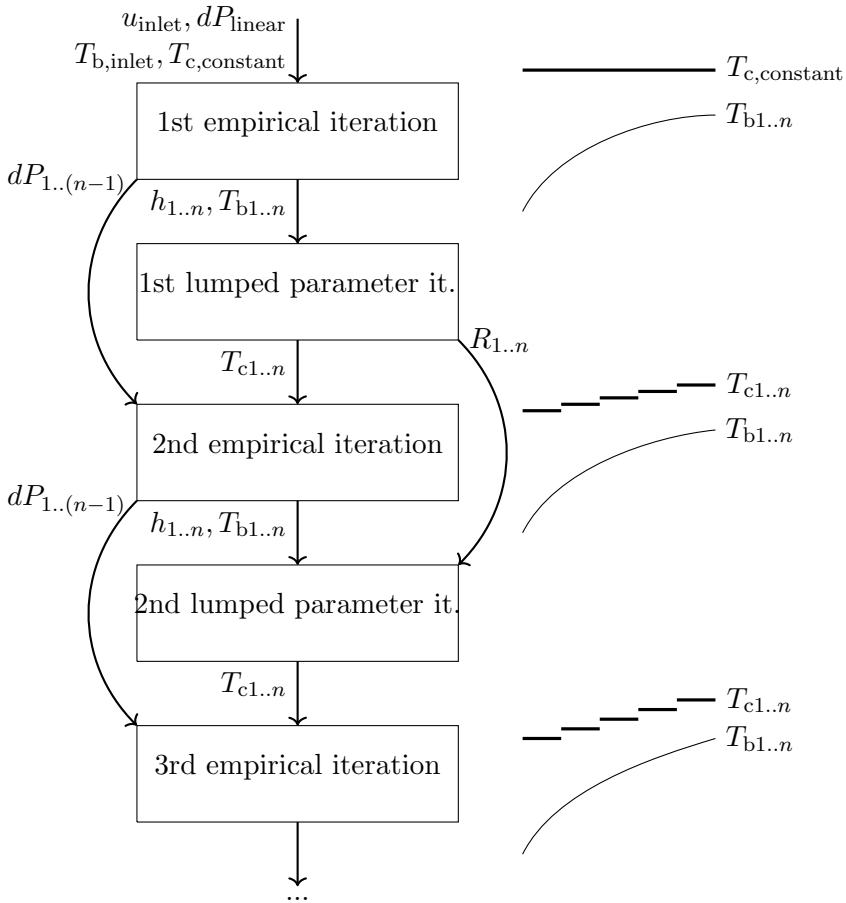
Figure 4.6: Flow chart of the combined empirical-lumped parameter model process.
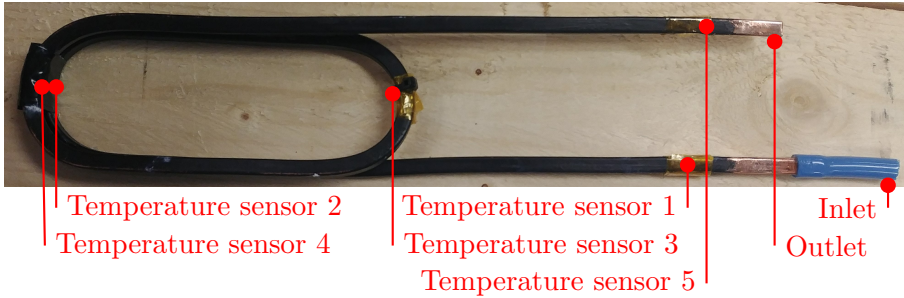
Figure 4.7: Photo of copper conductor used for the experiment.

with increased pressure. The cooling capability however will still increase as the pump power increases, because of the change in other air properties (such as density, thermal conductivity, specific heat), but not as much as at lower speeds.

4.2 Experimental validation

Experiments were performed on a drawn rectangular copper rod, shown in Figures 4.7 and 4.8. The dimensions of the rod are as follows; Length $L_{\text{rod}} = 870$ mm, side (height and width) $s = 6$ mm, inner channel radius $r_{\text{q}} = 2$ mm, and three $180°$ bends with radius $r_{\text{b}} = 18$ mm. The distance between the current connection terminals is $L = 848$ mm, which is the value that was used for the calculations involved in the experiment, post-processing and the empirical-lumped parameter model.

During the experiment, the copper temperature was measured on five spots, along with the pressure before the inlet. The experiment was performed in collaboration with the work of a master thesis [80].

The model described in the previous section assumes no heat exchange with the surrounding. In the experiment, however, some heat will escape to the surrounding air via natural convection and radiation, as well as to the terminals and cables for the current supply via conduction. The natural convection and radiation to the surrounding air was approximated to $h = 15$ W/m^{2}K, based on experiments in the aforementioned study [80].

With no data of the temperatures and dimensions of the current supply terminals and cables, the heat flux between those and the copper rod is impossible to determine with exact accuracy, but with the help of a small lumped parameter model with five nodes (one for each temperature sensor), an average heat flux
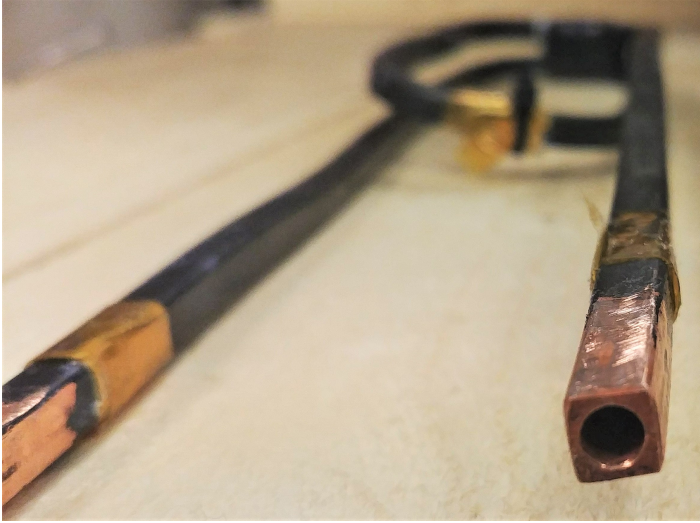
Figure 4.8: Photo of outlet cross section of copper conductor used for experiment.

from the inlet terminal could be estimated to $Q_{\text{in}} = 0.4$ W and the flux to the outlet terminal to $Q_{\text{out}} = 0.75$ W. These values (along with $h = 15$ W/m^{2}K to the surrounding air), were added to the lumped parameter model for the empirical-lumped parameter model.

Determining the air speed

The air speed was derived from the measured inlet pressure and equation 4.19:

$$dP = \rho \frac{u_{\text{m}}^2}{2} \left(f \frac{L}{D} + \sum k_{\text{b}} \right) \tag{4.19}$$

The centerline radius of the bend was measured to 18 mm while the internal diameter of the pipe is 4 mm. The bend loss coefficient k_{b} was determined to be 0.3 for each bend (and the number of bends were three) from table data [81].

If the pressure drop can be assumed to be linear along the pipe, the speed can be derived using the drop from the measured pressure at the inlet to the outlet pressure, which is the same as normal atmospheric pressure, and the whole length of the pipe, with the air density calculated for the inlet temperature $T_{\text{air,in}} = 20°$C and inlet pressure. This assumption however, would result in a too high inlet air speed, since the pressure drop is not in fact linear along the pipe. Since the temperature and the pressure varies along the pipe, the air

properties, density, speed and friction factor will vary too, which will in turn affect the pressure drop along the pipe. Lacking measurements of temperatures and pressures along the pipe, or other quantities necessary to derive the inlet air speed, the pressure distribution along the pipe was retrieved from the empirical-lumped parameter model. From there, it was found that the local pressure drop per mm along the pipe near the inlet was approximately 80 % of the average pressure drop per mm over the whole pipe (varying with $\pm 3\%$ from 80 % for the different cases in the experiment).

$$u_{\mathrm{m}} = \sqrt{2 \frac{0.8 \cdot dP}{\rho} \frac{1}{f \frac{L}{D} + 3 \cdot 0.3}} \qquad (4.20)$$

The air speed is thus derived with the correlation in equation 4.20 where dP is the pressure drop from inlet to outlet, $L = 848$ mm, $D = 4$ mm, and ρ and f are calculated from the inlet air pressure and speed with the same correlations as in the empirical model, via an iterative process. An initial f is chosen with an arbitrary number (a.k.a. qualified guesswork) for calculating a first iteration of u_{m}, leading to a Reynolds number and friction factor that determine a better estimation for dP and a new iteration of u_{m}, and so on. After 5 iterations, the third decimal of the air speed is stable.

Results and analysis

Seven combinations of current and air flow are tested. The measured temperatures from these cases are presented in Figure 4.9 along with the modeled temperatures from the model. Two levels of voltage was applied while varying the air flow, resulting in two different current densities (approximately 11.2 and 13.8 A/mm^2 with variations due to temperature depending resistance). In the presented results, the cases are sorted by air speed.

Firstly, for the three centermost temperatures from the experiments, the temperatures coincide well with the temperatures predicted by the model. For those three points along the pipe, the model on average predicts a temperature 7 K higher than the measured temperatures. It is a good sign that the model is on the conservative side, not overestimating the cooling capability of the system, leading to overoptimistic results.

A few more things are important to note about the results. The predictions of the endpoint temperatures are way off, which shows that the estimation of the heat flux to and from the current connection terminals is not accurate enough.
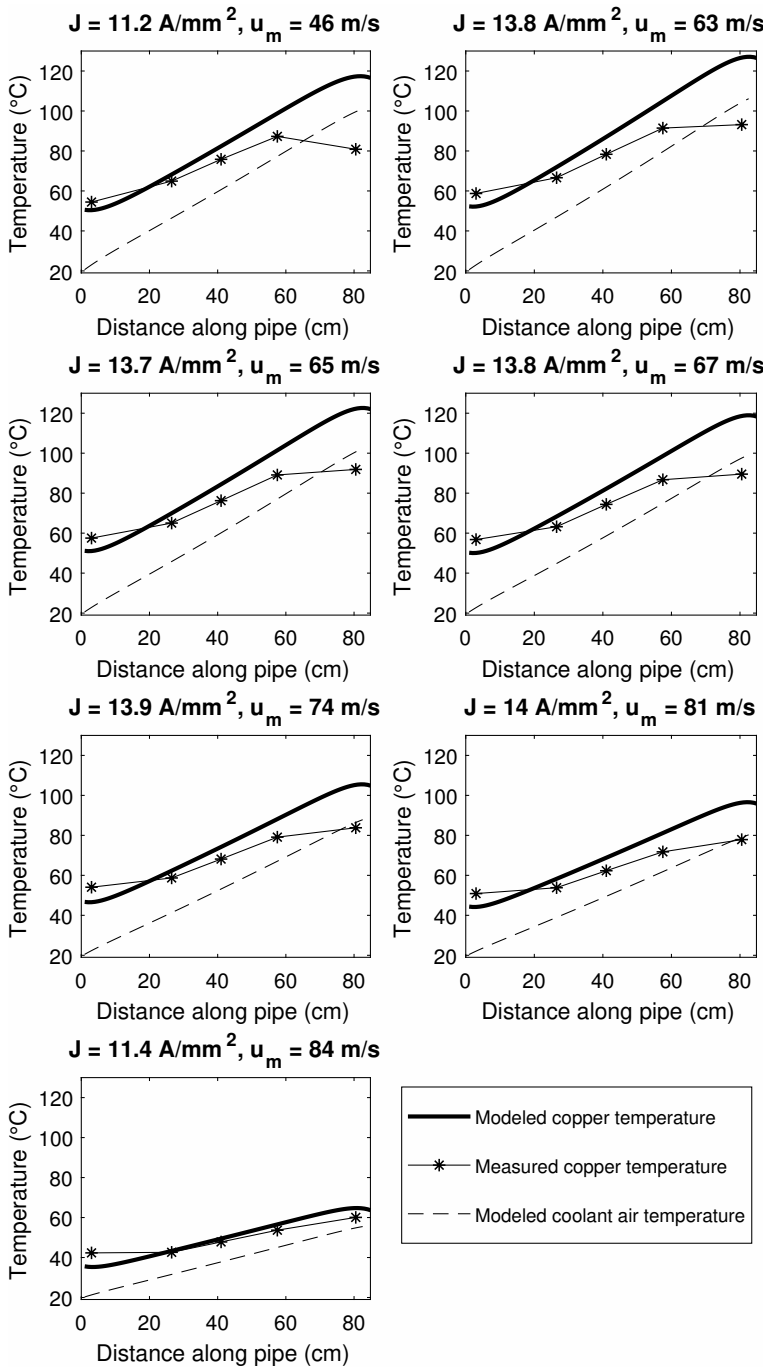
Figure 4.9: Comparison of experimental results and model results.

The temperatures at the inlet and outlet should therefore be ignored when assessing the model's accuracy to predict the temperature in a pipe with no heat exchange with the surrounding.

The three centermost measured temperatures have a slightly flatter gradient than the models prediction. The effect of the heat flux to the connection terminals is negligible in these points. It is more probable that the reason for the flatter gradient is the way the pipe is bent. In Figures 4.7 and 4.8, it is clear that the points for temperature sensors 2 and 4 are very close physically. There is no direct contact between the conductors at these points, but the convection and radiation between them will bring the temperatures of these points closer together than if the rod was straight, which the model assumes it is.

Conclusions on experimental validation

There are many uncertainties in the experimental data, such as the derivation of the air speed, the way the rod was bent, the convection to the surrounding and the heat conduction to the current connection terminals. Also, more combinations of current densities and air speeds would be desirable as well as data from conductors and channels with other dimensions, for the models accuracy to be assessed on a wider range. Unfortunately, there was no possibility to perform more experiments or retrieve more data at the time of the writing of this thesis.

Also worth mentioning is the fact that several parts of the experimental data had to be processed through the empirical model, mostly when determining f for the pressure drop, and the pressure drop distribution to derive the inlet air speed. Validating a model with the model itself is not the best practice in general, but in this particular case, the only way to get any experimental validation at all.

Lastly though, the model seems to predict the copper temperature surprisingly well. The uncertainties in the empirical correlations suggest a larger error margin, and for the purpose of the model it is, awaiting further experiments in the future, considered to be accurate enough. The point of the model is to estimate the power cost to keep the copper in the windings from overheating for a given current density, to in turn estimate the efficiency of an electrical machine utilizing the windings. And as already stated, the experiments show no reason to doubt that the model fulfills that purpose.
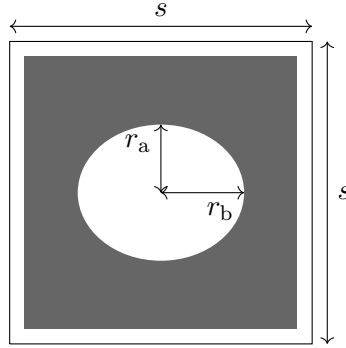
Figure 4.10: Sketch of the cross section of a conductor for the model, with a slightly elliptic air
channel and insulation (white frame).

4.3   Model results

The empirical-lumped parameter model is used together with the golden section
search algorithm to find the necessary air speed to keep the copper below 150
°C for various cases. Copper conductors with a square shaped cross section area
are modeled, as shown in Figure 4.10, with a insulation thickness of 0.1 mm on
all sides [61]. The side (s) of the conductors are varied from 2 to 6 mm, while
the length L is kept constant at 224 mm. The current density are varied from
4 to 18 A/mm^2, defined as equation 4.21, thus ignoring the cross section area
of the circular hole for the coolant air no matter what value r takes. The air
channel radii $r_{a,b}$ is varied so that the fill factor k_f varies as equation 4.22. The
model is run with two cases for the air channels, one with circular channels, and
one elliptic case where one radius is four times longer than the perpendicular
radius.

$$J = I/s^2 \tag{4.21}$$

$$k_f = \frac{s^2 - \pi r^2}{s^2} \tag{4.22}$$

This means that for a conductor with a given side s, the current is always the
same, independent of the air channel radius. If the channel is larger, the amount
of copper is decreased, and the resistance increased. If the channel is very small
the resistance is lower, but on the other hand more pump power is required to
push enough air through the channel to keep the copper cool enough. Where

is the right balance between the amount of copper and the size of the cooling channel? The model answers that and the results are presented in Figure 4.11.

Figure 4.11 shows the total power in an air cooled conductor, meaning the sum of the resistive losses and the pump power required to keep the copper below 150 °C. Along the x axis, the width (and equal height) of the conductor is varied. Along the y axis the air channel radius is varied, deciding the fill factor, which is the amount of copper divided by the conductors total cross section area. Each row represent a given current density J. Each column represent either a circular air channel ($r_a = r_b$) or an elliptic channel ($2r_a = r_b/2$). The total power is presented in W/mm^2 @ $L = 224$ mm, meaning the losses of the conductors of various dimensions are averaged per cross section mm^2, but summed along the whole active length, to make the results comparable. White areas show that the air speed is too high for the model to converge with accuracy. It does not necessarily mean that the required level of cooling is impossible to reach, but that it will cost more pump power to achieve. Finally, in the left column, two stars are shown. One near the center of each plot, marking the dimension chosen for the machine design in the coming chapter. And one star at the right edge of the plots, marking the dimensions for the conductor used in the experiments in the previous section.

Figure 4.12 shows the same layout as Figure 4.11, but with the inlet air speed in m/s presented. Figure 4.13 presents the inlet pressure in bar (where 1 bar is the outlet pressure). Figure 4.14 present the resistive losses divided by the pump power, thus showing the relation between the powers summed in the total power. Within each figure, the same color scale is used, so every shade represent the same range of values.

4.3.1 Analysis of the results

In Figure 4.11, a number of trends can be seen. For higher current densities, more power is lost to resistive losses and pump effect for the cooling system. Higher fill factor generally means less power lost. And for high current densities only the smallest windings can keep the insulation cool enough without exceeding the air speed limit.

In Figure 4.12, it turns out that the required air speed increases fast as the current density increases. For higher current densities, larger conductors and narrower air channels require higher speeds. For the narrower channels, this is because a higher speed is required to maintain more or less the same mass flow that the wider pipes let through. For larger conductors, the reason is mostly
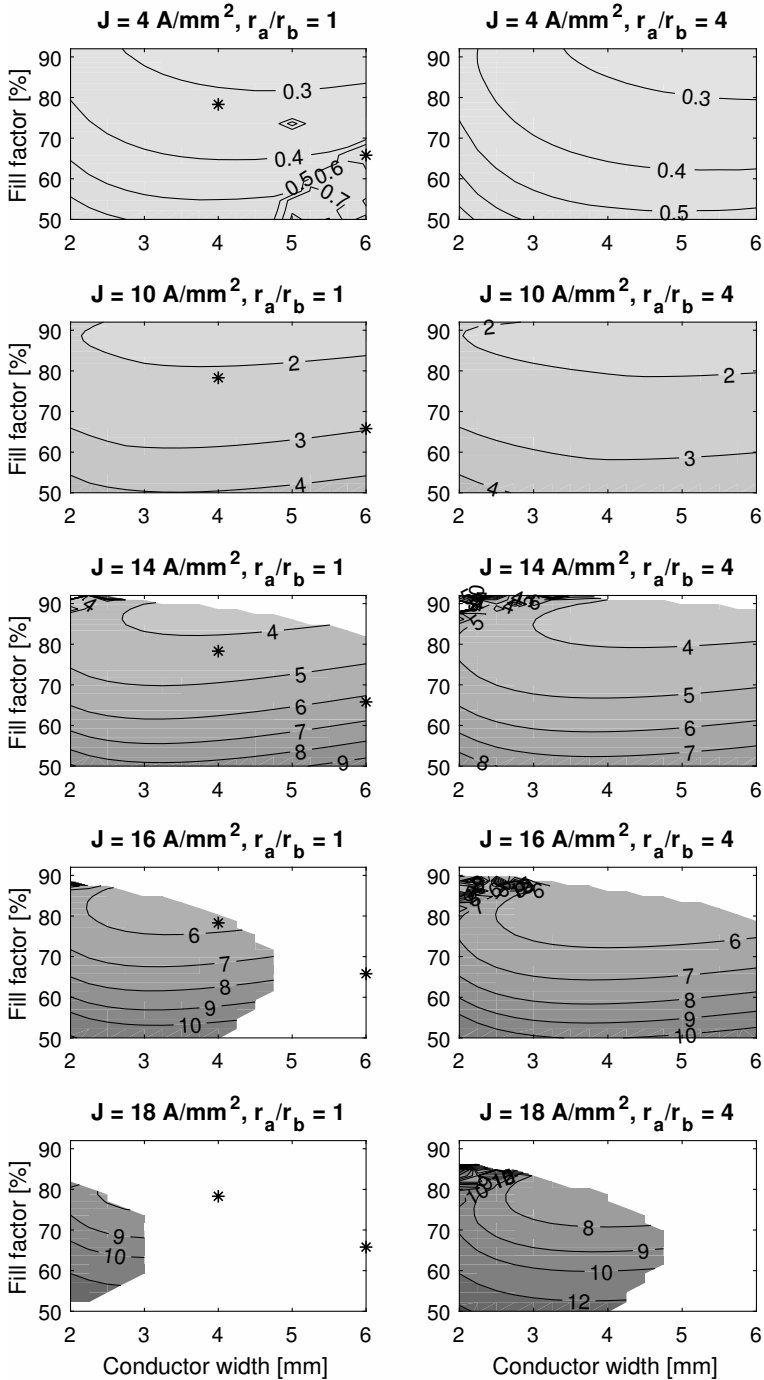
Figure 4.11: The total power [W/mm^2@$L = 224$ mm] (resistive losses and pump power) necessary to keep the copper below 150 $^\circ$C for various current densities, conductor dimensions and fill factors, for 224 mm long conductors.
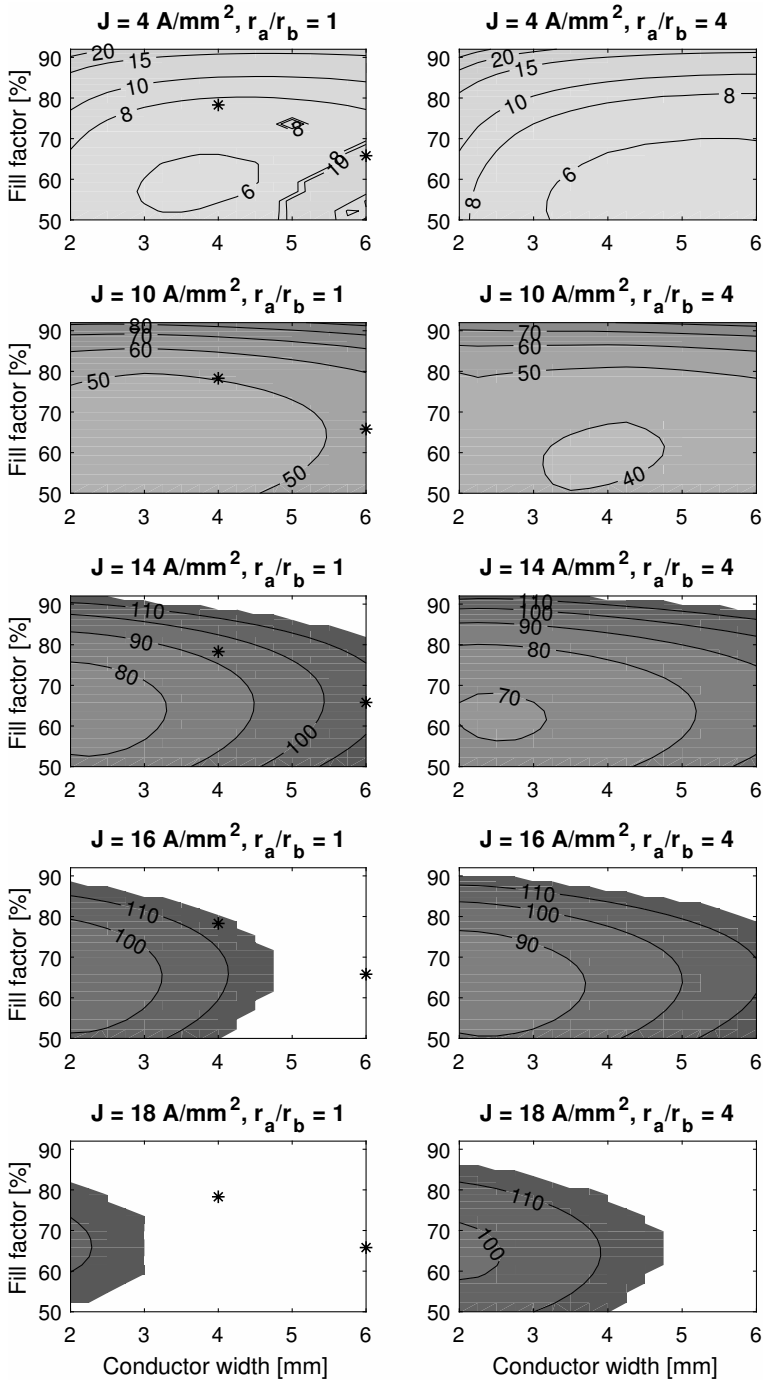
Figure 4.12: The air speeds that will keep the copper below 150 °C for various current densities, conductor dimensions and fill factors, for 224 mm long conductors.
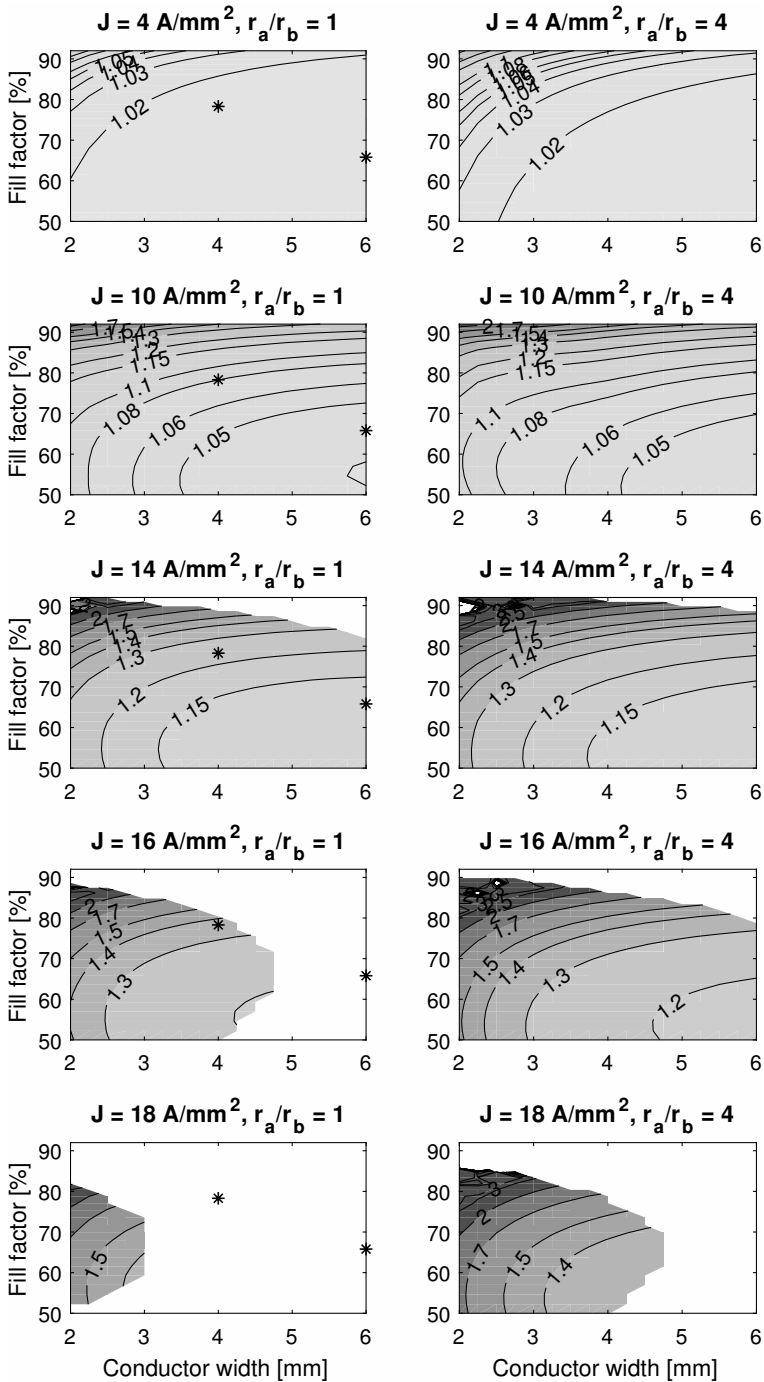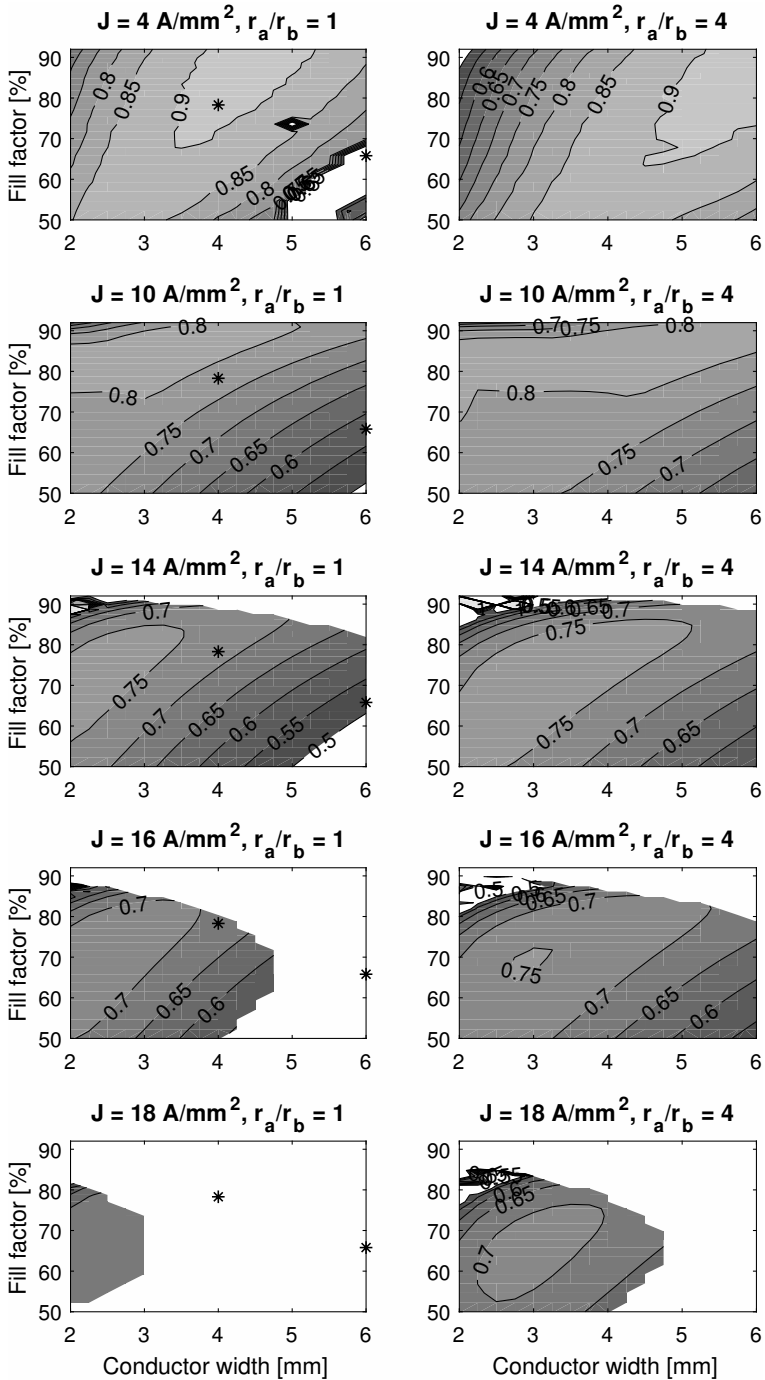
Figure 4.13: Inlet pressure necessary to produce the air speed needed to keep the copper below 150 °C for various current densities, conductor dimensions and fill factors, for 224 mm long conductors.

Figure 4.14: Resistive losses per pump power when copper is kept below 150 °C for various current densities, conductor dimensions and fill factors, for 224 mm long conductors.

that wider air channels have less surface area per volume flow, meaning the heat transfer in the surface is lower per mass flow, decreasing the heat dissipated into the air.

In Figure 4.13 it is quite expectedly seen that wider channels in larger conductors require lower inlet pressure. Comparing the pressure and air speed figures, it is noticed that for pressure, the circles have their center towards the lower right of the graphs, while the air speed has the circles' centers to the lower left. Since the pump power is the product of the pressure drop and the volume flow, it might be expected that the pump power should have the circles gathered around the lower part of the graphs. But the cross section areas have a high impact on the volume flow, which lifts the lowest pump powers to the higher fill factors.

The relations between the resistive losses and the pump powers shown in Figure 4.14 indicates no extreme relation, but make clear that the pump power is always higher than the resistive losses, but never more than twice.

Comparing the circular and elliptic channels, it turns out they are very similar in total power, but still there is a big difference in the ability to reach high current densities. The source of this difference is clear when comparing the pressure and air speed results for the channel shapes. The elliptic channels require a higher inlet pressure, because of the extra friction due to the extra surface area. But the extra surface area also increase the heat transfer in the surface, meaning less air needs to be pushed through. This expected difference in required air speeds can be seen in the results. And since the air speed is the most limiting parameter in the cooling model, this works to the advantage of the elliptic channel. Remember, however that this limitation is in the model and not in a real case. An improved model for higher speeds, or real life experiments are needed to explore this difference further, before a final decision can be made.

Which dimension that is most efficient depends on the operation point. For low current densities, high fill factor is good, since the need for cooling is low, making the extra conductor area more important than keeping the friction down for the air pressure. As the current density is increased, the area for lowest total power moves to lower fill factors. An optimal winding would more or less move from a large one with a very thin air channel, diagonally over the graph to a smaller conductor a higher portion used for the air channel, to be able to reach high current densities. For a certain application with a known distribution of operation points, a sound choice can be made. For a general application as the work of this thesis, with the purpose to compare the general performance of an electrically magnetized rotor with an interior permanent magnet rotor, some kind of golden mean has to be found.

The choice for the rotor performance study falls on a 4x4 mm conductor with 78 % fill factor, or in other words, a circular 1.05 mm radius air channel. The motivations follow.

In order to not forget the experiences from the laminated windings (chapter 3.3), the thinnest windings with the narrowest channels are avoided, to not be too optimistic about which paths the air flow will choose in a real application. For a low operation point, a large conductor with a narrow winding is desirable, but to enable high load, those are the worst choice. 4 mm, 78 % fill factor simply is basically halfway through and seems to be a good compromise. The fill factor is high enough to keep the total power down, but low enough to enable at least 16 A/mm^2 (before the model's convergence and accuracy problems commence). The elliptic channels are avoided because of the lack of testing and the uncertainty about the manufacturability they possess at this moment.

This concludes the air cooling modeling chapter, providing the tools and experience necessary into the design of the rotor for the performance comparison.

Chapter 5

Rotor design

This chapter covers the design of a rotor for an existing stator, with the purpose of comparing its performance with the original IPM rotor of the same machine, to evaluate the potential in the direct cooling concept.

The chapter starts with a presentation of the reference machine and its specifications, continues with some analysis to identify some important parameters prior to the rotor design itself. The rotor design integrates the cooling model featuring the previous chapter. The chapter ends with the aforementioned performance comparison to the IPM reference machine.

5.1   The reference machine

An IPMSM for a parallel hybrid drive in heavy vehicles is developed at the author's department at Lund University [82] [83]. This machine is tested and known well in both theory and practice. The specifications of the machine are presented in Table 5.1 and a section of the machine is shown in Figure 5.1.

5.2   Rotor geometries

For the design of the electrically excited rotor, some choices are made to simplify the optimization. Since the windings proposed require rectangular slots, the dimensions for the rotor geometry are limited to the height of the slot h_s, width
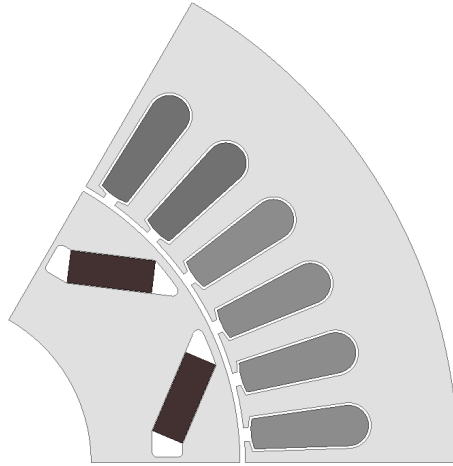
Figure 5.1: Section of the original IPM machine

Table 5.1: Reference machine specifications

Machine type	IPMSM	
Continuous power	80-110	kW
Peak power	150-180	kW
Peak torque	250	Nm
Top speed	15000	rpm
Active length	224	mm
Outer active stator radius	100	mm
Air-gap radius	60	mm
Air-gap width	1	mm
DC voltage range	600-650	V_{dc}
Max. cont. stator current	180	A_{RMS}
Coolant medium	Gearbox oil	
Poles	6	
Stator slots	36	
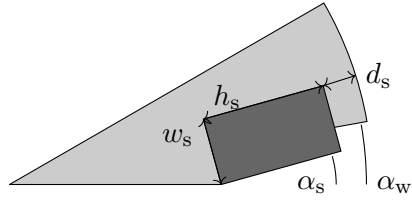
Figure 5.2: Dimensions in the rotor geometry, where light gray represents the iron core and dark gray represents the slot. The figure shows 1/12 of the the machine.
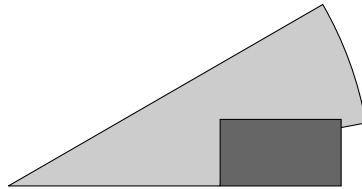
Figure 5.3: Geometry 1, with 0° slot angle.
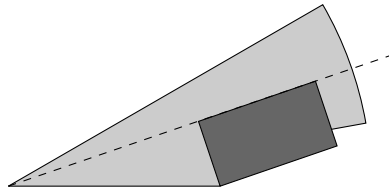
Figure 5.4: Geometry 2, with a slot angle resulting in the tangent of the slot/tooth interface intersecting the center, marked with the dashed line.
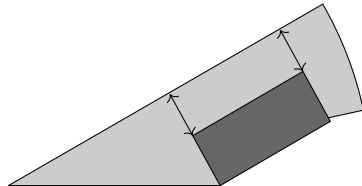
Figure 5.5: Geometry 3, with a slot angle resulting in constant tooth width, marked with the arrows of equal length.

of the slot w_s, the depth of the slot from the air-gap d_s, the angle of the slot α_s, and the angle of the wedge-gap α_w, illustrated in Figure 5.2.

The slot angle determines the three main geometries studied in the rotor design. The first geometry is defined by $\alpha_s = 0$, shown in Figure 5.3. The second geometry has a slot angle that results in the tangent of the slot/tooth interface to intersect the center of the machine, shown in Figure 5.4. The third geometry is defined by the slot angle that results in a constant tooth width, shown in Figure 5.5.

5.3   Loss studies

Before performing the rotor design, some studies on the losses of the machine are made.

5.3.1   Space harmonics losses in rotor windings

The rotor winding uses direct current to magnetize the rotor. When the rotor rotates in the stator, the flux will fluctuate as the stator and rotor teeth alignment varies. These flux variations, along with flux leakage through the windings, are called space harmonics and will induce an alternating current in the rotor windings.

If the space harmonics result in more than negligible extra losses in the rotor windings, the air cooling model must include the AC resistance in the rotor windings, and not only the DC resistance. To examine whether this is necessary, and how the winding dimensions affect the space harmonics, a series of simulations are carried out.

Simulation setup for space harmonics

ANSYS 18.2 Electronics [84] is used to carry out 2D simulations to study the questions raised above. In the simulations, a section (1/6) of the machine is modeled, with the indented rectangular windings. The inputs of the simulation series is presented in 5.2. Only the losses in the rotor windings are studied in this section. In appendix A, a clarification of the definitions of currents used in this thesis is presented.

Table 5.2: Simulation inputs for space harmonics loss studies.

No of cases	Parameter	Min		Max	Step size	Unit
3	Rotor geometry	1	:	3	1	-
1	w_s		:	13		mm
12	h_s		:	13		mm
5	Speed	3000	:	15000	3000	rpm
1	I_x		:	500		A
1	I_y		:	500		A
3	I_r	0	:	600	300	A
134	Rotor angle	0	:	60	$\sim$0.45	°
2	Rotor winding conductors	2x4	:	3x6		-

Two sizes of conductors are studied in the windings. One case where 2 by 4 conductors with the size 3x6 mm are stacked per slot, and one case where 3 by 6 conductors with the size 2x4 mm are stacked per slot. Interestingly, the numbers 2&4 and 3&6 appear in both cases, so to be clear the numbers from here on will always be referring to the number of conductors, and not their dimensions in millimeters. The 2 by 4 case thus has the largest conductors. The conductor cross section area is roughly 2.25 times larger than that of the 3 by 6 case.

The simulations are made on all three geometries respectively, with slot dimensions kept constant. In figures 5.6, examples of the three geometries are shown with 2 by 4 conductors as well as 3 by 6 conductors. Note that the stator in the simulations in this study (section 5.3.1) is not exactly the same but similar to that of the reference machine. This does not however impact the relevance of the analysis and conclusions of the study for the rest of the work.

5.3.2 Results from space harmonics loss simulations

The mean losses in the rotor windings for a 60 degree sweep for various speeds and winding configurations is put together and shown in Figures 5.7 to 5.9.

First, it is clear in all cases that there is a strong frequency dependency in the rotor winding losses.

Comparing the conductor sizes, the smaller conductors have larger low frequency losses, and larger high frequency losses in all cases.
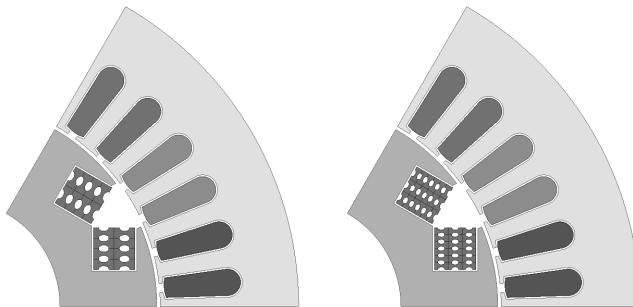
Comparing the geometries, geometry 1 and 2 are quite similar, while geometry 3 have significantly lower losses.
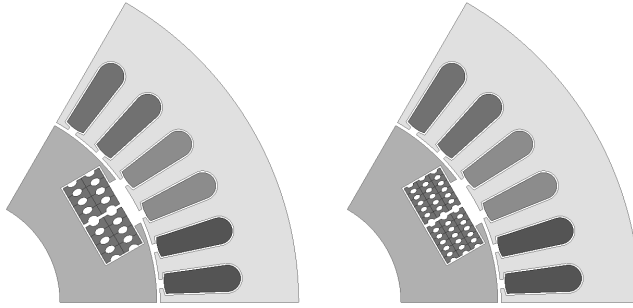
(a) Geometry 1, 2 by 4 con- (b) Geometry 1, 3 by 6 con-
ductors   ductors
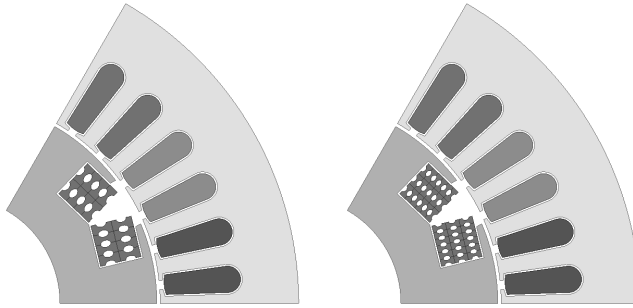
(c) Geometry 2, 2 by 4 con- (d) Geometry 2, 3 by 6 con-
ductors   ductors

(e) Geometry 3, 2 by 4 con- (f) Geometry 3, 3 by 6 con-
ductors   ductors

Figure 5.6: a-b) Geometry 1, constant slot width. c-d) Geometry 2, tooth angle origins in center.
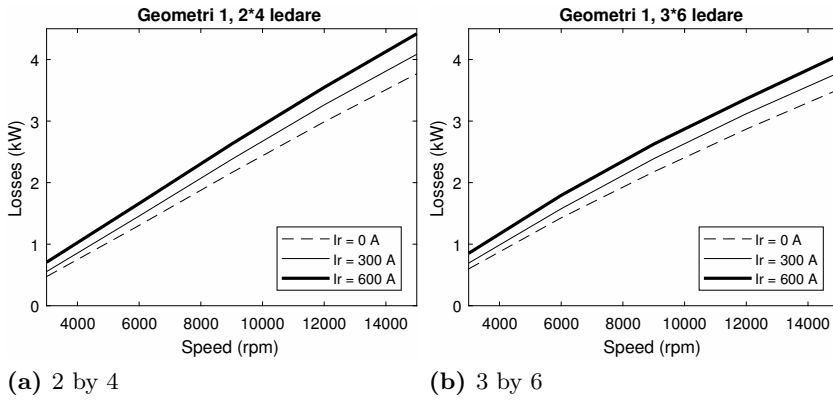e-f) Geometry 3, constant tooth width.

(a) 2 by 4

(b) 3 by 6

Figure 5.7: Rotor winding losses for Geometry 1.

(a) 2 by 4

(b) 3 by 6
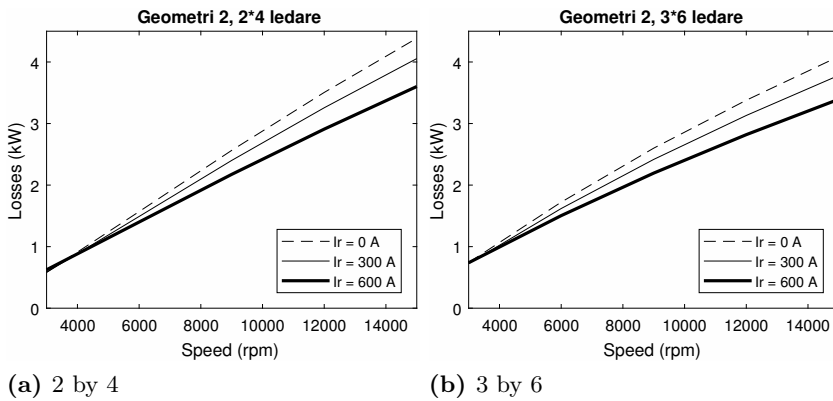
Figure 5.8: Rotor winding losses for Geometry 2.

(a) 2 by 4

(b) 3 by 6
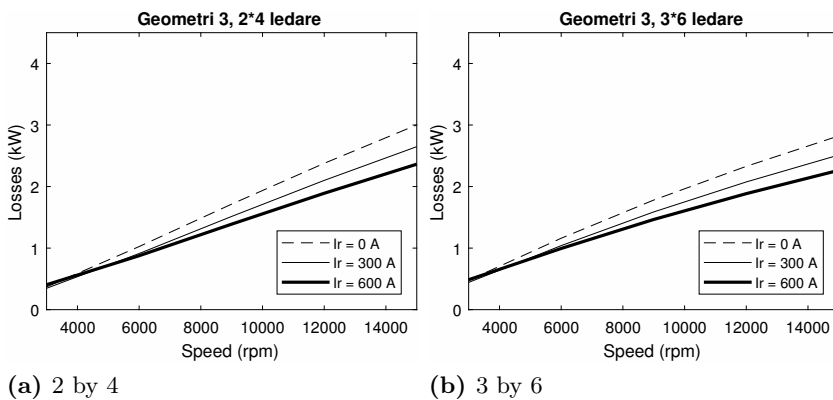
Figure 5.9: Rotor winding losses for Geometry 3.

Comparing the excitation currents I_r, the situation is more complex. As expected, it seems like the losses are smaller for lower excitation currents at low frequencies. At higher frequencies though, the result varies between the geometries. To address this, the flux variations are studied further below.

Flux linkage variations

As expected, figure 5.10 show that lower rotor currents result in lower rotor winding flux linkage. But the absolute magnitude of the flux is probably not as important to the space harmonics as the flux variations. Therefore, the min-max variations are compared in Figure 5.11.

The variations look similar for all speeds, so only 3000 rpm is shown. For geometry 1, the extent of the flux variations decreases as the excitations current increases, probably due to magnetic saturation. That however is not the case with geometries 2 and 3.

Analysis of space harmonics losses

The large impact of the frequency dependency of the losses makes clear that the AC resistance component can not be neglected when the air cooling model and electromagnetic simulations are integrated.

The size of the conductors has some effect on the magnitude of the losses, but a small one. As the conductor cross section area is reduced to 44 %, from 2 by 4 to 3 by 6 conductors, the losses decrease by less than 10 % in high frequencies and increase at low frequencies. This is likely contributed by a small inconsistency in current density, since the ration between copper and air channel area has a small difference in the simulations when the number of conductors is changed. This could affect the choice of rotor dimensions in the rotor design.

The geometries make a big difference on the space harmonics losses and makes it clear that this has to be kept in mind as the geometry of the rotor is determined. Further studies are needed on which other dimensions in the rotor design that affect the magnitude of the space harmonics. The rotor design can, in other words, not be set only with respect to the electromagnetic performance. A large contributor to the fact that geometry 3 seems best with respect to the rotor winding losses is the angle of the slots. The angle increase the distance and amount of iron between the rotor windings and the air gap, and results in the wedges covering more of the windings, making the flux less turbulent as the
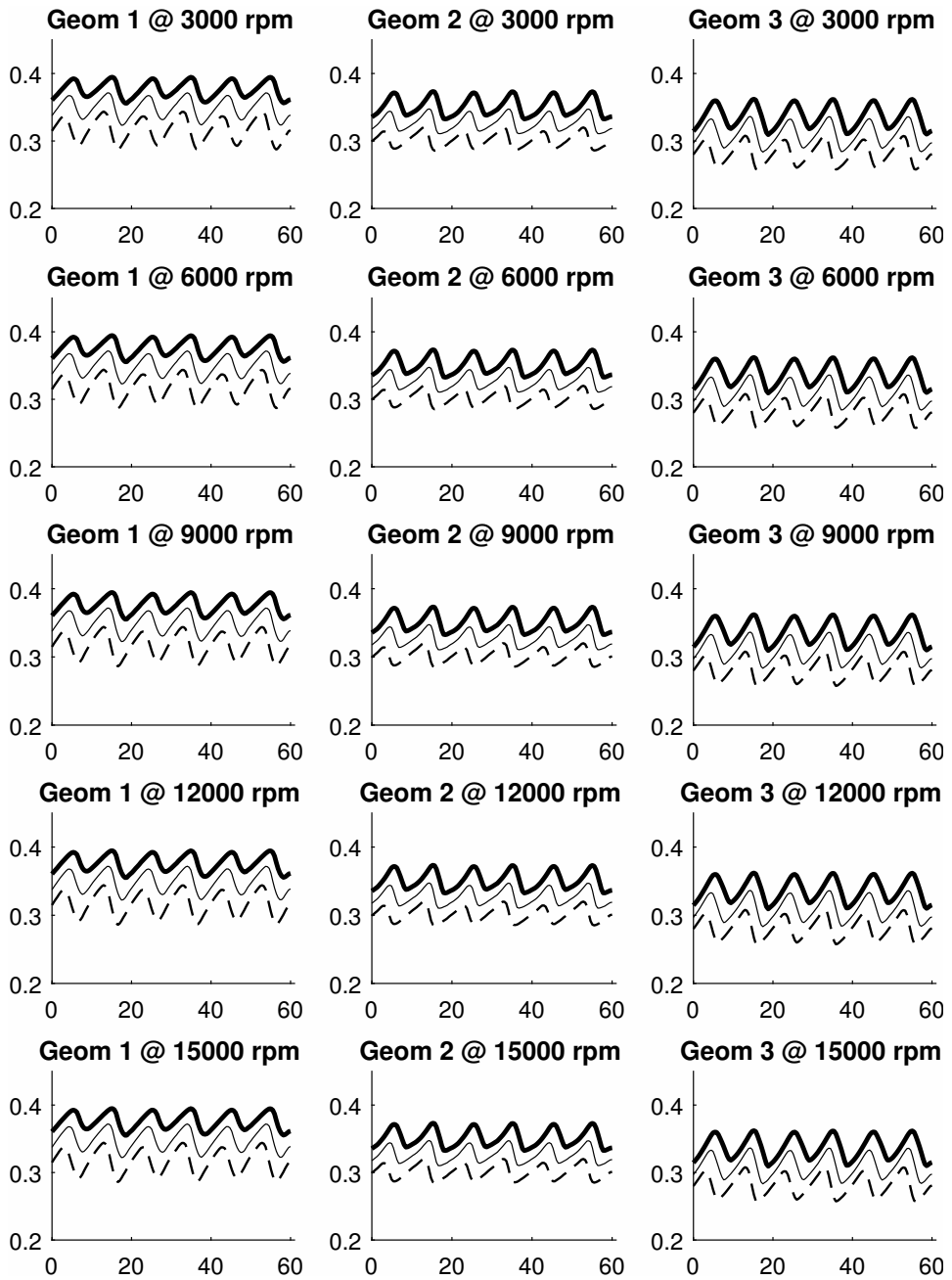
Figure 5.10: Rotor winding flux linkage [Wb] over a 60 degree rotor rotation. Dashed: $I_r = 0$ A, Line: $I_r = 300$ A, Thick: $I_r = 600$ A
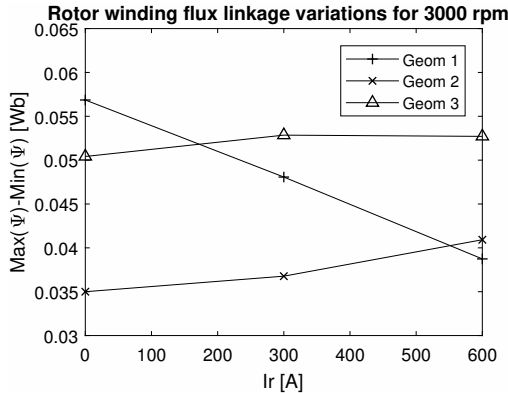
Figure 5.11: Min-max flux variations at 3000 rpm

rotor turns past the stator teeth. In other words, the poles in geometry 3 has more magnetic integrity, as the rotors were design in these simulations. This indicates the wedge gap can play a big role in the rotor design.

The most surprising result is that a larger excitation current does not always lead to higher losses. The look into the flux variations show that the min-max flux variations does indeed decrease as the iron becomes more saturated - but only for geometry 1, which is the only geometry where larger current always lead to bigger losses. By elimination, the cause for this phenomenon is blamed on the flux leakage through the slots. The simulations are run with a quite high stator current, so even at low excitation currents, the rotor flux originating from the stator current is high, resulting in high space harmonics losses even when the excitation current is low. The effect of the decreasing losses with increased rotor current is thus not so much an increased flux (As can be seen in figure 5.10, only a marginal increase), but an increase of the magnetic integrity of the rotor poles. As the excitation current is increased, less flux leaks through the windings to induce harmonic currents.

The conclusion from this study is that the AC harmonics has a strong effect on the rotor winding losses, but also that several elements in the rotor design have a big impact on the outcome.

5.3.3   Loss dependency on cooling channel dimensions

The air cooling model relies somewhat on the balance between the impact of the size of the cooling channel on the resistance and the pump power. If the channels

takes up a larger proportion of the slot area, the resistance will increase, leading to more losses. This will require more heat to be dissipated by the coolant air, but on the other hand, the coolant requires less pump power to be pushed through the larger channels.

However, the insight about the substantial effect the space harmonics has on the rotor winding losses, this problem becomes different, depending on what effect the size of the cooling channels has on the space harmonics losses. To bring clearness in that question a series of simulations are conducted.

Simulation setup and results for rotor winding loss dependency on cooling channel dimensions

The simulations are run in ANSYS 18.2 Electronics, on a model with the stator of the reference machine and the same rotor geometries as in the space harmonics study. The slot dimensions are 14x14 mm with 2 by 4 conductors in each slot. Each of the geometries are run with a speed of 3000 rpm and 12000 rpm respectively. The currents are set to $I_{x} = 500$ A, $I_{y} = 500$ A and $I_{r} = 600$ A for all cases. Every case is run twice - Once with plain rectangular windings, and once with indented windings for cooling channels.

The cooling channel indents used up $\sim 26\%$ of the cross section area of the conductors without indents, leading to an increase of the DC resistance with $\sim 35\%$. The simulations however showed that the losses in the rotor windings only increased with 0.5-5 %. This shows that the AC losses in the rotor windings are not directly dependent on the resistance.

A likely scenario is that when 26 % of the conductor cross section area is occupied with cooling channels, the conductor resistance increase by 35 %, and thus the DC losses in the increase by the same amount. The AC losses however is mainly originated from high currents induced at the fringe of the conductors and is not directly dependent in the conductor cross section area, and does thus not increase when the cooling channels are introduced.

An example of this would be a rectangular conductor where DC losses makes up 14 W and AC losses makes up 86 W (making a total of 100 W). 26 % of the conductor is taken away to give room for cooling channels, which makes the DC losses increase by 35 % to 19 W, but the AC losses maintain their 84 W of losses. This results in the losses increasing from 100 to 105 W, which is just 5 % even though the conductors DC resistance is increased by a larger amount.
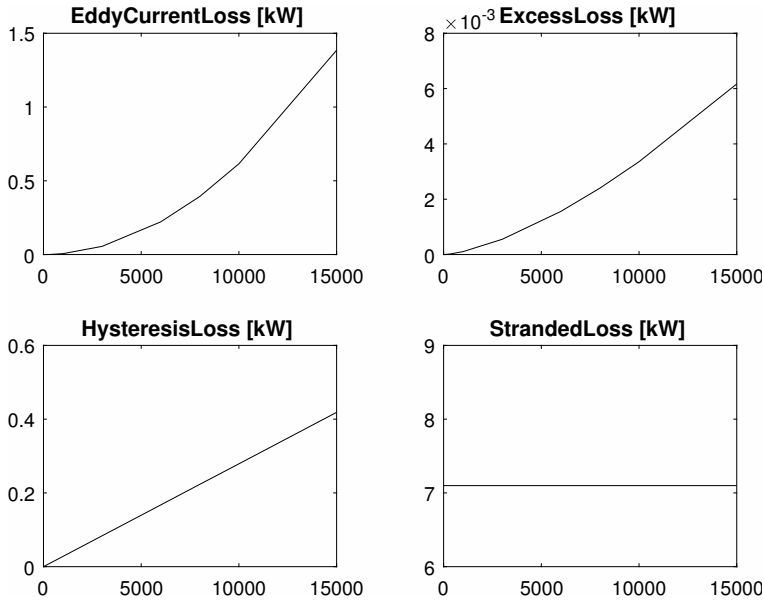
Figure 5.12: Summary of loss dependencies on speed

5.3.4   Loss dependency on speed

Simulations are conducted on various speeds in order to find out how the different types of losses provided from the ANSYS simulation results. The results are summarized in Figure 5.12.

The results show that ANSYS models the stator winding losses (shown as StrandedLoss) as independent of speed. The hysteresis losses are proportional to the speed. The Eddy current losses and (almost negligible) excess losses can be interpolated as second degree polynomials. The rotor winding losses (SolidLoss in ANSYS) have already been found to have a near linear speed dependency in section 5.3.1.

This means that the rotor design simulations only has to be run at two different speed for the losses of the other speeds to be derived, assuming the eddy and excess losses are both zero at 0 rpm.

Table 5.3: Simulation inputs.

No of cases	Parameter	Min	:	Max	Step size	Unit
3	Rotor geometry	1	:	3	1	-
2	w_s	8	:	14		mm
2	h_s	8	:	14		mm
2	Speed	3000	:	12000		rpm
5	I_x	-200	:	600	200	A
4	I_y	0	:	600	200	A
4	I_r	0	:	900	300	A
301	Rotor angle	0	:	120.8	~0.4	°

5.4 Rotor design optimization

The aim with the rotor design is to make one efficiency map of the machine for every simulated rotor geometry. The efficiency maps are based on an *Most torque per loss* algorithm (MTPL), resulting in a lookup table for each speed and torque. The efficiency maps are then compared to motivate the next iteration of simulations.

5.4.1 Simulation setup

The inputs of the first parameter sweep simulation of the rotor design are shown in Table 5.3.

The three rotor geometries are presented in the earlier sections of this chapters. The slot height and width are tested with two values each to give a direction of further iterations of slot simulations, as shown in figures 5.13-5.14. The speed is run at two different speeds, corresponding to half and double base speed, so that the frequency dependent losses can be interpolated according to the correlations determined in section 5.3.4. The stator currents are chosen so that they cover the current range of the original IPMSM, and provide some level of resolution. Note that the IPMSM operates solely in the second current quadrant when running as a motor because of the negative reluctance ($L_{mx} < L_{my}$), while the EMSM is expected to operate mainly in the first current quadrant because of the positive reluctance ($L_{mx} > L_{my}$). The excitation current covers excitation up until the flux in the core is just starting to saturate. Increasing the excitation after this point will continue to improve the performance, but to a lower degree. For the final performance comparison a higher excitation is used, but for this initial parameter sweep the simulation time is prioritized to cover a wider range
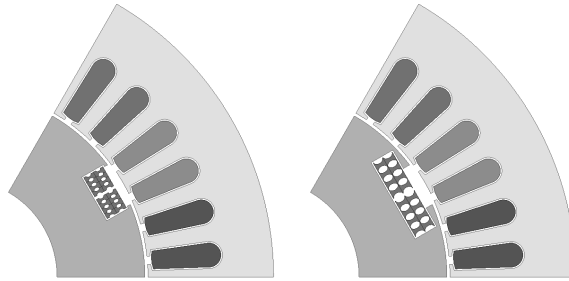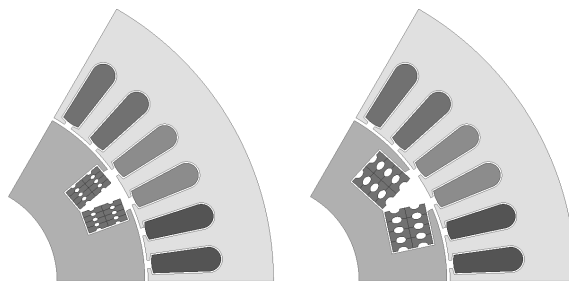
(a) Geometry 1, 8x8 mm   **(b)** Geometry 1, 14x8 mm
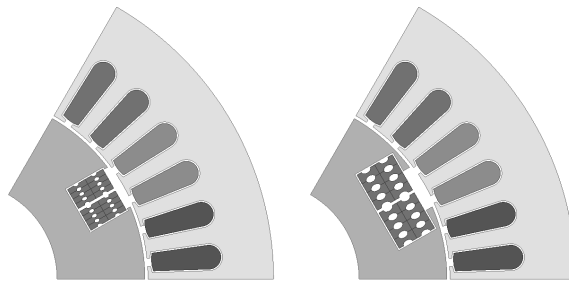
(c) Geometry 1, 8x14 mm   **(d)** Geometry 1, 14x14 mm
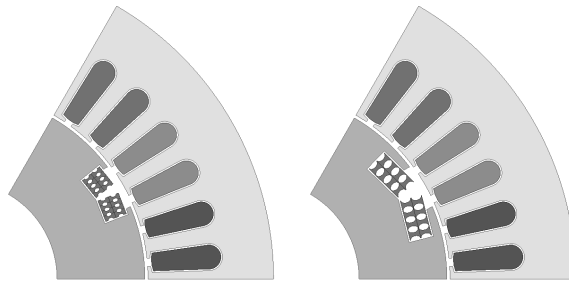
(e) Geometry 2, 8x8 mm   **(f)** Geometry 2, 14x8 mm

(g) Geometry 2, 8x14 mm   **(h)** Geometry 2, 14x14 mm

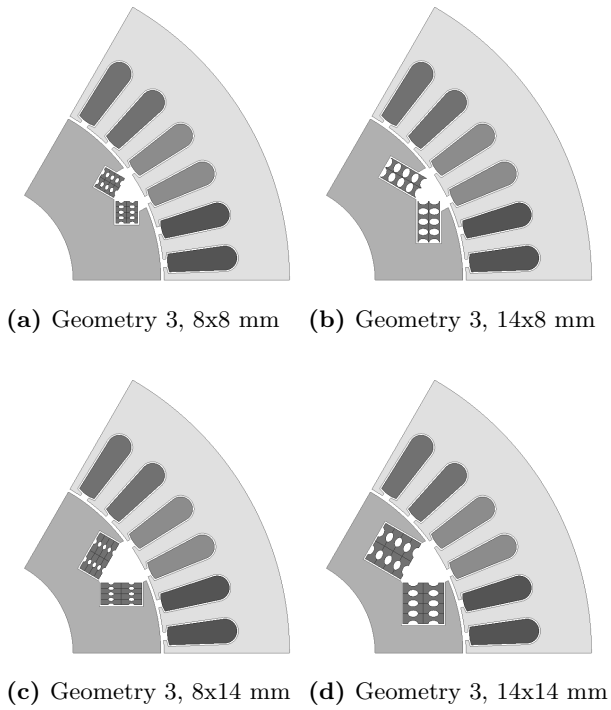**Figure 5.13:** Variations of geometry 1 and 2 with rotor slot dimensions given as w_s x h_s.

(a) Geometry 3, 8x8 mm **(b)** Geometry 3, 14x8 mm

(c) Geometry 3, 8x14 mm **(d)** Geometry 3, 14x14 mm

Figure 5.14: Variations of geometry 3 with rotor slot dimensions given as w_s x h_s, width x height. This sorting order of rotor design dimensions are used for all figures in the coming sections where results for several designs are shown.
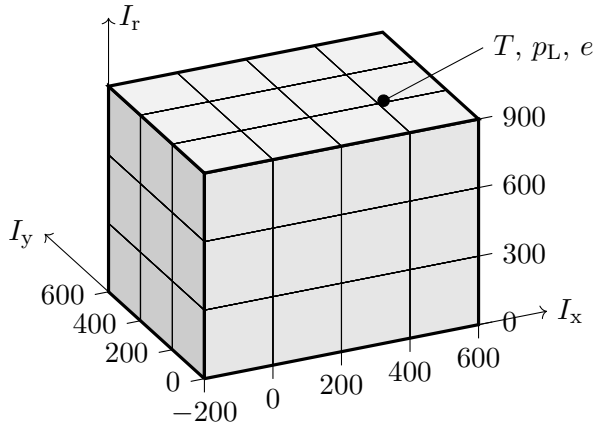
Figure 5.15: Example of a cuboid representing the three dimensional matrix with simulation results.

for more parameters.

These 1920 parameter combinations are each run for a rotor rotation of 120.8 degrees. The reason for this angle is that the hysteresis losses in the machine need 100.8 degrees to develop fully. The remaining 20 degrees of rotation are enough to deliver a whole period of loss characteristics, which repeats equally for for each stator phase (two stator slots) the rotor passes. The step size is kept as long as possible to still give full accuracy in the loss output from the simulation.

Post-processing cuboids

From the simulations, torque and all loss output from the software is obtained. The torque is averaged over the whole 120.8° rotation of the rotor, while the losses are averaged over the last 20°. The torque and different losses (hysteresis, eddy, stator windings copper losses and rotor windings copper losses) for each case is saved in a three dimensional matrix. The matrix can be represented as a cuboid with one current for each dimension of the shape and one value for the torque and every sort of loss in every node, as in Figure 5.15. Every speed, slot dimension and rotor geometry has one cuboid of its own.

The cuboid is then interpolated, so the resolution of the torque and loss values is increased from 5x4x4 to a higher value, like 41x31x31, so that there is one node for every 20 A in all dimensions, as in Figure 5.16. Cubic spline interpolation is used for the torque and the different losses.
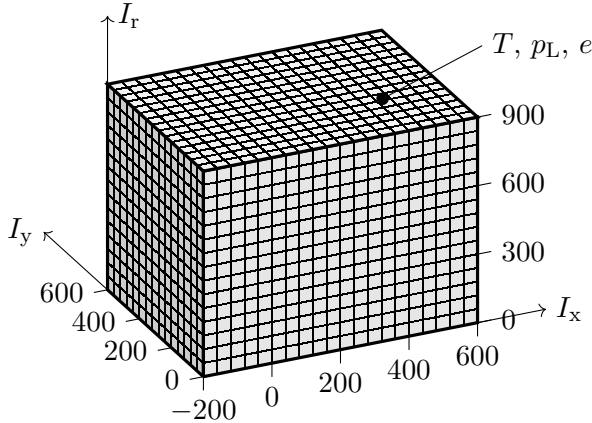
Figure 5.16: Example of interpolated cuboid with increased resolution.

Loss determination and interpolation

As stated before there is one of these cuboids for every different rotor geometry (1, 2, 3), slot dimension (width and height) and speed (3000 and 12000 rpm). The next step is to make new cubes for more speeds. As also stated before, the copper losses can be interpolated linearly, while eddy current losses (and excess losses) can be interpolated with second degree polynomials. Also the torque is interpolated linearly. All this is done for every node, to create a corresponding node in every cuboid for a new speed (below, between and above 3000 and 12000 rpm).

To get the necessary pump power to cool the total losses of the rotor windings (with both AC and DC losses), the air cooling model is used. In addition to what is presented in chapter 4, the model calculates the expected DC resistance and DC losses at normal temperature and subtracts the expected DC losses from the total rotor winding losses. As the air cooling model progresses, the DC resistance changes with every iteration of the copper temperature, increasing the DC losses. The AC losses are induced from a voltage, and as the copper temperature rises, the resistance increase, leading in theory to decreased AC losses. This AC loss decrease is not modeled, but at least it motivates why they are not included in the DC losses' increase with the temperature. The DC and AC losses determine the heat generation in the copper, and the golden section algorithm finds the air speed necessary to dissipate that heat (as described in chapter 4.1.3). The pump power for those conditions are saved in a lookup-table, to save processing time. The lookup-table gives the necessary pump power for any desired current and total rotor loss combination (Figure 5.17). Some cases
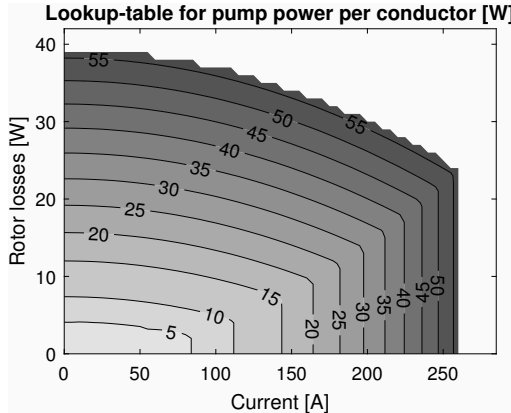
Figure 5.17: Representation of the lookup-table for the pump power.

result in the air cooling model not converging, like when an air speed of 120 m/s is not enough to dissipate all the heat. In this case, the model outputs infinite pump power. The rotor winding losses for every node is run against a lookup-table for the pump power.

The air cooling model assumes 4x4 mm conductors with 1.05 mm radius air channels, even though not an whole number of 4x4 mm windings fit in the slot dimensions simulated. The air cooling model scales the losses from the machine to losses per $mm^2@L = 224$ mm, and then scales the pump power back up to the cross section area of the rotor slots. In a real application, conductor dimensions fitting the rotor slots would of course have to be chosen.

Iso-torque surfaces and MTPL

The next step is to identify which current combinations in each cuboid that results in a certain torque. A number of different torque levels are set, and for each level, an iso-torque surface is derived, in every cuboid. For every current combination on the surface, the desired torque is put out from the machine. But not all of these current combinations are available, for different reasons. So for every node, on the iso-torque surface, unavailable currents have to be cut.

Current combinations where the air cooling does not converge are cut. Currents that exceed the maximum stator current, set by the converter and/or thermal constraints in the machine, are cut as well. This maximum stator current is inherited from the original IPMSM. Optimally, the currents made unavailable due to voltage limitations and the induced voltage, are cut too. For the initial

parameter sweep, this is not done. But for the other iterations of simulations the induced voltage is known for every node in the cuboids, as the length of the average of the power invariant d, q-transformation of the induced voltage, which is then interpolated for higher current and speed resolution like the other parameters.

The interpolation of the induced voltage takes a bit of extra care, though. The magnitude of the induced voltage will be highly dependent on the location of the current modulus resulting in zero voltage. The position of this modulus will depend on the rotor magnetization, starting at $i_x = i_y = 0$ A when $i_r = 0$ A and then moving to negative x-currents as the magnetization is increased. The position can be derived from the machine's voltage equations, if the necessary parameters are known 5.1 and 5.2.

$$u_{sx} = R_s i_x + L_{sx} \frac{di_x}{dt} + \omega_r L_{sy} i_y \tag{5.1}$$

$$u_{sy} = R_s i_y + L_{sy} \frac{di_y}{dt} + \omega_r (L_r i_r + L_{sx} i_x) \tag{5.2}$$

If they are not, the zero voltage modulus is harder to locate, especially with the sparse resolution of currents simulated. Two example of this is shown in figure 5.18, where the induced voltage is derived with cubic interpolation over the simulated current grid in the left column. The figure shows the iso-torque lines for 40, 70 and 100 Nm, as well as the iso-induced voltage lines for 425, 600 and 800 V for a few different rotor currents at 10 000 rpm. Since the inverter voltage supply is limited to 600 V for the reference machine, the voltage available for the stator windings is $600/\sqrt{2} \simeq 425$ V. In the left column of the figure, a torque of 40 Nm is available for a few current combinations, where the 40 Nm iso-torque line is below the 425 V iso-voltage line, for the low rotor current ($I_r = 500$ A). For the following two rotor currents, the 425 V iso-voltage line all but disappears completely, to grow back at the highest rotor current shown. This behavior makes 40 Nm unavailable for rotor currents between 500 and 1500. The problem is that there is no indication that the voltage should be zero at some point between $I_x = 0$ and $I_x = -200$ A, when there are no simulation results. The values of the induced voltage between $I_x = 0$ and $I_x = -200$ A will thus be interpolated between the values of the induced voltage at $I_x = 0$ and $I_x = -200$ A. The result is the low voltages disappear.

To solve this, the induced voltage vectors are studied for $I_x = 0$ and $I_x = -200$ A along the x-axis. The assumption that the voltage increase linearly is made,
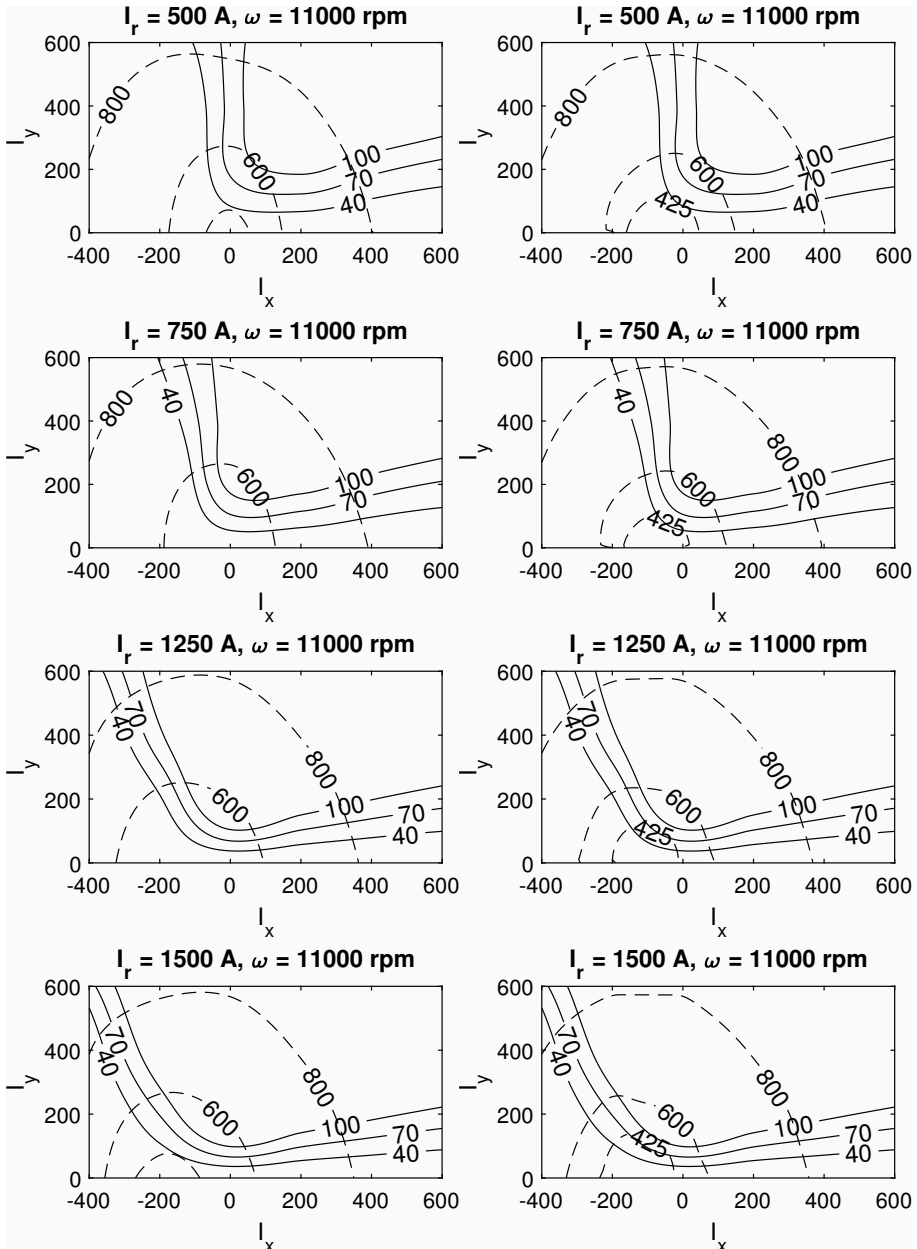
Figure 5.18: Induced voltage (dashed) and torque for various rotor currents at 10 000 rpm, for two interpolation methods. Left: Cubic interpolation over simulated current grid. Right: Natural neighbor interpolation including approximated zero voltage modulus. The examples are from different torques and speeds of the final EMSM design.
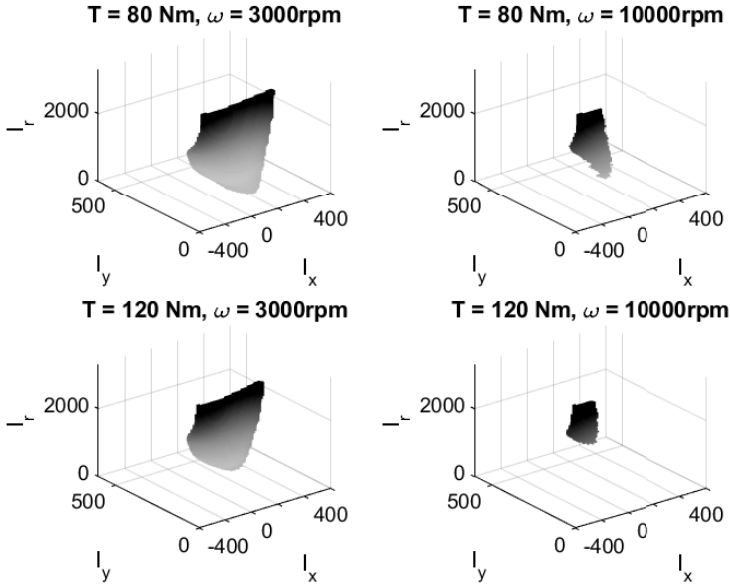
Figure 5.19: Examples of three dimensional iso-T planes with losses represented in the shade on the plane. Brighter color means lower losses. The examples are from different torques and speeds of the final EMSM design.

so that the length of the induced voltage vectors at the mentioned currents, can be used to calculate *if* and in that case *where* between $I_x = 0$ and $I_x = -200$ A the voltage is zero. When this modulus is identified, the induced voltage cuboid can be interpolated (using the *natural neighbor* method), including the zero voltage modulus, resulting in the right column of figure 5.18, where the 425 V iso-voltage line is similar for all rotor currents, as it moves towards the left.

As the current limitation, voltage limitation and cooling limitation have cut off their chunks of current combinations, hopefully there is still a bit of the iso-torque surface left. If so, the point on the surface with the lowest total losses is identified and the current combination for that point is saved in a lookup table as the current that gives most torque per losses (MTPL). A few examples of iso-torque surfaces, with total losses represented in a gray scale on the surface, are presented in Figure 5.19.
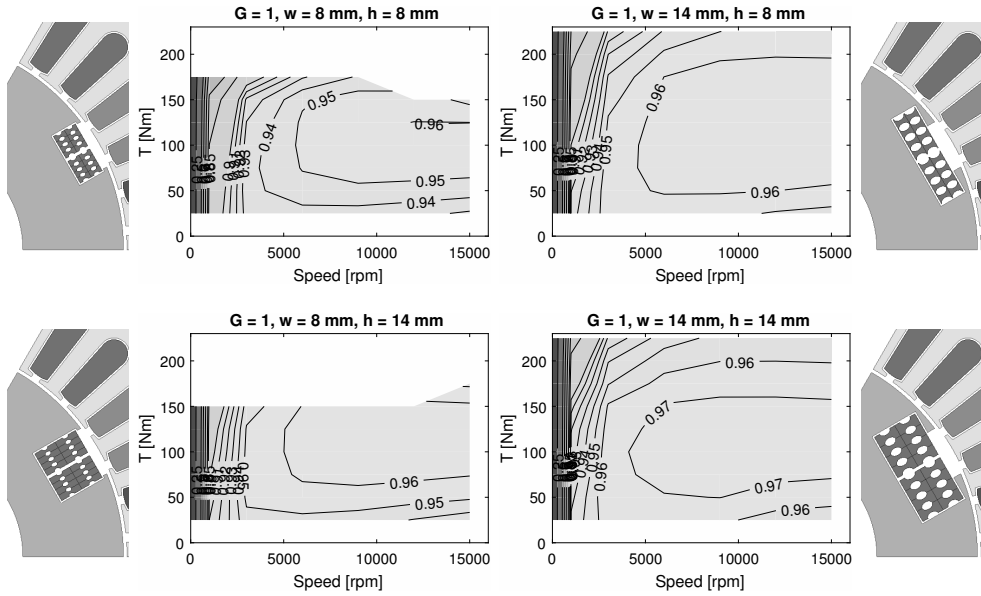
Figure 5.20: Efficiency maps for the first iteration of slot dimensions for Geometry 1.

Torque-speed characteristics and efficiency maps

As the current combination giving the lowest losses is known for every torque and speed, for every rotor geometry and slot dimension, efficiency maps can be put together. The (mechanical) power p_m for every point in the efficiency map is calculated as the product of speed and torque, and the efficiency is calculated as equation 5.4.1.

$$\eta = \frac{p_\text{m}}{p_\text{m} + p_\text{L,tot}} \tag{5.3}$$

The efficiency maps from the first series of simulations are presented in figures 5.20-5.22. The results are discussed in a later section, but a few things are clear from the results. The larger slot dimensions are better (with regards to efficiency and torque capability for the limited rotor current) for all geometries. This motivates the dimensions of the second parameter sweep to be made at some combinations of 11, 14 and 17 mm for slot widths and heights. For these simulations, the induced voltage in the stator is recorded, to limit the power and see the speed range capacity. For both series of simulations, the stator current is
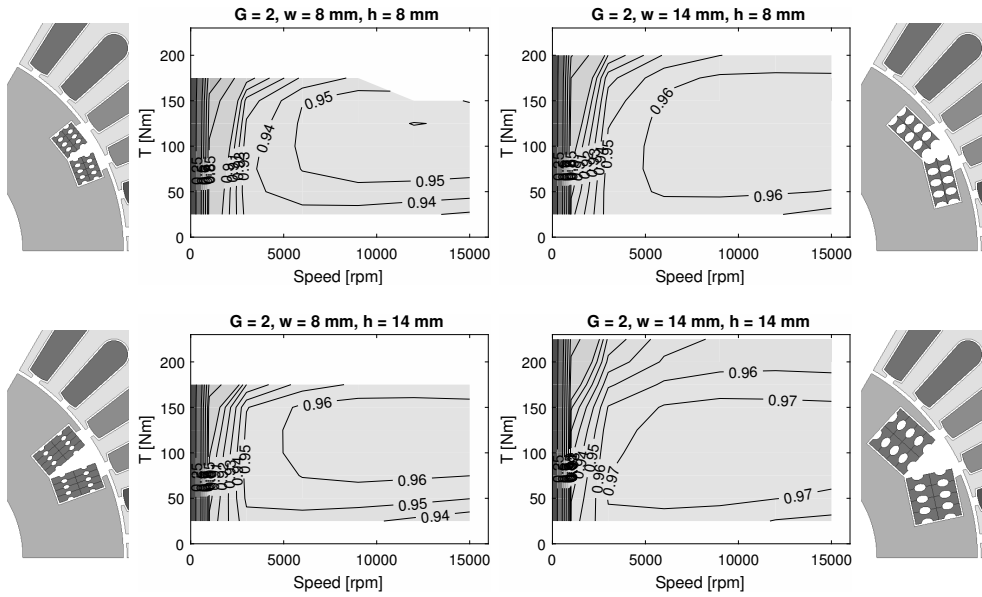
Figure 5.21: Efficiency maps for the first iteration of slot dimensions for Geometry 2.
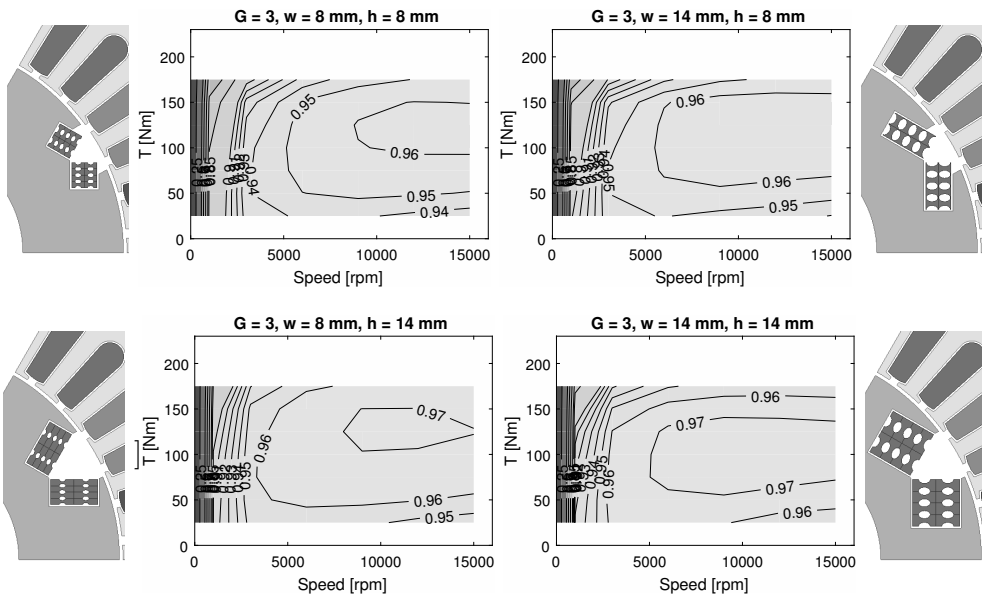

Figure 5.22: Efficiency maps for the first iteration of slot dimensions for Geometry 3.
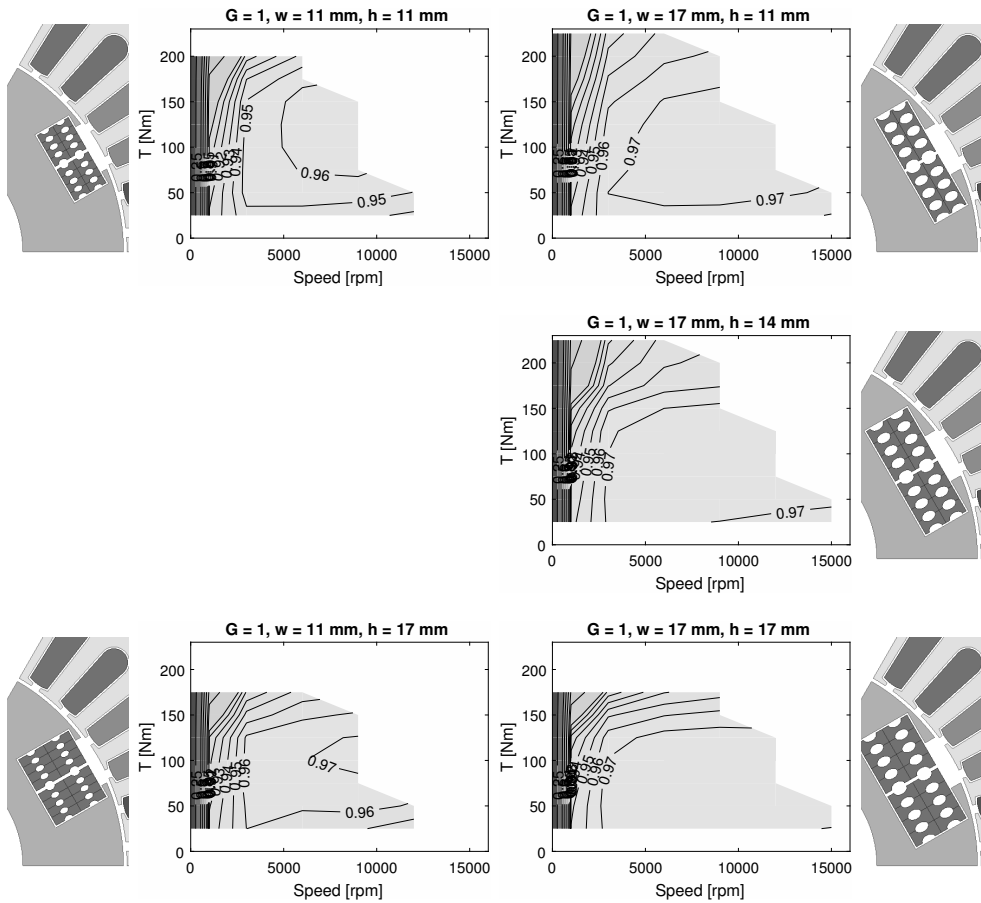
Figure 5.23: Efficiency maps for the second iteration of slot dimensions for Geometry 1.

limited to $|I_x + I_y| \leq 500$ A, the converter voltage to 900 V and the rotor current to converging air cooling, with the help of the aforementioned lookup-table. The results of the second series of simulations are shown in figures 5.23-5.24.
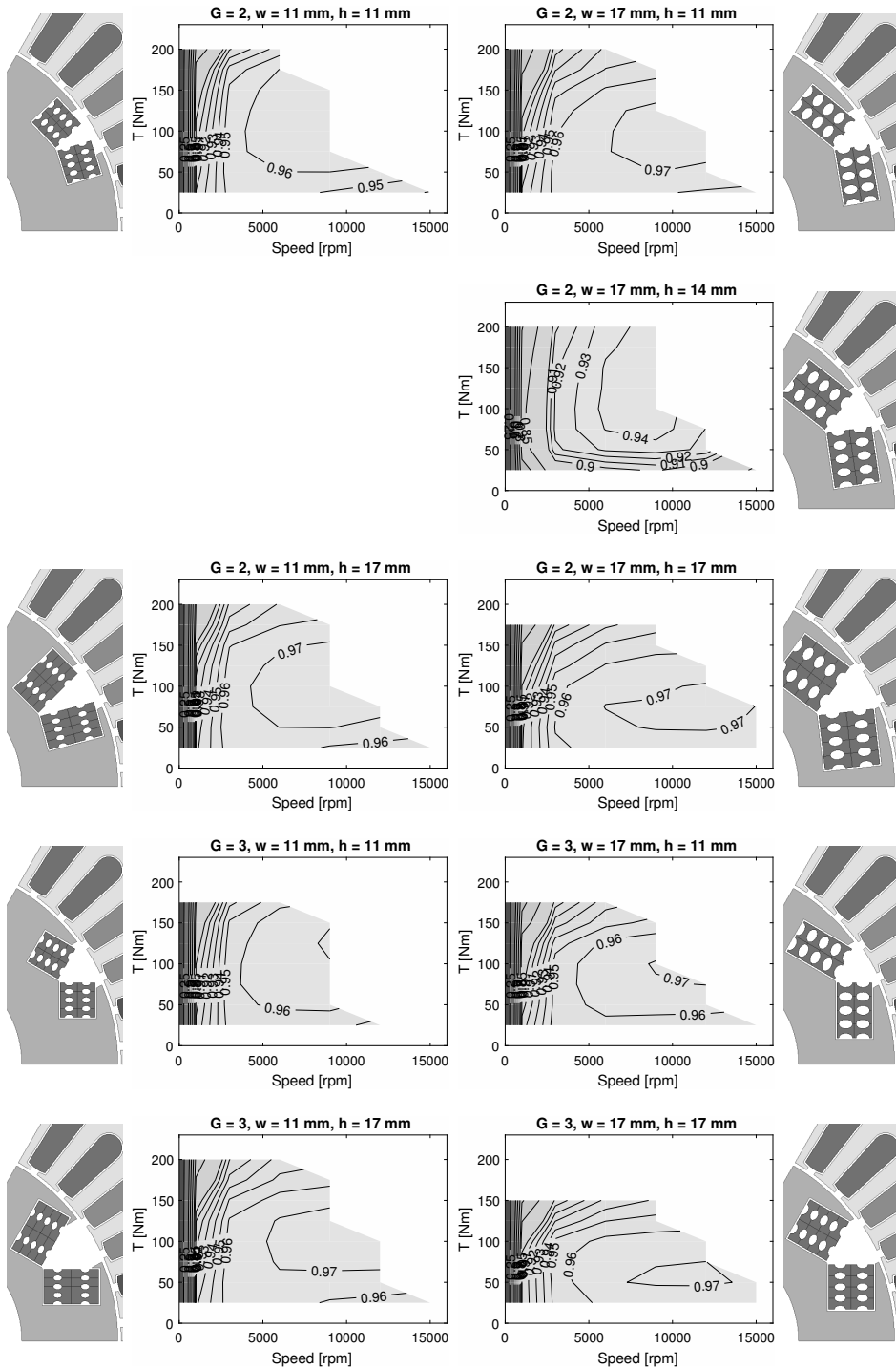
Figure 5.24: Efficiency maps for the second iteration of slot dimensions for Geometries 2 and 3.
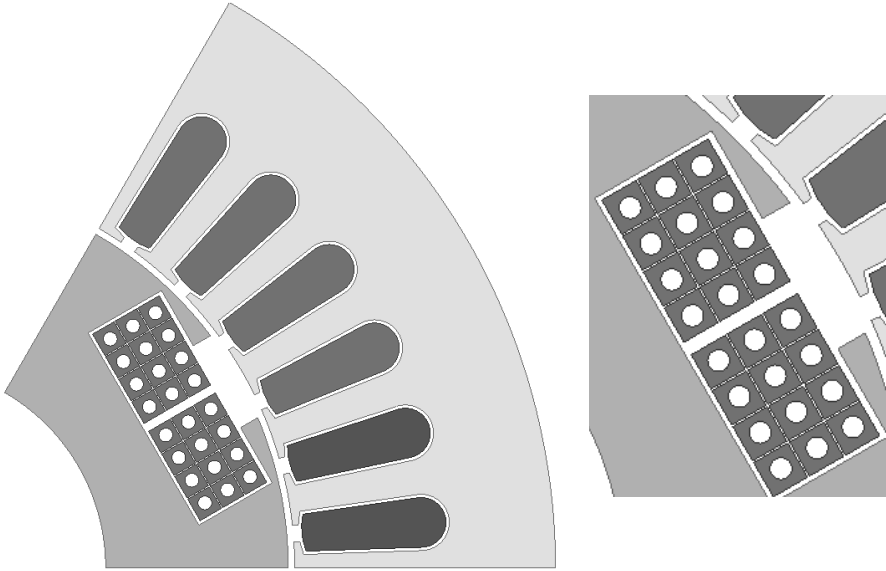
Figure 5.25: The machine used for the simulations of the performance comparison, with a close-up of the rotor windings.

5.5   Performance comparison

One final simulation is run with a slot width of 17 mm and height of 13 mm, with hollow windings with the same dimensions as the winding dimensions chosen in chapter 4.3.1, shown in figure 5.25. The simulation inputs are presented in table 5.4.

Table 5.4: Simulation inputs for final EMSM design.

No of cases	Parameter	Min	:	Max	Step size	Unit
1	Rotor geometry		:	1		-
1	w_s		:	17		mm
1	h_s		:	13		mm
2	Speed	3000	:	12000		rpm
6	I_x	-400	:	600	200	A
4	I_y	0	:	600	200	A
12	I_r	0	:	3300	300	A
301	Rotor angle	0	:	120.8	$\sim$0.4	°

The resulting efficiency maps are shown in 5.26. As limitations in the post-
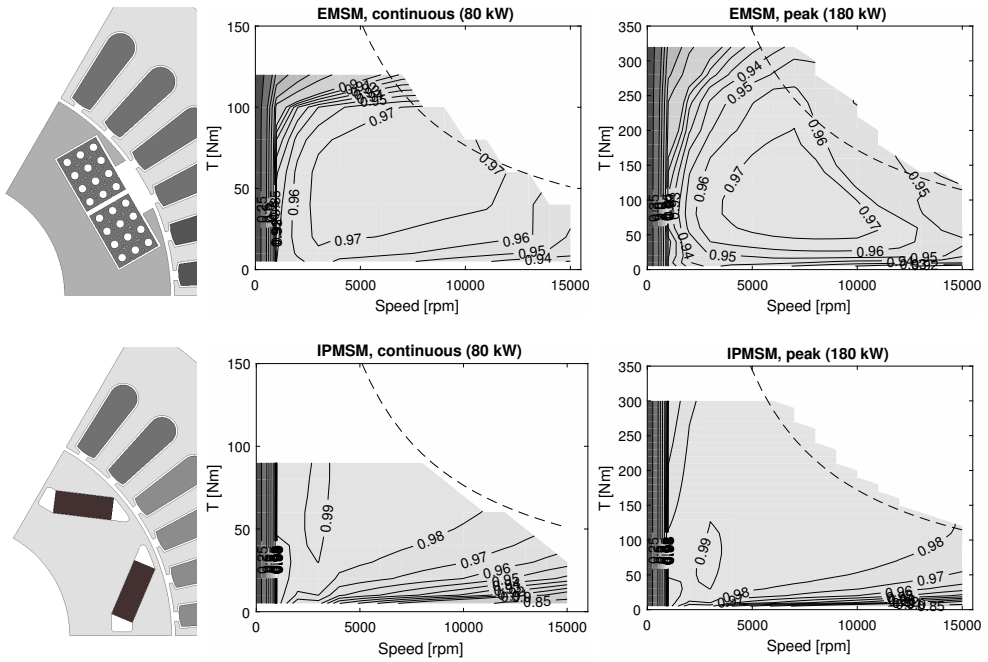
Figure 5.26: Efficiency maps for the chosen air-cooled EMSM and the reference IPMSM for continuous and peak power. The dashed lines mark 80 kW for continuous power and 180 kW for peak power respectively.

processing of this design, the converter voltage is set to 600 V, while the rotor current is simulated up to 3300 A per slot and is then limited by the cooling capability. The stator current is limited at two levels, one for continuous power with $|i_x + i_y| \leq 180$ A, corresponding to $|I_x + I_y| \leq 104$ A, and one for peak power with $|i_x + i_y| \leq 519$ A, corresponding to $|I_x + I_y| \leq 300$ A.

The machine with the air cooled electrically excited rotor reaches the original requirements of the reference machine with the same voltage supply and continuous thermal limitations to the stator current, which are repeated here for pure convenience, table 5.5.

The efficiency is lower than that of the IPMSM, which is expected and in the author's eyes, but the difference is smaller than expected. But when it comes to torque, power and speed capability, the EMSM shows clear signs of being able to outperform the IPMSM.

Table 5.5: Requirements for the reference machine

Continuous power	80	kW
Peak power	180	kW
Peak torque	250	Nm
Top speed	15000	rpm
Active length	224	mm
Outer active stator radius	100	mm
DC voltage range	600-650	V_{dc}
Max. cont. stator current	180	A
Max. peak stator current	519	A
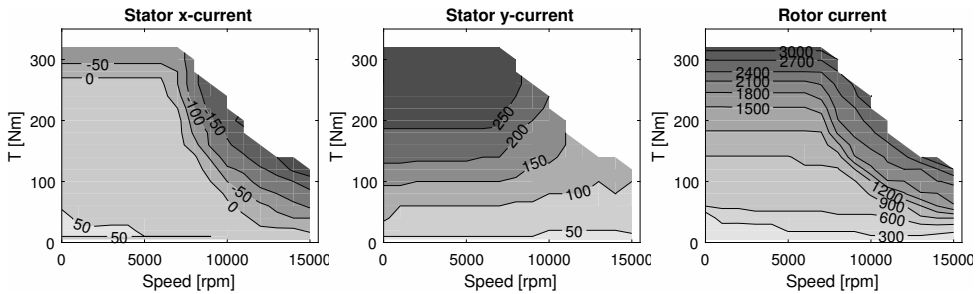
Figure 5.27: The current combinations derived from the MTPL algorithm for the peak power case of the EMSM.

5.5.1   Analysis of EMSM operation

An analysis of the currents in the EMSM is made with the help of figure 5.27. The stator x-current is positive and low ($0 < I_x < 50$ A) for most of the map, with a couple of interesting exceptions.

The first interesting area is high torque (> 270 Nm) at low speed (< 6000 rpm). The area is explored in figure 5.28, left column. Iso-torque lines for 250, 270, 300 and 320 Nm are shown together with a dashed half circle marking the maximum peak stator current and a line marking $I_x = 0$ A. In the top left diagram, for $I_r = 1850$ A, the point where the 250 Nm iso-torque line touches the maximum stator current line marks the MTPL-modulus for 250 Nm, and for this point, I_x is still positive. At $I_r = 2190$ A, 270 Nm touches the maximum stator current line at exactly $I_x = 0$ A. Above this torque level, the MTPL is reached for negative stator x-currents. This marks an important property of the EMSM with direct cooled rotor windings. High rotor currents push the iso-torque lines down to the left, turning the operation over to the second quadrant for high powers. This overload capability in the rotor windings is also what is enabling
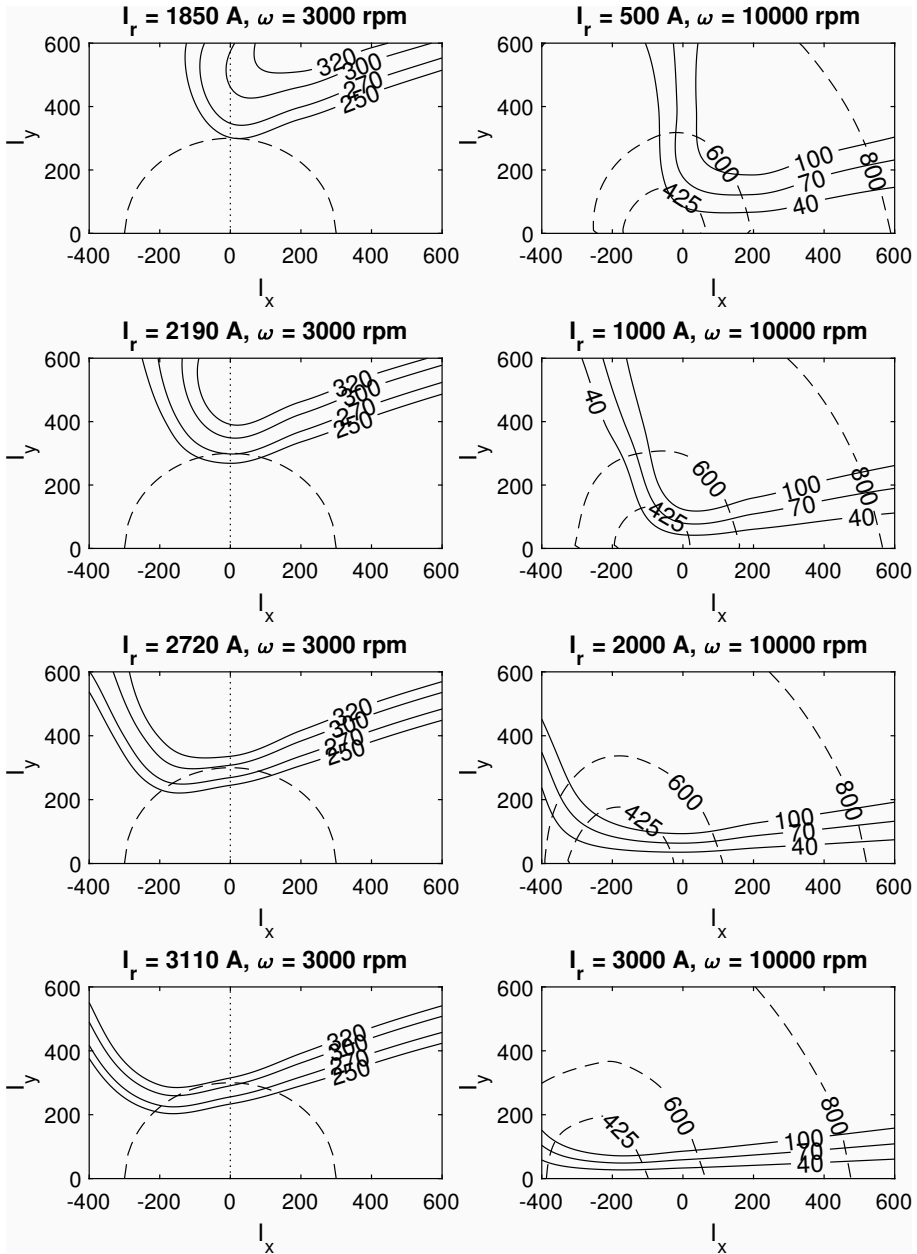
Figure 5.28: Left: Iso-torque lines for various rotor currents at 3000 rpm, with maximum stator current (dashed) and $I_x = 0$ A (dotted). Right: Iso-torque and iso-voltage (dashed) lines for various rotor currents at 10 000 rpm.

torques over 100 Nm continuously for the EMSM.

The second interesting area is the field weakening method in the constant power speed range (> 6000 rpm). It is clear that both the rotor current and stator x-current is used for field weakening, which is expected, since literature states this provides the optimal combination of power and efficiency [55]. But it can still seem counterintuitive, that the most efficient wat to reach operation points at high speeds involve exciting a strong field with the rotor current, and then countering it with a negative stator x-current. To provide more insight in the field weakening method, different torques at 10 000 rpm is studied and presented in the right column of figure 5.28. Currents resulting in lower than 425 V are reachable with the available voltage supply (which goes down to 600 V for low battery state of charge for the original IPMSM). As the rotor current increases, the iso-voltage line for 425 V is pushed left, requiring more and more negative stator x current. But the iso-torque lines are also pushed down and left. For $I_\mathrm{r} = 500$ A, 40 Nm is reachable, but the iso-torque lines for 70 and 100 Nm are in unavailable voltage levels. So for low torque (40 Nm), low rotor current (below 500 A) are suitable, generating low losses. But to enable higher torques, more rotor current is needed. This is clear in figure 5.28, as more and more iso-torque lines are inside of 425 V as the rotor current in increased in the right column. Every operation point with different torques for a high speed uses the least necessary rotor current to push the torque line within reachable voltage, which requires more and more negative stator x current to weaken the field. This results in the EMSM being more efficient for low powers at high speeds, which is evident when comparing the efficiency maps of the IPMSM and the EMSM, in figure 5.26.

A short analysis of the losses is presented in figure 5.29. The stator winding losses show an almost non-existent speed dependence, partly because ANSYS models stranded wires as free from space harmonic losses and time harmonics (such as current ripple from the converter) are not modeled by the author in the simulations. On the contrary, the core losses are almost only speed dependent. The rotor windings increase their losses slightly with speed, as the AC losses rise. The pump power is more independent on speed, which is a sign that the air model overestimates the DC-losses calculated from the rotor current - If the DC losses calculated from the rotor current are larger than the input total rotor winding losses, the rotor winding losses that needs cooling are be assumed to be equal to the estimated DC losses, leaving no excess AC losses to cool beyond them, which is why the lines in the pump power plot are as straight as the rotor current lines in figure 5.27.

Appendix B presents loss and flux density plots of the machine, without further
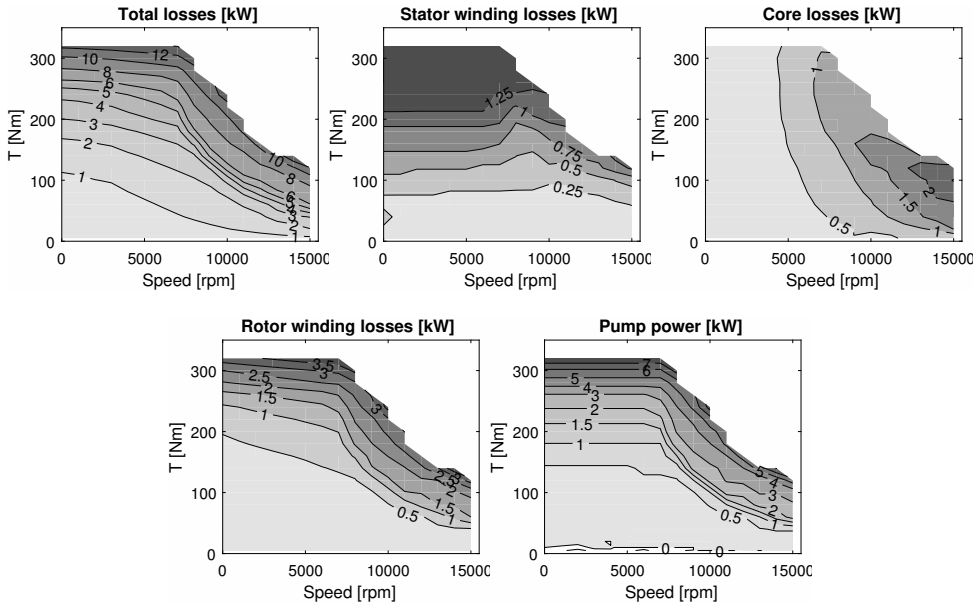
Figure 5.29: The losses of the EMSM in the peak power case.

comments or analysis.

5.5.2   Delimitations for performance comparison

When it comes to losses, the rotor iron and PM losses are not modeled in the IPMSM. The end windings are not modeled neither, for either machine. That reduces the copper and iron losses compared to a real application, but to a similar amount for both machines, making the results comparable for its purpose. Same goes with converter losses. The stator winding resistance voltage is neglected in the voltage limitation due to induced voltage.

For the EMSM, more simplifying assumptions are made. The rotor current supply is outside the area studied in this thesis, meaning the converter as well as the supply in form of slip rings or rotating transformer, are neglected. The design of the cooling system is also left out, where the efficiency of the pump or fan is expected to increase the losses further, and the temperature rise due to the increased pressure is expected to narrow down the temperature difference between the inlet air temperature and the maximum copper temperature.

Chapter 6

Conclusions

6.1 Conclusions

The main objective of the work of this thesis has been to investigate whether direct cooling can be used to improve the performance of an electrical machine and if, in that case, direct cooling can be used to make a PM-less machine that matches or even outperforms a PMSM. The work of this thesis constitutes an analytical study and concludes that the goal might very well be within reach. The designed EMSM outperforms the reference IPMSM in torque, power and speed capability. The efficiency of the EMSM is lower, but just slightly and operations points exist where the efficiency of the EMSM is higher than that of the IPMSM.

The air cooling model is developed to estimate the pump power needed to generate the necessary heat transfer. It is built to handle several types of direct cooled windings with circular or elliptic coolant channels, in order to find which dimensions are more suitable, in general or for a specific application. The possibilities to verify the model with experiments and computational fluid dynamics (CFD) simulations have been limited in the work of this thesis. However the little amount of testing that has been performed, shows comforting results, indicating that the model is at least not completely off in its estimation.

The model is used to determine winding dimensions for the rotor design with a combination of effective cooling, enabling at least 16 A/mm^2 slot fill factor for pure DC currents, and efficient cooling over a wide operation area. The model also provides a look-up table for the rotor design post-processing, which is used to merge the necessary pump power into the losses of the machine to

include them in the efficiency estimations for the rotor design and performance comparison.

A study is performed of how space harmonics affect the rotor winding losses and how the conductor size and air channel size affect the losses. It is concluded that the space harmonics induce a large amount of AC losses, but also that the rotor design has a big effect on their extent. The insights from this study are not only important for the work of this thesis, but also for the work ahead, for future research and applications of the direct cooling concept in what parameters have different grades of importance for the rotor winding losses.

The rotor design integrates the air cooling model through the lookup table and provides a perspicuous view over which rotor geometries and designs that are more suitable. A surprising deduction of this is that the rotor geometry that seemed worst in the rotor winding loss study performs better overall, in both torque and speed capacity. This indicates that the rotor design could be improved with even more work with the parameters identified in the loss study.

Through iterations of simulations, an optimal rotor design is narrowed down, with respect to the design parameters included in this work. The performance of the chosen design was compared to that of the reference PMSM, and proved to be able to beat it as well as meet the specification requirements. This is done with a maximum continuous rotor slot current density of 14 A/mm^2 (including area for insulation and padding) . Before a full comparison like that is interesting to make however, a thermal analysis of the whole EMSM should be done, as well as widening the delimitations such as including end winding effects, fan efficiency, and so on.

All in all, the work carries good signs for future work, as the direct cooling concept seems to surpass several of the other concepts in literature in current density, and also to be able to outperform an IPMSM with only slightly lower losses, fulfilling the objectives set for the work.

6.2   Reflections

Heat transfer and fluid dynamics are difficult fields with great uncertainties which require practical experiments in a wide range to be able to verify the models and to extend the model into higher inlet air speeds and pump powers than what is verified in the work of this thesis.

A few mysteries remain unsolved, meaning that some work is left to do after the

completion of this thesis. An example is why Geometry 1 has higher losses for higher rotor currents, as opposed to the other geometries. Somewhat surprising, Geometry 1 proved to be the best geometry overall, even though it had the most amount of AC losses in the rotor windings. There was no room in this thesis, time wise, to analyze the reasons why it still came out on top in the overall performance. A guess from the author is that it has to do with the use of space in the rotor, as both geometry 2 and 3 has some amount of space wasted in the angle between the rectangular winding areas.

This work finishes a first important step when it comes to studying the real potential in the proposed direct cooling concepts. When it comes to determining which of the concepts, indented or hollow rectangular windings, is best, manufacturability as well as cooling performance in experiments has to be weighed in.

For the full system design, a lot of more aspects have to be studied. The placement of the fan matters, as a pumping fan will increase the air temperature before the air even enters the cooling channels. A sucking channel will on the other hand decrease the air density, worsening the cooling properties of the air. The air can be circulated in a closed loop, and be cooled by cooling fins or a heat exchanger somewhere in the loop. Or it could be taken from the surrounding, which requires filters and gives the placement of the system a huge impact, as it requires cool and clean air from the surrounding to be available close to the machine. And then, of course, other coolants should be considered.

The AC losses are assumed to be evenly spread out over the whole rotor slot in the rotor design work, even though simulations show that they are induced on the fringe of a few windings close to the air gap. Another assumption would require more thermal analysis about whether the heat from those exposed windings spread to the surrounding windings or if the pump power needs to be increased further, to keep the hotspot cool enough.

Writing a licentiate thesis is difficult and takes a lot of work and one could argue that time would be more valuable spent on working on the doctoral thesis. But I am not that one. I am glad I took the time to write this licentiate thesis, since I have learnt a lot that will help the planning and writing of my next thesis. I consider this experience invaluable with that goal ahead of me.

6.3   Future work

The following needs further attention as the work proceeds.

- 3D CFD simulations can potentially supplement where experiments and numerical models can not go, and at least that possibility should be explored as the work progresses.

- As mentioned, more experiments are needed, both for individual pipes to verify the fluid dynamics approximated by the model, for pipes of more different dimensions, and for both concepts proposed in this thesis.

- The effect the rotating rotor has on the air flow needs to be investigated, whether by simulations, analytically or experiments.

- The effect of different design parameters (such as wedge angle and slot depth) should be further investigated and then applied, if an actual rotor or whole machine is to be designed and built for prototype.

- The options for supplying the rotor windings with current should be considered, comparing advantages and disadvantages with slip-rings and rotating transformers, as well as converter properties.

Appendix A

Rotating x/y-frame of reference

In a synchronous machine, the magnetizing field of a magnetized rotor have a fixed physical angle on the rotor. When the rotor rotates, the field will follow. This physical direction defines the direct axis, d. An angle 90 electrical degrees away from the d-axis in turn defines the quadrature axis, q.

The stator current, typically three phase, then has to vary with the same frequency as the rotation of the d/q-frame. The alternating current in the stator windings results in a rotating magnetizing field. In the α/β-frame, which is fixed on the stator, the stator magnetizing field looks like a rotating vector.

The stator current is defined as components of α and β in the same direction as the field. This vectors angle is then compared to the angle of the d/q-frame in every instance. A corresponding frame for the stator, mimicking the rotor's d/q-frame, is defined as the x/y frame. The value of the stator current's α/β-vector is transferred to the x/y-frame, with an angle always corresponding the α/β-current's angle in the d/q-frame.

The result of this is a vector in the x/y-frame showing where the stator's magnetizing field is compared to the rotor's. A stator current aligned with the x-axis means the rotor and stator fields are aligned as the rotor rotates. To generate torque, an angle different from 0 degrees from the x-axis is needed. An illustration of the vectors is shown in figure A.1

The scaling of the α/β- or x/y-current vector can be done in different ways. Since the stator current is actually three different currents in one phase each,
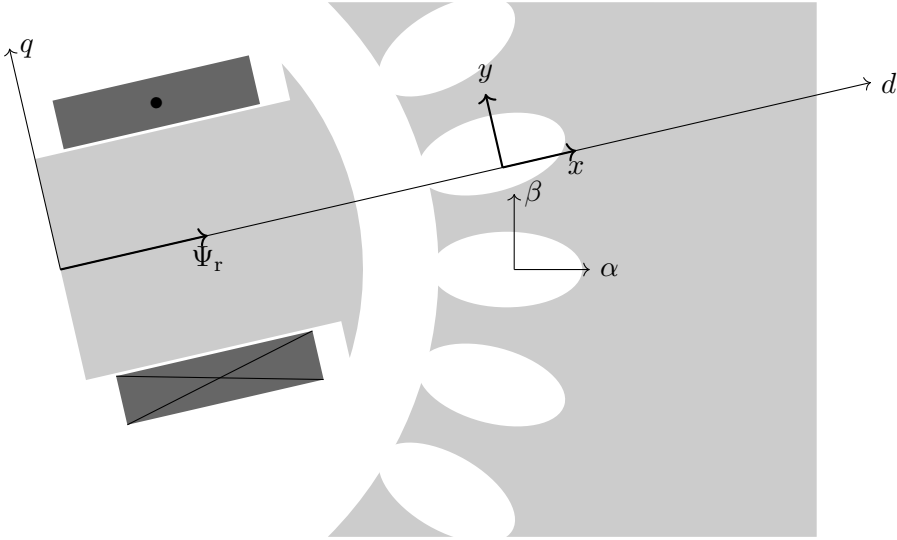
Figure A.1: Illustration of the defined vectors in a 2-pole synchronous machine. All frames have the origin in the center of the machine. The position of the frames in the illustration is supposed to clearify which frames are used for the stator and rotor respectively.

and the α/β-representation is only one vector, this scaling method is not trivial.

Preferably this scaling is done through a power invariant transformation. This means any currents of voltages in the d/q-frame can be treated as DC-equivalents, and any power-calculation in the d/q-frame will result in the same power as the total power of all three phases. Power invariant x and y currents are represented with lower case i.

However, the ANSYS-simulations on electrical machines in this thesis, does not use power invariant transformation, but merely let the value of the x/y-vector represent the rms-value of a single phase current. This transformation is represented with upper case I in this thesis, and the scale compared to power invariant transformed currents corresponds to $i = \sqrt{3}I$.

Currents in the x/y-frame are divided into four quadrants. The first two quadrants correspond to positive y-values and generally represent operation points where the machine is running as a motor. Thus, the third and fourth quadrant is unexplored in the work of this thesis, even though generator operation is also interesting for traction machines for future studies. The first quadrant correspond to positive x and y values, while the second quadrant corresponds to negative x-currents. Because of the opposite saliencies of the EMSM and IPMSM, the main operation is situated in different quadrants. The most simulated current
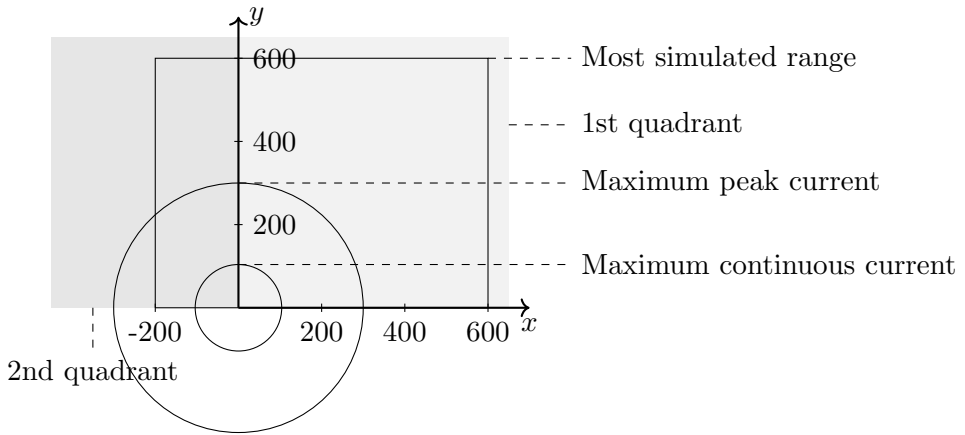
Figure A.2

range for the EMSM is shown in figure A.2.

Appendix B

Loss and flux density

Field plots retrieved from ANSYS at I_x = -70 A, I_y = 290 A, I_r = 3110 A, at 6000 rpm, as the maximum power operation point at nominal speed.
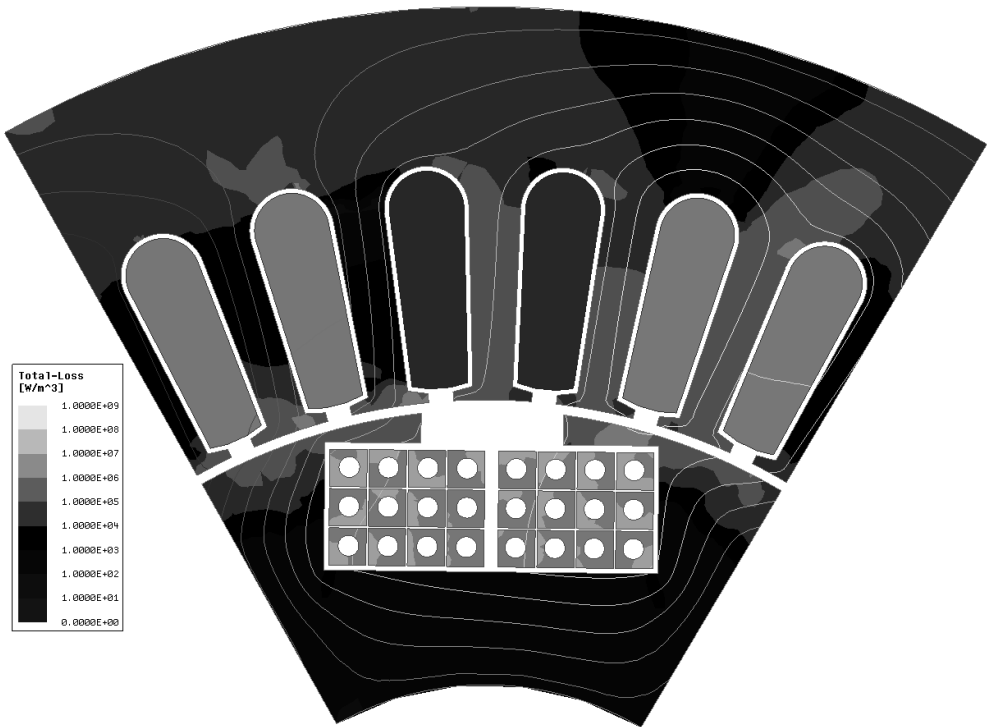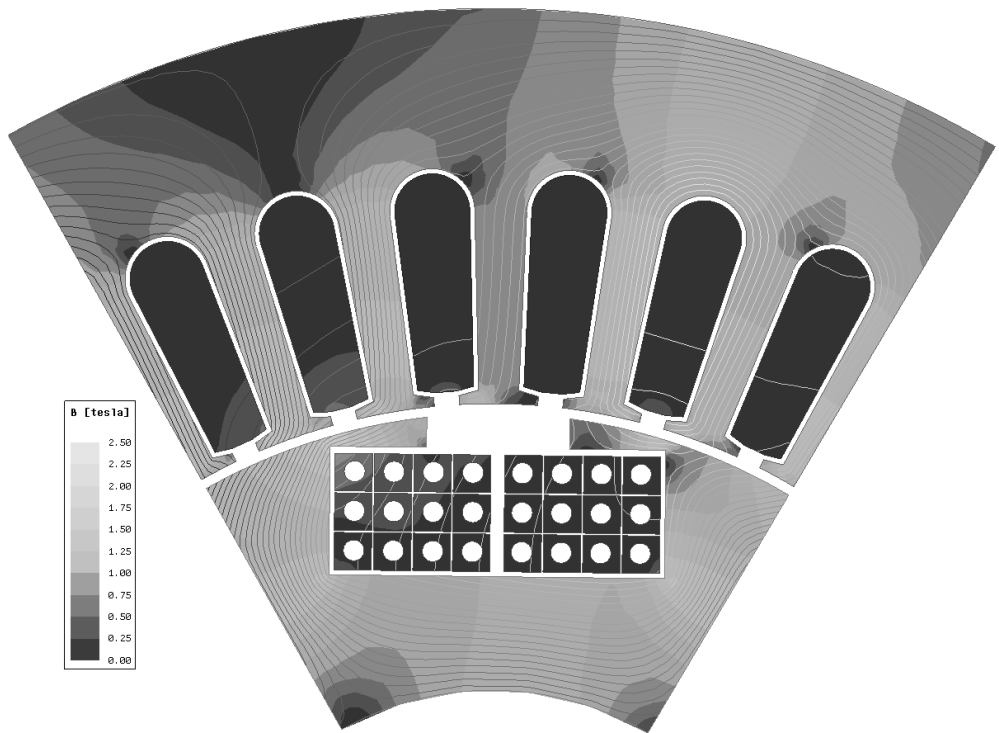
Figure B.1: Loss density.

Figure B.2: Flux density.

References

[1] J. Pontes. EV Sales - World Top 20 December 2017, 2018 (accessed on 2018-06-14). http://ev-sales.blogspot.com/2018/01/world-top-20-december-2017.html.

[2] China Auto Web. BAIC ES 210 (Senova EV), December 2014 (accessed on 2018-06-15). http://chinaautoweb.com/car-models/baic-senova-ev/.

[3] E. A. Grunditz and T. Thiringer. Performance analysis of current bevs based on a comprehensive review of specifications. *IEEE Transactions on Transportation Electrification*, 2(3):270–289, Sept 2016.

[4] James D. Widmer, Richard Martin, and Mohammed Kimiabeigi. Electric vehicle traction motors without rare earth magnets. *Sustainable Materials and Technologies*, 3:7 – 13, 2015 (accessed on 2018-06-15). http://www.sciencedirect.com/science/article/pii/S2214993715000032.

[5] Zhidou Košice. Elektromobil ZhiDou D2, (accessed on 2018-06-15. http://zhidou-kosice.sk/zd-d2.

[6] Renault. Zoe Brochure, October 2017 (accessed on 2018-06-15). https://www.brayleys.co.uk/pdf/renault-zoe-brochure.pdf.

[7] wattEV2Buy. Comparing China's popular pure electric SUVs – BYD Song vs Roewe eRX5, September 2017 (accessed on 2018-06-15). https://wattev2buy.com/comparing-chinas-popular-pure-electric-suvs-byd-song-vs-roewe-erx5/.

[8] CNET. Deep dive: The 2017 Chevrolet Bolt's electric powertrain, April 2016 (accessed on 2018-06-15). https://www.cnet.com/roadshow/news/deep-dive-2017-chevrolet-bolt-electric-powertrain/.

[9] Chery International. New-Energy eq, (accessed on 2018-06-15). http://www.cheryinternational.com/new-energy-eq.html.

[10] Wikipedia. Chevrolet Volt, (accessed on 2018-06-15). https://en.wikipedia. org/wiki/Chevrolet_Volt.

[11] JAC. CCPC , JAC IEV7S won the champion of Pure-electric SUV group in Karamay, August 2017 (accessed on 2018-06-15). http://jacen.jac.com. cn/article/20170802/75091914.html.

[12] My Outlander PHEV. Mitsubishi Outlander PHEV Specs, March 2013 (accessed on 2018-06-15). http://www.myoutlanderphev.com/ mitsubishi-outlander-phev-specs.

[13] Auto Industriya. BYD reveals Qin EV300, e5 with 300km range, April 2016 (accessed on 2018-06-15). https://www.autoindustriya.com/ auto-industry-news/byd-reveals-qin-ev300-e5-with-300km-range.html.

[14] China Auto Web. Geely Emgrand EV, November 2015 (accessed on 2018- 06-15). http://chinaautoweb.com/car-models/geely-emgrand-ev/.

[15] BYD Philippines. BYD Qin sedan HV, (accessed on 2018-06-15). http: //byd.com.ph/showroom/sedan/qin.

[16] Car and Driver. 2016 BMW 330e, July 2016. https://www.caranddriver. com/reviews/2016-bmw-330e-iperformance-tested-review.

[17] Teknikens värld. Provkörning av Hyundai Ioniq Electric, Janu- ary 2017 (accessed on 2018-06-15). http://teknikensvarld.se/ provkorning-av-hyundai-ioniq-electric-390450/.

[18] J. de Santiago, H. Bernhoff, B. Ekergard, S. Eriksson, S. Ferhatovic, R. Waters, and M. Leijon. Electrical motor drivelines in commercial all- electric vehicles: A review. *Vehicular Technology, IEEE Transactions on*, 61(2):475–484, Feb 2012.

[19] T Maughan. The worst place on earth, 2015 (accessed on 2018-04-13). http://www.bbc.com/future/story/20150402-the-worst-place-on-earth.

[20] C. Milmo. Concern as China clamps down on rare earth exports, 2010 (ac- cessed on 2018-04-13). https://www.independent.co.uk/news/world/asia/ concern-as-china-clamps-down-on-rare-earth-exports-1855387.html.

[21] Roskill. Rare Earths, Global Industry, Markets & Outlook 2017. Tech- nical Report 17, Roskill, November 2017 (accessed on 2018-04-13). https: //roskill.com/market-report/rare-earths/.

[22] K. Kaiman. The Rare-Earth Crisis, 2011 (accessed on 2018-04-13). https: //www.technologyreview.com/s/423730/the-rare-earth-crisis/.

[23] C. Bontron. Rare-earth mining in China comes at a heavy cost for local villages, 2012 (accessed on 2018-04-13). https://www.theguardian.com/environment/2012/aug/07/china-rare-earth-village-pollution.

[24] J. Kaiman. Rare earth mining in China: the bleak social and environmental costs, 2014 (accessed on 2018-04-13). https://www.theguardian.com/sustainable-business/rare-earth-mining-china-social-environmental-costs.

[25] K. Bradsher. Prices of Rare Earth Metals Declining Sharply, 2011 (accessed on 2018-04-13). https://www.nytimes.com/2011/11/17/business/global/prices-of-rare-earth-metals-declining-sharply.html.

[26] F. Els. China to become net importer of some rare earths, 2017 (accessed on 2018-04-13). https://www.theguardian.com/environment/2012/aug/07/china-rare-earth-village-pollution.

[27] M. Ritchie. Rare Earth Metals Electrified by China's Illegal Mining Clean-Up, 2017 (accessed on 2018-04-13). https://www.bloomberg.com/news/articles/2017-09-07/rare-earth-metals-electrified-by-china-s-illegal-mining-clean-up.

[28] R. Cho. Rare Earth Metals: Will We Have Enough?, 2012 (accessed on 2018-04-13). http://blogs.ei.columbia.edu/2012/09/19/rare-earth-metals-will-we-have-enough/.

[29] P. Fyhr, J. E. Ståhl, and M. Andersson. The scale of permanent magnet materials for automotive traction motors. In *2012 2nd International Electric Drives Production Conference (EDPC)*, pages 1–7, Oct 2012.

[30] S. Estenlund, M. Alaküla, and A. Reinap. Pm-less machine topologies for ev traction: A literature review. In *2016 International Conference on Electrical Systems for Aircraft, Railway, Ship Propulsion and Road Vehicles International Transportation Electrification Conference (ESARS-ITEC)*, pages 1–6, Nov 2016.

[31] C. Oprea, A. Dziechciarz, and C. Martis. Comparative analysis of different synchronous reluctance motor topologies. In *Environment and Electrical Engineering (EEEIC), 2015 IEEE 15th International Conference on*, pages 1904–1909, June 2015.

[32] J. Malan, M.J. Kamper, and P.N.T. Williams. Reluctance synchronous machine drive for hybrid electric vehicle. In *Industrial Electronics, 1998. Proceedings. ISIE '98. IEEE International Symposium on*, volume 2, pages 367–372 vol.2, Jul 1998.

[33] A. Walker, M. Galea, C. Gerada, A. Mebarki, and D. Gerada. A topology selection consideration of electrical machines for traction applications: towards the freedomcar 2020 targets. In *Ecological Vehicles and Renewable Energies (EVER), 2015 Tenth International Conference on*, pages 1–10, March 2015.

[34] I. Boldea, L.N. Tutelea, L. Parsa, and D. Dorrell. Automotive electric propulsion systems with reduced or no permanent magnets: An overview. *Industrial Electronics, IEEE Transactions on*, 61(10):5696–5711, Oct 2014.

[35] E. Cosoroaba, W. Wang, and B. Fahimi. Comparative study of two winding configurations for a double stator switched reluctance machine. In *Electrical Machines (ICEM), 2014 International Conference on*, pages 1013–1017, Sept 2014.

[36] Z.Q. Zhu and D. Howe. Electrical machines and drives for electric, hybrid, and fuel cell vehicles. *Proceedings of the IEEE*, 95(4):746–765, April 2007.

[37] M.A. Tavakkoli and M. Moallem. Torque ripple mitigation of double stator switched reluctance motor (dssrm) using a novel rotor shape optimization. In *Energy Conversion Congress and Exposition (ECCE), 2012 IEEE*, pages 848–852, Sept 2012.

[38] A. Chiba, Y. Takano, M. Takeno, T. Imakawa, N. Hoshi, M. Takemoto, and S. Ogasawara. Torque density and efficiency improvements of a switched reluctance motor without rare-earth material for hybrid vehicles. *Industry Applications, IEEE Transactions on*, 47(3):1240–1246, May 2011.

[39] W. Wang and B. Fahimi. Comparative study of electric drives for ev/hev propulsion system. In *Electrical Systems for Aircraft, Railway and Ship Propulsion (ESARS), 2012*, pages 1–6, Oct 2012.

[40] K.M. Rahman, B. Fahimi, G. Suresh, A.V. Rajarathnam, and M. Ehsani. Advantages of switched reluctance motor applications to ev and hev: design and control issues. *Industry Applications, IEEE Transactions on*, 36(1):111–121, Jan 2000.

[41] A. Chiba, K. Kiyota, N. Hoshi, M. Takemoto, and S. Ogasawara. Development of a rare-earth-free sr motor with high torque density for hybrid vehicles. *Energy Conversion, IEEE Transactions on*, 30(1):175–182, March 2015.

[42] K. Kiyota and A. Chiba. Design of switched reluctance motor competitive to 60-kw ipmsm in third-generation hybrid electric vehicle. *Industry Applications, IEEE Transactions on*, 48(6):2303–2309, Nov 2012.

[43] M. Abbasian, M. Moallem, and B. Fahimi. Double-stator switched reluctance machines (dssrm): Fundamentals and magnetic force analysis. *Energy Conversion, IEEE Transactions on*, 25(3):589–597, Sept 2010.

[44] W. Wang, C. Lin, and B. Fahimi. Comparative analysis of double stator switched reluctance machine and permanent magnet synchronous machine. In *Industrial Electronics (ISIE), 2012 IEEE International Symposium on*, pages 617–622, May 2012.

[45] M. Asgar and E. Afjei. Radial force reduction in a new flat-type double-stator switched reluctance motor. *Energy Conversion, IEEE Transactions on*, PP(99):1–9, 2015.

[46] A.H. Isfahani and B. Fahimi. Comparison of mechanical vibration between a double-stator switched reluctance machine and a conventional switched reluctance machine. *Magnetics, IEEE Transactions on*, 50(2):293–296, Feb 2014.

[47] A.H. Isfahani and B. Fahimi. Multi-physics analysis of double stator switched reluctance machines. In *Energy Conversion Congress and Exposition (ECCE), 2013 IEEE*, pages 2827–2833, Sept 2013.

[48] C. Rossi, D. Casadei, A. Pilati, and M. Marano. Wound rotor salient pole synchronous machine drive for electric traction. In *Industry Applications Conference, 2006. 41st IAS Annual Meeting. Conference Record of the 2006 IEEE*, volume 3, pages 1235–1241, Oct 2006.

[49] Y. Amara, L. Vido, M. Gabsi, E. Hoang, M. Lecrivain, and F. Chabot. Hybrid excitation synchronous machines: Energy efficient solution for vehicle propulsion. In *Vehicle Power and Propulsion Conference, 2006. VPPC '06. IEEE*, pages 1–6, Sept 2006.

[50] W.Q. Chu, Z.Q. Zhu, J. Zhang, X. Ge, X. Liu, D. Stone, and M. Foster. Comparison of electrically excited and interior permanent magnet machines for hybrid electric vehicle application. In *Electrical Machines and Systems (ICEMS), 2014 17th International Conference on*, pages 401–407, Oct 2014.

[51] D.G. Dorrell. Are wound-rotor synchronous motors suitable for use in high efficiency torque-dense automotive drives? In *IECON 2012 - 38th Annual Conference on IEEE Industrial Electronics Society*, pages 4880–4885, Oct 2012.

[52] W.Q. Chu, Z.Q. Zhu, and J.T. Chen. Analytical optimization and comparison of torque densities between permanent magnet and electrically excited

machines. In *Electrical Machines (ICEM), 2012 XXth International Conference on*, pages 1192–1198, Sept 2012.

[53] W.Q. Chu, Z.Q. Zhu, and J.T. Chen. Simplified analytical optimization and comparison of torque densities between electrically excited and permanent-magnet machines. *Industrial Electronics, IEEE Transactions on*, 61(9):5000–5011, Sept 2014.

[54] Thomas Bergh. *Belt driven Alternator and Starter with a Series Magnetized Synchronous Machine drive.* PhD thesis, Lund University, 2006 (accessed on 2018-06-15). http://www.iea.lth.se/publications/Theses/LTH-IEA-1052.pdf.

[55] W.Q. Chu, Z.Q. Zhu, Jian Zhang, Xu Liu, D.A. Stone, and M.P. Foster. Investigation on operational envelops and efficiency maps of electrically excited machines for electrical vehicle applications. *Magnetics, IEEE Transactions on*, 51(4):1–10, April 2015.

[56] Y. Liu, J. Zhao, R. Wang, and C. Huang. Performance improvement of induction motor current controllers in field-weakening region for electric vehicles. *Power Electronics, IEEE Transactions on*, 28(5):2468–2482, May 2013.

[57] W. Xu, J. Zhu, Y. Guo, S. Wang, Y. Wang, and Z. Shi. Survey on electrical machines in electrical vehicles. In *Applied Superconductivity and Electromagnetic Devices, 2009. ASEMD 2009. International Conference on*, pages 167–170, Sept 2009.

[58] M. Zeraoulia, M.E.H. Benbouzid, and D. Diallo. Electric motor drive selection issues for hev propulsion systems: A comparative study. *Vehicular Technology, IEEE Transactions on*, 55(6):1756–1764, Nov 2006.

[59] E-Magnets UK. Grades of Neodymium, (accessed on 2018-06-15) note =.

[60] Vacuumschmelze. RARE EARTH PERMANENT MAGNETS VACOdym • VACOmax, 2014 (accessed on 2018-06-15). http://www.vacuumschmelze.com/fileadmin/Medienbiliothek_2010/Downloads/DM/VACODYM-VACOMAX-PD002_2015_en.pdf.

[61] LWW Group. Product brochures, 2017 (accessed on 2018-06-15). http://www.lww.se/wp-content/uploads/2017/06/DAMIDBOND-200-bondable-1.pdf.

[62] E. L. Brancato. Estimation of lifetime expectancies of motors. *IEEE Electrical Insulation Magazine*, 8(3):5–13, May 1992.

[63] K. M. Rahman and S. E. Schulz. Design of high efficiency and high density switched reluctance motor for vehicle propulsion. In *Conference Record of the 2001 IEEE Industry Applications Conference. 36th IAS Annual Meeting (Cat. No.01CH37248)*, volume 3, pages 2104–2110 vol.3, Sept 2001.

[64] P. M. Lindh, I. Petrov, R. S. Semken, M. Niemelä, J. J. Pyrhönen, L. Aarniovuori, T. Vaimann, and A. Kallaste. Direct liquid cooling in low-power electrical machines: Proof-of-concept. *IEEE Transactions on Energy Conversion*, 31(4):1257–1266, Dec 2016.

[65] P. Lindh, I. Petrov, A. Jaatinen-Värri, A. Grönman, M. Martinez-Iturralde, M. Satrústegui, and J. Pyrhönen. Direct liquid cooling method verified with an axial-flux permanent-magnet traction machine prototype. *IEEE Transactions on Industrial Electronics*, 64(8):6086–6095, Aug 2017.

[66] V. Ruuskanen, J. Nerg, M. Niemelä, J. Pyrhönen, and H. Polinder. Effect of radial cooling ducts on the electromagnetic performance of the permanent magnet synchronous generators with double radial forced air cooling for direct-driven wind turbines. *IEEE Transactions on Magnetics*, 49(6):2974–2981, June 2013.

[67] M. Polikarpova, P. Röyttä, J. Alexandrova, S. Semken, J. Nerg, and J. Pyrhönen. Thermal design and analysis of a direct-water cooled direct drive permanent magnet synchronous generator for high-power wind turbine application. In *2012 XXth International Conference on Electrical Machines*, pages 1488–1495, Sept 2012.

[68] N. A. Rahman, E. Bostanci, and B. Fahimi. Thermal analysis of switched reluctance motor with direct in-winding cooling system. In *2016 IEEE Conference on Electromagnetic Field Computation (CEFC)*, pages 1–1, Nov 2016.

[69] C. Högmark, R. Andersson, A. Reinap, and M. Alaküla. Electrical machines with laminated winding for hybrid vehicle applications. In *2012 2nd International Electric Drives Production Conference (EDPC)*, pages 1–6, Oct 2012.

[70] R. Andersson, C. Högmark, A. Reinap, and M. Alaküla. Modular three-phase machines with laminated winding for hybrid vehicle applications. In *2012 2nd International Electric Drives Production Conference (EDPC)*, pages 1–7, Oct 2012.

[71] A. Reinap, F. J. Márquez-Fernández, R. Andersson, C. Högmark, M. Alaküla, and A. Göransson. Heat transfer analysis of a traction machine

with directly cooled laminated windings. In *2014 4th International Electric Drives Production Conference (EDPC)*, pages 1–7, Sept 2014.

[72] S. Estenlund. Model of air cooled windings for traction machine. In *2XXIIIrd International Conference on Electrical Machines (ICEM)*, pages 1–6, Sep 2018.

[73] F. M. White. *Fluid mechanics*. McGraw-Hill, New York, 7 edition, 2011.

[74] B. Sunden. *Introduction to Heat Transfer*. WIT Press, Southampton, UK, 2012.

[75] B. R. Munson, D. F. Young, T. H. Okiishi, and W. W. Huebsch. *Fundamentals of Fluid mechanics*. J Wiley, New York, 6 edition, 2009.

[76] F. P. Incropera, D. P. Dewitt, T. L. Bergman, and A. S. Lavine. *Fundamentals of Heat and Mass transfer*. J Wiley, New York, 6 edition, 2007.

[77] H. Schlichting. *Boundary layer theory*. McGraw-Hill, New York, 7 edition, 1979.

[78] SF Pressure Drop Online-Calculator: Roughness of pipes, (accessed on 2018-06-15). http://www.pressure-drop.com/Online-Calculator/rauh.html.

[79] L. F. Moody. Friction Factors for Pipe Flow. *Transactions of the ASME*, 66:671, 1944.

[80] M. Gabassi. Directly cooled windings - Conjugate heat transfer assessment of air-cooled hollow conductor. MSc thesis, Lund University, 2018.

[81] S. Jayanti. Bends, Flow and Pressure Drop in. http://www.thermopedia.com/content/577/.

[82] R. Andersson, A. Reinap, and M. Alaküla. Design and evaluation of electrical machine for parallel hybrid drive for heavy vehicles. In *2012 XXth International Conference on Electrical Machines*, pages 2622–2628, Sept 2012.

[83] R. Andersson and A. Reinap. Loss mapping of an insert permanent magnets synchronous machine for parallel hybrid electric heavy vehicles. In *2016 XXII International Conference on Electrical Machines (ICEM)*, pages 1847–1853, Sept 2016.

[84] ANSYS. Electromagnetic Simulation Products, 2017 (accessed on 2018-06-15). https://www.ansys.com/products/electronics.

LUND
UNIVERSITY